EXCITED-STATE DYNAMICS OF IRON(II)-BASED CHARGE-TRANSFER CHROMOPHORES

By

Allison Michelle Brown

A DISSERTATION

Submitted to
Michigan State University
in partial fulfillment of the requirements
for the degree of

DOCTOR OF PHILOSOPHY

Chemistry

2011

ABSTRACT

EXCITED-STATE DYNAMICS OF IRON(II)-BASED CHARGE-TRANSFER CHROMOPHORES

By

Allison Michelle Brown

Iron(II) photophysics is a field of research that has been, and continues to be, extensively studied by both calculation and experiment. The reactivity and photophysical properties of these complexes are very well understood, providing both a fundamental understanding of the science as well as a foundation for applying that understanding. This dissertation discusses the viability iron(II)-based complexes may have in one particular application: dye-sensitized solar cells. The recent and explosive interest in ruthenium(II) complexes for the application in solar cells begs the question of whether the isoelectronic and 100-fold more abundant substitution can be made. A concurrent decrease in price and increase in scalability would result from the successful replacement of ruthenium with iron. However, intrinsic differences in ligand field splitting between first and second row transition metals produce low-lying electronic states that short circuit the iron-based cells. Overcoming these deactivation pathways is the purpose of this research and will be the focus and end goal for the discussions herein.

In honor of:
Selmer, Gurina, Ashley
Dedicated to:
Odin, Eleanor, Adelheyd, Madeline

AKNOWLEDGEMENTS

Many people have played important roles in my graduate career. Jim, you have been an amazing mentor, advisor, and advocate. Your confidence has afforded me opportunities to expand my skill set and knowledge base as well make connections and find a career path. The guidance you provide our group is based on teaching us how to be scientists, an aspiration too few advisors possess, for it is a gift that will benefit each of us on any and every path we take. The McCusker group, past and present, has challenged and supported me through the good and bad times. Amanda and Eric, you both have become good friends and invaluable resources without whom my abilities in ultrafast spectroscopy would be nil. Dong, Rick, Kate, Shenshen, Troy, Andrew, and Larry, you have been superb colleagues—giving of time, critiques, and advice throughout my time in Michigan. Joel, I'm so pleased to have started together. You helped me through both transition periods of the laser lab mentally and physically and became my favorite travel partner—I feel as though I have a true colleague and friend. Lindsey, there are not enough words to describe the respect and gratitude I have for you, without whom my graduate career and subsequent opportunities would have been very different. Your ability to see our common goals through a different perspective coupled with your skills to synthesize the desired compounds has provided me successful research projects. I will forever be grateful that you joined our group, being both a friend and talented scientist. Lisa, we have been both advocates and adversaries… in the end, I can't imagine my time in Michigan without you. Eileen and Jennie, you will make a powerful team for the ultrafast systems. You are both intelligent and talented women with the abilities and understanding to dominate the technology and the science. Believe in

yourselves and never be too focused to stop and skip the Pandora song that is throwing you into a funk. Dani—I don't need you, but I like you. You should be proud of and confident in yourself and your ability to accomplish anything you set your mind to. Keep me in the back of your mind and I'll keep yours in mine. I'm so proud you will be my research sister for life.

I have been fortunate to make many lifelong friendships during my time in Michigan. Aman, my first and closest—I'm so glad they let you in. Monica, Lucho, Juan-David, Borzoo, Maryam, Amir, Dani, Hovig, Jay, Jill, Amber, Melissa, Pam, Felipe, Fede—you made Michigan a place worth living. Nick, you stole me from the grasps of depression and gave me happiness when I needed it most. I wouldn't have made it through the stress of the last months without you. I am so excited to start our next chapter together.

My family has been a phenomenal support—always patient, understanding, and encouraging. Odin, Eleanor, Adelheyd, and Madeline—one by one you have provided motivation to both be productive and take time off to visit you. Jeremy, Sarah, Joel, and Leah have been both amazing role models as well as effective tempters. You made coming home so wonderful and could make my day better in Michigan with a simple phone call. Quinn, you are always a positive and encouraging voice. Thank you for visiting me so often. Debbie, you have been a serendipitous addition to my life and I feel fortunate for the love and support you give. I'm also grateful for your family in Michigan: for the additional visits from you and Dad and the extra support from the family, even the offer to help "defend" my thesis, the good old-fashioned way. Craig, you are a rock and I am so lucky to have grown up with you. Thank you for all the opportunities you provided our family and the unconditional love you have so generously given.

Mom, I love you so much and can't imagine a better role model. You possess so many attributes I admire and I couldn't have picked a better woman to show me the strength, confidence, and sense of self this process required. Dad. Your constant support and realistic empathy through all of this has sustained me. Every nervous breakdown was met with comforting words and encouragement. You were essential to my success in this process. I am so thrilled to be your daughter and grateful for all of the effort you have put into us. Every time I think of all that you have accomplished, I am amazed.

Me Quiero!!!! I love you all!!!

TABLE OF CONTENTS

LIST OF TABLES

LIST OF FIGURES

Chapter 1: Introduction

Worldwide energy use can be modeled and predicted with three values: population, income per capita, and efficiency of energy usage.[1,2] With that in mind, the already staggering amount of energy consumed annually on a global level is predicted to double by 2050 and triple by 2100 due to an increase in population and the advancement of underdeveloped countries.[2] The $\sim 15 \times 10^{12}$ watts (15 TW) currently in use is primarily supplied by fossil fuels, with a small percentage coming from nuclear (9%) and renewable resources (8%).[3] The gap that exists between the amount of energy that is currently produced and the amount that will be required in the future will likely be filled with energy sources that are easy to obtain and transport to the places they will be used. Local resource abundance as well as cost and ease of use will factor into the types of energy sources utilized.

Historically, carbon-based sources of fuel (wood, coal, natural gas, oil) have been the easiest to obtain and convert to useful energy.[4] Although the efficiency with which they release useful energy leaves something to be desired, carbon-based sources have been abundant, reliable, and relatively easy to find and use. The non-renewable and finite abundances of oil and natural gas in particular, however, have made finding and securing these resources increasingly more difficult and expensive. Not only does the decreasing abundance affect the price, but the lack of equal distribution of these resources worldwide also leads to instability between countries that have and those that have not.

Issues surrounding the use of fossil fuels are not only political, geological, geographical, and economical, but there is also a large environmental impact to consider. Burning carbon-based materials results in the release of carbon dioxide (CO_2), among other products. A correlation between CO_2 levels and atmospheric temperatures has been identified and traced back at least 400,000 years and current CO_2 levels are higher than ever recorded on this time-scale.[5] Results of increasing them further are unknown: global temperature may be affected, but increased air pollution, ocean acidity, and coral reef bleaching have already been a direct result of the CO_2 concentration increase.[5] At this time, predictions can be made, but no one can know what effects will come from the continued release of CO_2 into the atmosphere.

In order to bridge the energy gap that faces the world in the next few decades with as little carbon-based sources as possible, alternative energy sources are currently the subject of vast and intense research. Sustainable and non-sustainable carbon-neutral/carbon-free sources are being researched and exploited to supply every additional TW with fossil fuel-free energy. Among the leaders are nuclear and renewable (solar, hydroelectric, wind, geothermal, biomass, etc.) sources. Following a supply and demand-type argument, solar is the only source that can provide the necessary energy (and more), as more than 120,000 TW hit the Earth's surface. This is 8000 times the current energy usage. It has been calculated that covering 0.16% of Earth's land area with 10% efficient solar cells would harvest 20 TW.[2] Not only is this more than enough for the world's energy needs, but technology is already in place to reach these efficiencies.

Silicon-based solar cells can perform in commercial modules with up to 20% efficiencies[6,7] and the industry has grown at a rate of 30% per year over the last decade.[8] However, the cost/efficiency ratio of these cells and modules are not economically competitive with fossil fuels. With the price of electricity from coal between 10 and 50 times less expensive than electricity from solar energy[9], the cost of switching energy sources is too high. Additional classes of solar cells such as thin film, organic, and sensitized solar cells have received funding and attention for various advantages (high efficiency, low cost, abundant materials, ease of processing), but suffer from the similar problem of low efficiency/cost ratios.[10] These ratios must increase significantly in order to make solar energy a viable competitor with fossil fuels sources for electricity. Scientific breakthroughs must accompany the engineering and manufacturing obstacles standing in the way of cheap and efficient solar energy.

Dye-sensitized solar cells (DSSCs) make up a unique class of solar cells that utilize a mechanism for electron movement that eases the restriction of sample purity that imposes high manufacturing costs on silicon-based solar cells and avoids the minority carrier diffusion plaguing organic solar cell efficiency. In brief, a light absorber is chemically attached to a nanostructured wide band gap semiconductor. The exited state of the light absorber - a transition metal-based dye molecule in the present case, but can also be a quantum dot, porphyrin system, or other light absorbing entity - is situated at a potential negative of the semiconductor band gap. Following light absorption, electrons from the excited state are injected into the conduction band, traverse to the back contact of the electrode, and are shuttled to the counter electrode, producing a current. From the counter

electrode, electrons reduce a redox mediator in an organic electrolyte and are further used to rereduce the now oxidized sensitizer, making the process regenerative. A scheme of the device is shown in Figure 1.

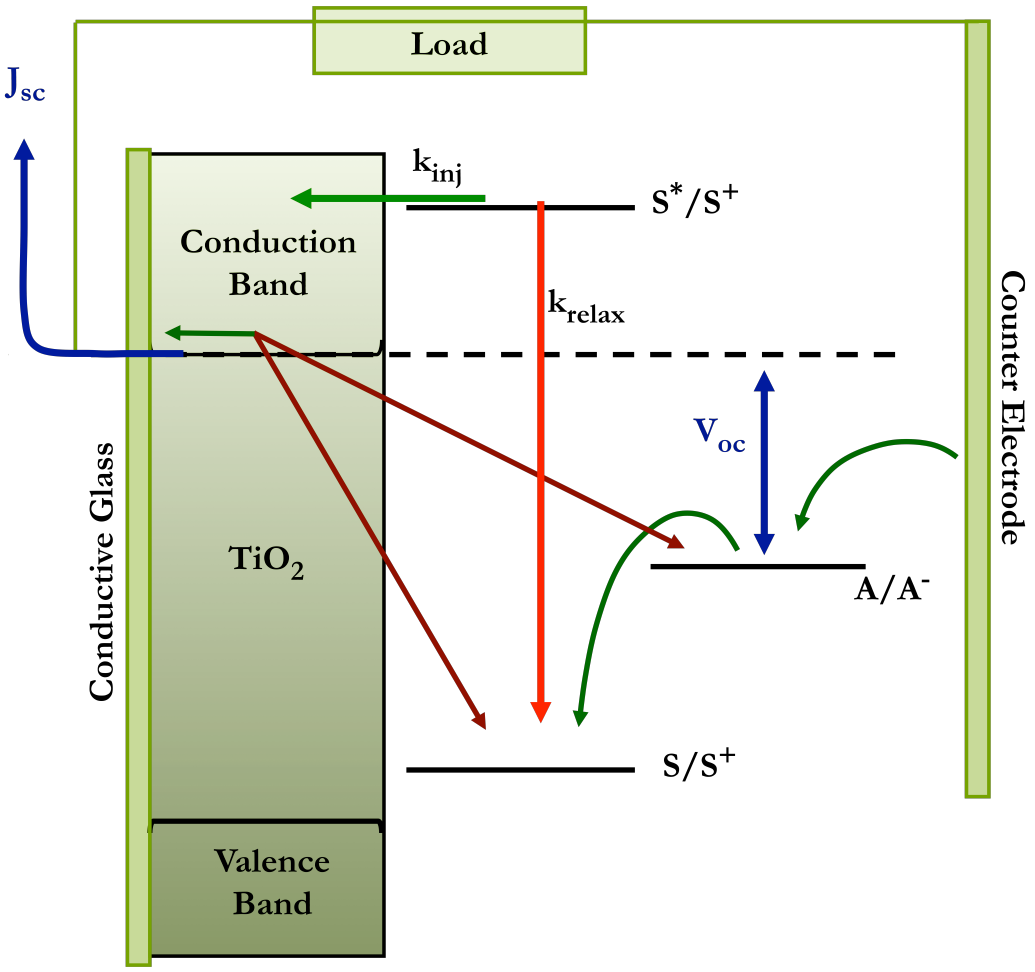

Figure 1-1: Schematic of the generic dye-sensitized solar cell. Green arrows indicate movement of electrons in the ideal case. Red arrows indicate short circuit processes that decrease overall cell efficiency. Blue arrows indicate values measured to determine the efficiency of the cell. For interpretation of the references to color in this and all other figures, the reader is referred to the electronic version of this dissertation.

Kinetic processes representing ideal electron movement through the cell are shown in green while processes reducing overall efficiency of the cells are shown in red. State-of-the-art DSSCs use ruthenium (II)-based sensitizers, indium-doped glass, and platinum counter

electrodes along with volatile organic solvents in the electrolyte. In the beginning, these materials were used to produce the most efficient cells and develop an understanding for how this complicated device works. Despite successful initial improvements, efficiency enhancement has leveled off for nearly 15 years despite continued research on these devices. Research on DSSCs has historically been predominantly conducted on ruthenium (II)-based dyes.[11-15] These complexes contain all that is considered necessary for good sensitizers: large extinction coefficients over the solar spectrum, stable redox behavior, long-lived charge transfer excited states, and excited state energetics thermodynamically favorable for electron injection. Despite the advantages of using ruthenium (II), improvement of device performance has reached a plateau. This, coupled with a small elemental abundance and the high cost of the dye (~30% of the cell cost)[16], precludes the long-term success and scalability of ruthenium-based devices. It is the intention of this research project to improve the efficiency/cost ratio of DSSCs through the replacement of ruthenium (II) in the dye with first row transition metals. The work presented in this dissertation, along with continued effort from others involved in the project, will focus on iron (II). Not only will switching metals decrease the cost of the dye, but it may also open opportunities for substitution of the platinum counter electrode with cheaper and more abundant materials.

Low spin iron (II) was chosen as the initial first row transition metal to study for a number of reasons. First, it is isoelectronic with ruthenium (II) and has the advantage of being extensively studied both photophysically and chemically. Second, the cost and abundance difference between the two metals is large and can make a big impact on overall

cell cost and scalability. Third, previous work has shown the production of a photocurrent from a DSSC with an iron-based sensitizer, albeit 50-times smaller than for the ruthenium analog, suggesting the potential for an iron-based cell and definitely proving the need to examine the possibility.[17]

In 1991, Grätzel reported a dramatic increase in dye-sensitized solar cell efficiency by changing the morphology of the semiconducting substrate from a single crystal to nanoporous TiO_2.[14] Seven years later, Ferrere and Gregg replaced the Ru^{2+} dye with an Fe^{2+} analog in a working cell.[17] Keeping all other materials in the cell constant, a small, but detectable, photocurrent was produced. The overall efficiency of the cell was 100 times smaller than for the Ru^{2+}-based cell, but the principle was proven: electrons can be collected from a photoexcited iron (II)-based dye in a DSSC. Unfortunately, this research was abandoned after only a few reports due to the discouragingly low overall efficiencies of the cells.[18,19] The efficiency of a cell is calculated using Equation 1

$$\eta = \frac{P_{out}}{P_{in}} = \frac{J_{sc} V_{oc}\, ff}{P_{in}} \qquad \text{Equation 1}$$

where η is the efficiency of the cell, P_{in} is the incident power, P_{out} is the power produced by the cell, J_{sc} is the short circuit current density (number of electrons through the cell per unit area), V_{oc} is the open circuit voltage (potential associated with each electron), and ff is the fill factor (measure of how "ideally" the cell behaves and can be influenced by many

factors including electrolyte concentration, homogeneity of the TiO_2 film, etc.). Figure 2 presents a graphical representation of Equation 1.

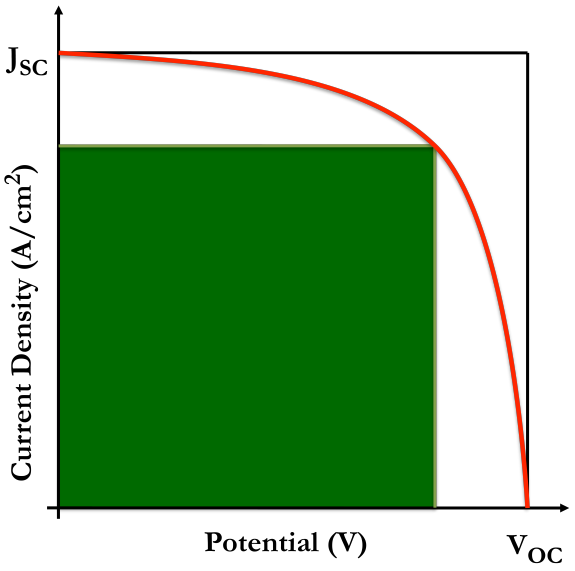

Figure 1-2: Generic J-V curve used to measure parameters associated with cell efficiency as shown in Equation 1. The red line represents the measured current as a function of applied voltage. The area of the black box represents the product of the V_{oc} and the J_{sc} and is the maximum possible power out of the cell. The green box represents the power out of the cell at the point where the product of the measured current and voltage is the maximum. The percentage of the black box that is filled by the green box is the fill factor.

With an understanding of how efficiency is determined and which factors can improve it, a closer look at the cell conditions and measured parameters provides helpful insights into how an Fe^{2+}-based cell might be improved. First, the biggest factor in efficiency reduction is observed in the J_{sc}. Simply put, fewer electrons make it through the iron (II)-based cell than for the ruthenium (II)-based analog. An understanding of why this discrepancy occurs can lead to intelligent modifications of the dye and/or cell conditions in order to improve this value.

With evidence that current density (J_{SC}) is the biggest source of efficiency loss in the iron (II)-based cell, it is instructive to compare the electronic structures of iron (II) and ruthenium (II) as shown in Figure 3. While both complexes are initially excited into metal-to-ligand charge transfer (MLCT) states, low-energy ligand field states in iron (II) that lie below the semiconductor conduction band present deactivation pathways, decreasing the number of injected electrons. These ligand field states are higher in energy for ruthenium and are positioned at more negative potentials than the charge transfer states.[13] Unlike in ruthenium, where the lifetime of the charge transfer state is long compared to electron injection time, the presence of low energy ligand field states serves to shorten the charge transfer lifetime in the iron complexes resulting in a decreased number of electrons that can be injected. Fewer injected electrons means fewer electrons available for movement through the cell, which decreases the short circuit current. The open circuit voltage will also decrease with the loss of injection yield due to the correlation between electron population in the conduction band and the Fermi level that determines the potential available to each electron.[20] In order to improve these quantities (and overall cell efficiency), the injection rate must be competitive with charge transfer state deactivation. A 90% injection yield requires an injection rate ten-times faster than the competing relaxation rate, while 99% injection requires 100 times faster injection compared to relaxation. Although the injection yields for these cells have not been measured, it can be assumed that they are quite low due to the small photocurrent and photovoltage values.

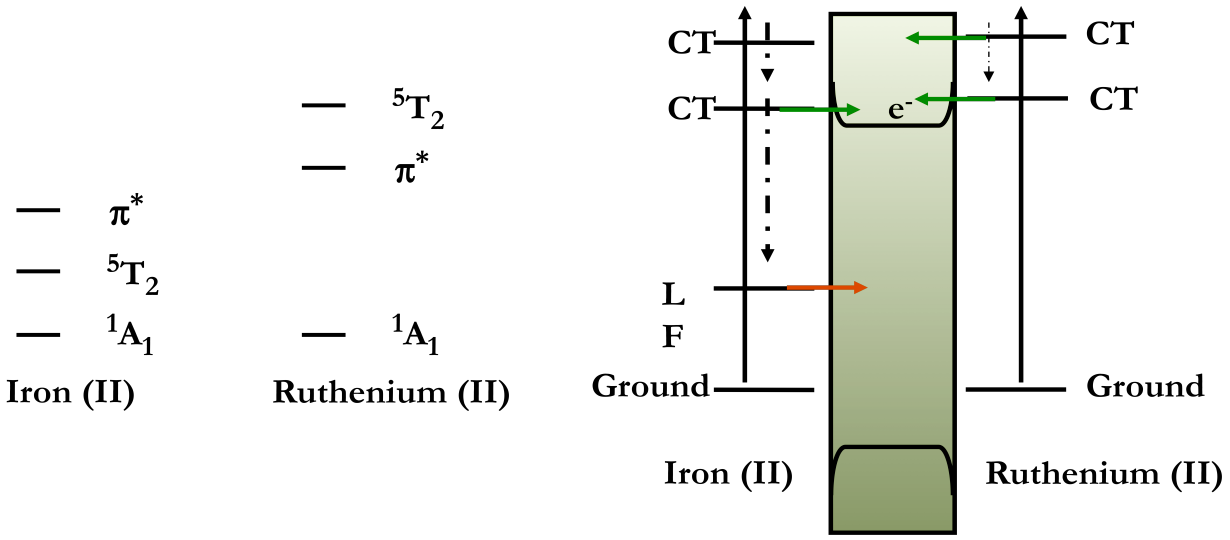

Figure 1-3: Comparison of the electronic structure of Ru^{2+} and Fe^{2+} alone and against the band structure of a semiconductor.

With the intention to measure the injection dynamics from cells based on any sensitizers deemed promising, it is necessary to have a comprehensive understanding of how this process is identified and measured spectroscopically as well as what timescales are appropriate for detection. Turning to the literature, it is seen that many reports on this topic are available.

Many techniques are used to determine the timescale for electron injection in dye-sensitized solar cells.[21-24] Some of the more widely used are visible and near-IR transient absorption spectroscopy[25-30], mid-IR transient absorption spectroscopy[31-55], terahertz spectroscopy[56-59], and time resolved emission spectroscopy[60,61]. Each of these techniques has the advantage of strong, well-characterized signals corresponding to electron injection as well as the timescale necessary to detect the fast component of electron injection. Other, less utilized, experiments include time resolved microwave conductivity[62,63], transient X-

Ray absorption spectroscopy[64,65], surface photovoltage[66,67], photoacoustic spectroscopy[68], microscopic imaging[69,70], confocal fluorescence microscopy[71], and diffuse reflectance transient absorption spectroscopy[72]. Many of these are either in their infancy as a technique used for electron injection detection or they lack the timescale or strong signal required for such a sensitive measurement.

Much work has been done to study the electron injection rates on dry films and full solar cells as a function of semiconductor[73-75], electrolyte composition[76], and excitation energy[77] as well as variations in the sensitizer such as anchoring group[78-80], bridge length[81,82], and energetics[83,84] compared to the conduction band edge.[25,85] From these works, it is clear that every aspect of the dye-sensitized solar cell plays an important role in the efficiency of the entire device. This provides impetus for the optimization of any cell with a new sensitizer deemed worthy of study, making the selection of such a sensitizer a balance of time and performance.

As previously stated, iron (II) polypyridyl complexes have been extensively studied both chemically and photophysically. Although the predominant absorption features in these complexes are charge transfer in nature, numerous studies have assigned the long-lived excited state of low spin Fe^{2+} complexes to a metal-centered ligand field state.[86,87] This state lives between hundreds of picoseconds to hundreds of nanoseconds, depending on the ligand set. Observation of the formation of this state, however, has only recently been possible. As time resolution on transient absorption, emission, raman, and X-Ray experiments has improved in recent years, processes on shorter timescales have become

measurable. Through the use of ultrafast (sub-ps) spectroscopy, direct measurements of both the charge transfer state as well as the conversion to the ligand field state have been possible.[88-95]

Previous work in the McCusker group has provided a firm foundation on which to advance iron (II)-based kinetic studies. A series of experiments by Jeremy Monat and Amanda Smeigh uncovered clear spectroscopic tags for examining the transition from the initial charge transfer excited state to the long-lived ligand field state(s).[88,96,97] A pair of molecules - one low spin and one high spin - that will be discussed in more detail in chapter 3 have ground and low-lying ligand field excited states that are inverted. The transient absorption difference spectrum for the low spin complex was measured on the femtosecond timescale and compared to the difference spectrum that was calculated from the ground states of both complexes. Both calculated and measured spectra were in agreement and represented the difference spectrum of the lowest-lying ligand field excited state of the low-spin complex.

Concurrently, spectroelectrochemical data were collected to observe the spectra associated with the oxidized and reduced forms of the complex, providing spectral information pertaining to the charge transfer excited state. Combining the oxidized metal center data with the reduced ligand information gave a rough estimate of the features that would prevail from the metal-to-ligand charge transfer state of the complex. By probing a region of the spectrum where one species (MLCT) has a positive signal and the other (ligand field) has a negative signal, Monat and Smeigh were able to confidently determine the timescale associated with the transition from one state to the other. This process was

measured to be less than 100 fs. With the appropriate spectroscopic tag in hand, the MLCT state deactivation times for several more Fe^{2+}-polypyridyl complexes have been measured, all with similar results.[98,99] Progress to modulate the timescale of this process is ongoing and will be discussed throughout this document.

Chapter 2 describes the experimental procedures used to measure the steady state and time-resolved photophysics of these molecules. Along with basic procedures for the group's long-standing techniques, detailed descriptions of spectroelectrochemistry and two femtosecond transient absorption spectrometers will be described, all of which have been set up during the course of this dissertation. The two femtosecond laser systems coupled with the nanosecond TA setup can span sub-50 fs to 100s of μs with no "dark" window, providing the opportunity to gather more information about all of our systems including direct measurement of electron injection dynamics.

In order to validate the numerical values used in the remainder of the dissertation, Chapter 3 will present a set of experiments performed on the previously mentioned Fe^{2+} spin-crossover complexes. A series of four complexes spans the range of low spin at all temperatures to high spin at all temperatures, with two complexes that can sample both spin states to varying degrees as a function of temperature. Thermodynamic, magnetic, and kinetic data for these complexes, which cannot be obtained for non-spin crossover complexes, are combined in order to provide a foundation from which conclusions can be drawn for the low spin complexes in the rest of the document.

Chapter 4 will describe efforts to identify the reaction coordinate responsible for the MLCT state relaxation in Fe^{2+} complexes. A series of substituted iron (II) bisterpyridyl

complexes were synthesized and characterized by Lindsey Jamula; those syntheses and characterizations as well as some calculations will be referenced, but not discussed. Photophysical and electrochemical measurements will be presented on steady state, nanosecond, and femtosecond timescales.

Chapter 5 introduces a new and exciting Fe^{2+} molecule. Originally designed and synthesized for its nearly perfect octahedral geometry, there is strong evidence to support the notion that the splitting of the ligand field is larger than that for $[Fe(CN)_6]^{4-}$. Kinetic and thermodynamic data provide evidence that the ligand field state from which ground state recovery takes place is different than all other known iron(II) complexes, indicating it is in a new excited state regime. The appearance of a weak, but significant emission at low temperatures strengthens the claim. Although this is a remarkable molecule on its own, the oxidation/reduction potentials also place the excited state of the complex in a potentially useful energetic position when attached to a substrate, providing a possibility to be a useful sensitizer in DSSCs. Kinetic, thermodynamic, and spectral data will be discussed in the contexts of fundamental iron(II) photophysics as well as possible applications in solar cells.

Chapter 6 will discuss some new directions and unresolved questions that might be pursued with the continuation of this project. Preliminary pump energy and solvent dependent results will be described along with additional experimental techniques that would provide more information on cell performance and injection dynamics on the complexes in hand as well as new molecules to be studied.

REFERENCES

References: Chapter 1

(1) Kates, R. W. *Environment* **2000**, *42*, 10.

(2) Lewis, N. S.; Nocera, D. G. *Proceedings of the National Academy of Sciences of the United States of America* **2006**, *103*, 15729.

(3) BP *Statistical Review of World Energy*, 2010.

(4) Annual Energy Review, Energy Information Administration, 2010.

(5) *Intergovernmental Panel on Climate Change,* **2007**.

(6) Green, M. A.; Wenham, S. R.; Honsberg, C. B.; Hogg, D. *Solar Energy Materials and Solar Cells* **1994**, *34*, 83.

(7) Avrutin, V.; Izyumskaya, N.; Morkoc, H. *Superlattices and Microstructures* **2011**, *49*, 337.

(8) In *The First Solar, Inc. website*.

(9) http://nsl.caltech.edu/energy; Lewis, N. S.

(10) Basic Research Needs for Solar Energy Utilization, U. S. Department of Energy, 2005.

(11) Ardo, S.; Meyer, G. J. *Chemical Society Reviews* **2009**, *38*, 115.

(12) Jennings, J. R.; Liu, Y.; Wang, Q.; Zakeeruddin, S. M.; Gratzel, M. *Physical Chemistry Chemical Physics* **2011**, *13*, 6637.

(13) Nazeeruddin, M. K.; Kay, A.; Rodicio, I.; Humphrybaker, R.; Muller, E.; Liska, P.; Vlachopoulos, N.; Gratzel, M. *Journal of the American Chemical Society* **1993**, *115*, 6382.

(14) O'regan, B.; Gratzel, M. *Nature* **1991**, *353*, 737.

(15) Clifford, J. N.; Martinez-Ferrero, E.; Viterisi, A.; Palomares, E. *Chemical Society Reviews* **2011**, *40*, 1635.

(16) C.A. Bignozzi, personal communication

(17) Ferrere, S.; Gregg, B. A. *Journal of the American Chemical Society* **1998**, *120*, 843.

(18) Ferrere, S. *Inorganica Chimica Acta* **2002**, *329*, 79.

(19) Ferrere, S. *Chemistry of Materials* **2000**, *12*, 1083.

(20) The Fermi level of a semiconductor is a measure of the type and amount of doping. It represents the relative population of holes in the valence band and electrons in the conduction band. As electrons are "doped" into the conduction band through electron injection, the quasi-Fermi level associated with the semiconductor moves toward the conduction band, increasing the potential difference available to each electron as it moves through the cell.

(21) Xie, Y.; Joshi, P.; Darling, S. B.; Chen, Q. L.; Zhang, T.; Galipeau, D.; Qiao, Q. Q. *Journal of Physical Chemistry C* **2010**, *114*, 17880.

(22) Wang, H. F.; Chen, L. Y.; Su, W. N.; Chung, J. C.; Hwang, B. J. *Journal of Physical Chemistry C* **2010**, *114*, 3185.

(23) Lu, X. J.; Mou, X. L.; Wu, J. J.; Zhang, D. W.; Zhang, L. L.; Huang, F. Q.; Xu, F. F.; Huang, S. M. *Advanced Functional Materials* **2010**, *20*, 509.

(24) Szarko, J. M.; Neubauer, A.; Bartelt, A.; Socaciu-Siebert, L.; Birkner, F.; Schwarzburg, K.; Hannappel, T.; Eichberger, R. *Journal of Physical Chemistry C* **2008**, *112*, 10542.

(25) Watson, D. F.; Meyer, G. J. *Annual Review of Physical Chemistry* **2005**, *56*, 119.

(26) Wiberg, J.; Marinado, T.; Hagberg, D. P.; Sun, L. C.; Hagfeldt, A.; Albinsson, B. *Journal of Physical Chemistry C* **2009**, *113*, 3881.

(27) Morandeira, A.; Boschloo, G.; Hagfeldt, A.; Hammarstrom, L. *Journal of Physical Chemistry C* **2008**, *112*, 9530.

(28) Morandeira, A.; Boschloo, G.; Hagfeldt, A.; Hammarstrom, L. *Journal of Physical Chemistry B* **2005**, *109*, 19403.

(29) Bauer, C.; Boschloo, G.; Mukhtar, E.; Hagfeldt, A. *Chemical Physics Letters* **2004**, *389*, 449.

(30) Benko, G.; Kallioinen, J.; Korppi-Tommola, J. E. I.; Yartsev, A. P.; Sundstrom, V. *Journal of the American Chemical Society* **2002**, *124*, 489.

(31) Takeshita, K.; Sasaki, Y.; Kobashi, M.; Tanaka, Y.; Maeda, S.; Yamakata, A.; Ishibashi, T.; Onishi, H. *Journal of Physical Chemistry B* **2003**, *107*, 4156.

(32) Morandeira, A.; Lopez-Duarte, I.; Martinez-Diaz, M. V.; O'Regan, B.; Shuttle, C.; Haji-Zainulabidin, N. A.; Torres, T.; Palomares, E.; Durrant, J. R. *Journal of the American Chemical Society* **2007**, *129*, 9250.

(33) Palomares, E.; Martinez-Diaz, M. V.; Haque, S. A.; Torres, T.; Durrant, J. R. *Chemical Communications* **2004**, 2112.

(34) Tachibana, Y.; Nazeeruddin, M. K.; Gratzel, M.; Klug, D. R.; Durrant, J. R. *Chemical Physics* **2002**, *285*, 127.

(35) Tachibana, Y.; Haque, S. A.; Mercer, I. P.; Durrant, J. R.; Klug, D. R. *Journal of Physical Chemistry B* **2000**, *104*, 1198.

(36) Durrant, J. R.; Tachibana, Y.; Moser, J. E.; Gratzel, M.; Klug, D. R. *Proceedings of the Indian Academy of Sciences-Chemical Sciences* **1997**, *109*, 411.

(37) Tachibana, Y.; Moser, J. E.; Gratzel, M.; Klug, D. R.; Durrant, J. R. *Journal of Physical Chemistry* **1996**, *100*, 20056.

(38) Cavalleri, A.; Rini, M.; Schoenlein, R. W. *Journal of the Physical Society of Japan* **2006**, *75*.

(39) Asbury, J. B.; Hao, E.; Wang, Y. Q.; Ghosh, H. N.; Lian, T. Q. *Journal of Physical Chemistry B* **2001**, *105*, 4545.

(40) Wang, Y. Q.; Asbury, J. B.; Lian, T. Q. *Journal of Physical Chemistry A* **2000**, *104*, 4291.

(41) Anderson, N. A.; Hang, K.; Asbury, J. B.; Lian, T. Q. *Chemical Physics Letters* **2000**, *329*, 386.

(42) Asbury, J. B.; Ellingson, R. J.; Ghosh, H. N.; Ferrere, S.; Nozik, A. J.; Lian, T. Q. *Journal of Physical Chemistry B* **1999**, *103*, 3110.

(43) Ghosh, H. N.; Asbury, J. B.; Weng, Y. X.; Lian, T. Q. *Journal of Physical Chemistry B* **1998**, *102*, 10208.

(44) Stockwell, D.; Yang, Y.; Huang, J.; Anfuso, C.; Huang, Z. Q.; Lian, T. Q. *Journal of Physical Chemistry C* **2010**, *114*, 6560.

(45) Huang, J.; Stockwell, D.; Boulesbaa, A.; Guo, J. C.; Lian, T. Q. *Journal of Physical Chemistry C* **2008**, *112*, 5203.

(46) Guo, J. C.; Stockwell, D.; Ai, X.; She, C. X.; Anderson, N. A.; Lian, T. Q. *Journal of Physical Chemistry B* **2006**, *110*, 5238.

(47) Ai, X.; Anderson, N. A.; Guo, J. C.; Lian, T. Q. *Journal of Physical Chemistry B* **2005**, *109*, 7088.

(48) Lenchenkov, V. A.; She, C. X.; Lian, T. Q. *Journal of Physical Chemistry B* **2004**, *108*, 16194.

(49) Ai, X.; Guo, J. C.; Anderson, N. A.; Lian, T. Q. *Journal of Physical Chemistry B* **2004**, *108*, 12795.

(50) Anderson, N. A.; Ai, X.; Lian, T. Q. *Journal of Physical Chemistry B* **2003**, *107*, 14414.

(51) Anderson, N. A.; Ai, X.; Chen, D. T.; Mohler, D. L.; Lian, T. Q. *Journal of Physical Chemistry B* **2003**, *107*, 14231.

(52) Asbury, J. B.; Wang, Y. Q.; Hao, E. C.; Ghosh, H. N.; Lian, T. Q. *Research on Chemical Intermediates* **2001**, *27*, 393.

(53) Ellingson, R. J.; Asbury, J. B.; Ferrere, S.; Ghosh, H. N.; Sprague, J. R.; Lian, T.; Nozik, A. J. *Zeitschrift Fur Physikalische Chemie-International Journal of Research in Physical Chemistry & Chemical Physics* **1999**, *212*, 77.

(54) Asbury, J. B.; Wang, Y. Q.; Lian, T. Q. *Journal of Physical Chemistry B* **1999**, *103*, 6643.

(55) Ghosh, H. N.; Asbury, J. B.; Lian, T. Q. *Journal of Physical Chemistry B* **1998**, *102*, 6482.

(56) Pijpers, J. J. H.; Ulbricht, R.; Derossi, S.; Reek, J. N. H.; Bonn, M. *Journal of Physical Chemistry C* **2011**, *115*, 2578.

(57) Nemec, H.; Rochford, J.; Taratula, O.; Galoppini, E.; Kuzel, P.; Polivka, T.; Yartsev, A.; Sundstrom, V. *Physical Review Letters* **2010**, *104*.

(58) Nemec, H.; Kuzel, P.; Kadlec, F.; Fattakhova-Rohlfing, D.; Szeifert, J.; Bein, T.; Kalousek, V.; Rathousky, J. *Applied Physics Letters* **2010**, *96*.

(59) Abuabara, S. G.; Cady, C. W.; Baxter, J. B.; Schmuttenmaer, C. A.; Crabtree, R. H.; Brudvig, G. W.; Batista, V. S. *Journal of Physical Chemistry C* **2007**, *111*, 11982.

(60) Koops, S. E.; O'Regan, B. C.; Barnes, P. R. F.; Durrant, J. R. *Journal of the American Chemical Society* **2009**, *131*, 4808.

(61) Verma, S.; Kar, P.; Das, A.; Palit, D. K.; Ghosh, H. N. *Journal of Physical Chemistry C* **2008**, *112*, 2918.

(62) Katoh, R.; Kasuya, M.; Furube, A.; Fuke, N.; Koide, N.; Han, L. Y. *Solar Energy Materials and Solar Cells* **2009**, *93*, 698.

(63) Katoh, R.; Huijser, A.; Hara, K.; Savenije, T. J.; Siebbeles, L. D. A. *Journal of Physical Chemistry C* **2007**, *111*, 10741.

(64) Zhang, X. Y.; Smolentsev, G.; Guo, J. C.; Attenkofer, K.; Kurtz, C.; Jennings, G.; Lockard, J. V.; Stickrath, A. B.; Chen, L. X. *Journal of Physical Chemistry Letters* **2011**, *2*, 628.

(65) Lee, K. E.; Gomez, M. A.; Regier, T.; Hu, Y. F.; Demopoulos, G. P. *Journal of Physical Chemistry C* **2011**, *115*, 5692.

(66) Lenzmann, F.; O'Regan, B.; Wienke, J.; Huisman, C.; Reijnen, L.; Goossens, A. *Physica E-Low-Dimensional Systems & Nanostructures* **2002**, *14*, 233.

(67) Lenzmann, F.; Krueger, J.; Burnside, S.; Brooks, K.; Gratzel, M.; Gal, D.; Ruhle, S.; Cahen, D. *Journal of Physical Chemistry B* **2001**, *105*, 6347.

(68) Serpa, C.; Schabauer, J.; Piedade, A. P.; Monteiro, C. J. P.; Pereira, M. M.; Douglas, P.; Burrows, H. D.; Arnaut, L. G. *Journal of the American Chemical Society* **2008**, *130*, 8876.

(69) Liu, R. C. *Journal of Physical Chemistry C* **2009**, *113*, 9368.

(70) Katoh, R.; Furube, A.; Tamaki, Y.; Yoshihara, T.; Murai, M.; Hara, K.; Murata, S.; Arakawa, H.; Tachiya, M. *J. Photochem. Photobiol. A-Chem.* **2004**, *166*, 69.

(71) Chen, Y. J.; Tzeng, H. Y.; Fan, H. F.; Chen, M. S.; Huang, J. S.; Lin, K. C. *Langmuir* **2010**, *26*, 9050.

(72) Furube, A.; Wang, Z. S.; Sunahara, K.; Hara, K.; Katoh, R.; Tachiya, M. *Journal of the American Chemical Society* **2010**, *132*, 6614.

(73) Zhang, J. Z. *Accounts of Chemical Research* **1997**, *30*, 423.

(74) Tiwana, P.; Docampo, P.; Johnston, M. B.; Snaith, H. J.; Herz, L. M. *Acs Nano* **2011**, *5*, 5158.

(75) Furube, A.; Murai, M.; Watanabe, S.; Hara, K.; Katoh, R.; Tachiya, M. *J. Photochem. Photobiol. A-Chem.* **2006**, *182*, 273.

(76) Zhang, C. N.; Huo, Z. P.; Huang, Y.; Dai, S. Y.; Wang, M.; Tang, Y. T.; Sui, Y. F. *J. Photochem. Photobiol. A-Chem.* **2010**, *213*, 87.

(77) Katoh, R.; Furube, A.; Murai, M.; Tamaki, Y.; Hara, K.; Tachiya, M. *Comptes Rendus Chimie* **2006**, *9*, 639.

(78) Kar, P.; Verma, S.; Sen, A.; Das, A.; Ganguly, B.; Ghosh, H. N. *Inorganic Chemistry* **2010**, *49*, 4167.

(79) Gajardo, F.; Leiva, A. M.; Loeb, B.; Delgadillo, A.; Stromberg, J. R.; Meyer, G. J. *Inorganica Chimica Acta* **2008**, *361*, 613.

(80) Park, H.; Bae, E.; Lee, J. J.; Park, J.; Choi, W. *Journal of Physical Chemistry B* **2006**, *110*, 8740.

(81) Wang, X. F.; Tamiaki, H.; Wang, L.; Tamai, N.; Kitao, O.; Zhou, H. S.; Sasaki, S. *Langmuir* **2010**, *26*, 6320.

(82) Paoprasert, P.; Laaser, J. E.; Xiong, W.; Franking, R. A.; Hamers, R. J.; Zanni, M. T.; Schmidt, J. R.; Gopalan, P. *Journal of Physical Chemistry C* **2010**, *114*, 9898.

(83) Listorti, A.; Lopez-Duarte, I.; Martinez-Diaz, M. V.; Torres, T.; DosSantos, T.; Barnes, P. R. F.; Durrant, J. R. *Energy & Environmental Science* **2010**, *3*, 1573.

(84) Wiberg, J.; Marinado, T.; Hagberg, D. P.; Sun, L. C.; Hagfeldt, A.; Albinsson, B. *Journal of Physical Chemistry B* **2010**, *114*, 14358.

(85) Anderson, N. A.; Lian, T. Q. *Annual Review of Physical Chemistry* **2005**, *56*, 491.

(86) Creutz, C.; Chou, M.; Netzel, T. L.; Okumura, M.; Sutin, N. *Journal of the American Chemical Society* **1980**, *102*, 1309.

(87) Bergkamp, M. A.; Brunschwig, B. S.; Gutlich, P.; Netzel, T. L.; Sutin, N. *Chemical Physics Letters* **1981**, *81*, 147.

(88) Juban, E. A.; Smeigh, A. L.; Monat, J. E.; McCusker, J. K. *Coordination Chemistry Reviews* **2006**, *250*, 1783.

(89) Khalil, M.; Marcus, M. A.; Smeigh, A. L.; McCusker, J. K.; Chong, H. H. W.; Schoenlein, R. W. *Journal of Physical Chemistry A* **2006**, *110*, 38.

(90) Smeigh, A. L.; Creelman, M.; Mathies, R. A.; McCusker, J. K. *Journal of the American Chemical Society* **2008**, *130*, 14105.

(91) Gawelda, W.; Cannizzo, A.; Pham, V. T.; van Mourik, F.; Bressler, C.; Chergui, M. *Journal of the American Chemical Society* **2007**, *129*, 8199.

(92) Gawelda, W.; Pham, V. T.; Benfatto, M.; Zaushitsyn, Y.; Kaiser, M.; Grolimund, D.; Johnson, S. L.; Abela, R.; Hauser, A.; Bressler, C.; Chergui, M. *Physical Review Letters* **2007**, *98*.

(93) Bressler, C.; Milne, C.; Pham, V. T.; ElNahhas, A.; van der Veen, R. M.; Gawelda, W.; Johnson, S.; Beaud, P.; Grolimund, D.; Kaiser, M.; Borca, C. N.; Ingold, G.; Abela, R.; Chergui, M. *Science* **2009**, *323*, 489.

(94) Cannizzo, A.; Milne, C. J.; Consani, C.; Gawelda, W.; Bressler, C.; van Mourik, F.; Chergui, M. *Coordination Chemistry Reviews* **2010**, *254*, 2677.

(95) Milne, C.; Pham, V. T.; Gawelda, W.; Nahhas, A. E.; van der Veen, R. M.; Johnson, S. L.; Beaud, P.; Ingold, G.; Borca, C.; Grolimund, D.; Abela, R.; Chergui, M.; Bressler, C. *Acta Physica Polonica A* **2010**, *117*, 391.

(96) Monat, J. E.; Rodriguez, J. H.; McCusker, J. K. *Journal of Physical Chemistry A* **2002**, *106*, 7399.

(97) Monat, J. E.; McCusker, J. K. *Journal of the American Chemical Society* **2000**, *122*, 4092.

(98) Smeigh, A. L., Michigan State University, 2007.

(99) Smeigh, A. L., Brown, A. M., McCusker, J. K. *Manuscript in Preparation* **2011**.

Chapter 2: Experimental

The methods used to collect the data presented throughout this dissertation will be described in this chapter. The experimental procedures will be explained from both a theoretically and practical point of view. The techniques that will be discussed include steady state electronic absorption, steady state low temperature emission, electrochemistry, spectroelectrochemistry, variable temperature Evan's method NMR, variable temperature nanosecond transient absorption, and femtosecond transient absorption. All physical and photophysical measurements were carried out in solutions of spectrophotometric grade solvents.

Steady-state Electronic Absorption and Emission

Ground state electronic absorption spectra were recorded on a Cary-50 UV-visible spectrophotometer in a 1 cm quartz cuvette. Extinction coefficients were measured using serial dilutions of a known concentration. Beer's law is given by Equation 1

$$A = \varepsilon \ell c \qquad \text{Equation 1}$$

where A is the absorbance, ε is the extinction coefficient in $M^{-1}cm^{-1}$, ℓ is the length of the cuvette, and c is the concentration of the solution. The wavelength dependent absorbance spectrum of each solution was measured for a series of 4-5 concentrations. Absorbance values were plotted against solution concentration and the slope of the line was calculated to give the wavelength dependent extinction coefficient.

Steady state emission was carried out on a Horiba Florolog with a Hamamatsu R5108 photomultiplier tube detector powered by a Stanford Research Systems PS325 high voltage supply and cooled by a C9143 thermoelectric cooler. Liquid nitrogen temperatures were

attained using a Janis Research Co., Inc. ST-100 optical dewar. Due to low emission levels of the complex studied, slit widths for both the excitation and emission monochromators were large, increasing the detectable light, but decreasing the spectral resolution.

Electrochemistry and Spectroelectrochemistry

Electrochemical measurements were carried out in an argon atmosphere glovebox (Vacuum Atmospheres) using a BAS CV-50W electrochemical analyzer. A standard three-electrode arrangement was used consisting of a Pt disk working electrode, a graphite rod counter electrode, and a $Ag/AgNO_3$ or Ag/AgCl reference electrode. Measurements were carried out in a 0.1 M $TBAPF_6$ supporting electrolyte solution of spectrophotometric grade acetonitrile, which was freeze-pump-thaw degassed before use. Cyclic voltammetry was used to determine the ligand reduction and metal oxidation potentials for each complex. Reduction and oxidation $E_{1/2}$ potentials were calculated as the average of the anodic and cathodic wave peaks for each process. The ferrocene/ferrocenium redox couple was used as an external reference for each sample. Values are reported referenced to NHE unless otherwise stated.

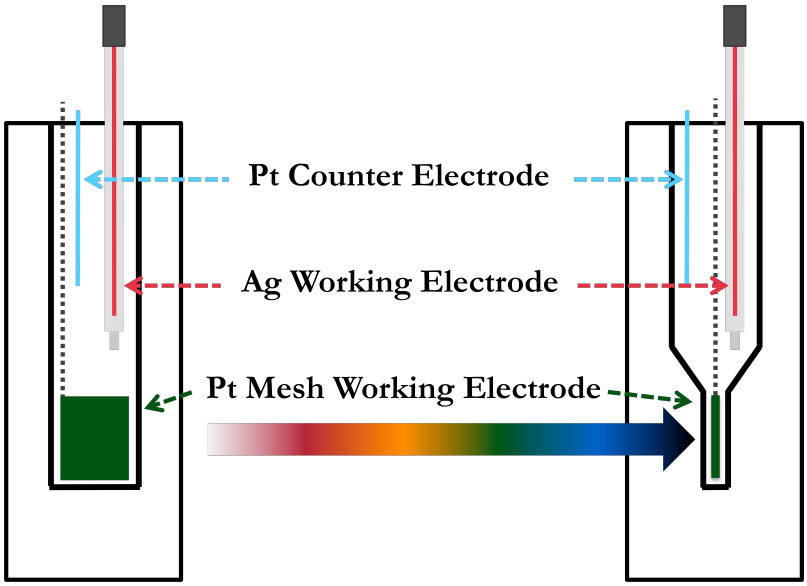

Figure 2-1: Dual path-length spectroelectrochemical cell.

UV-visible spectroelectrochemical experiments were performed in a dual-path length spectroelectrochemical cell (CHI140A, CH Instruments, Figure 1) in an Ar-filled glovebox (Vacuum Atmospheres). The 1 cm x 1 cm space on the top of the cell holds the $Ag/AgNO_3$ or Ag/AgCl reference electrode and platinum or silver wire counter electrode while the platinum mesh working electrode fit into the 1 mm x 1 cm path length bottom of the cell to electrolyze the solution while it is interrogated by light with a SI400 CCD spectrometer. Measurements were performed in spectrophotometric grade acetonitrile, which was freeze-pump-thaw degassed before use, along with 0.1 M $TBAPF_6$ as the supporting electrolyte. Solutions of each complex and supporting electrolyte were adjusted to have absorbance values between 0.6-0.8 at the ground state MLCT peak. No stirring occurred during the experiment. An overpotential of 100-200 mV past the first oxidation/reduction peak was applied to the sample in a chronoampometry experiment. Spectra were collected against a background of the solution without the molecule (electrolyte was part of the

blank spectrum). One 10 mL sample solution was prepared from which a 1 mL aliquot of the stock solution was used to fill the sample cell for each oxidative or reductive experiment. A ground state spectrum was taken before electrolysis began. Once electrolysis began, spectra were taken every 20-30 seconds for 20 minutes. The level of completion varied slightly as a function of the overpotential used and the specific positions of the electrodes in relation to each other.

Each spectroelectrochemical measurement was repeated 3-4 times. The most representative spectrum of each species (ground, oxidized, reduced) is presented. The SI400 CCD spectrometer uses two lamps (deuterium and tungsten) to produce the wide wavelength range, and a discontinuity at 475 nm can be seen in some spectra due to the difference in intensity at the changeover between the two lamps.

Because the excited state of interest is MLCT in nature, a combination of the spectra from the oxidized species, the reduced species, and the ground state species can simulate the excited state spectrum through the use of Equations 2 and 3.

$$\varepsilon_{ex} = \varepsilon_{ox} + \varepsilon_{red} - \varepsilon_{gr} \qquad \text{Equation 2}$$

$$\Delta A = (\varepsilon_{ex} - \varepsilon_{gr}) b \left[C_{gr} \right] \eta \qquad \text{Equation 3}$$

where ε_X is the extinction coefficient of the excited state, ground state, oxidized species, or reduced species, C_{gr} is the concentration of the ground state, and η is the percentage of photoinduced excited state created during the laser experiment or assumed for the calculation. In the complexes of interest (and by definition in any MLCT excited state), reduction of the molecule places an electron on the ligand and oxidation removes one from the metal as shown in Figure 2.

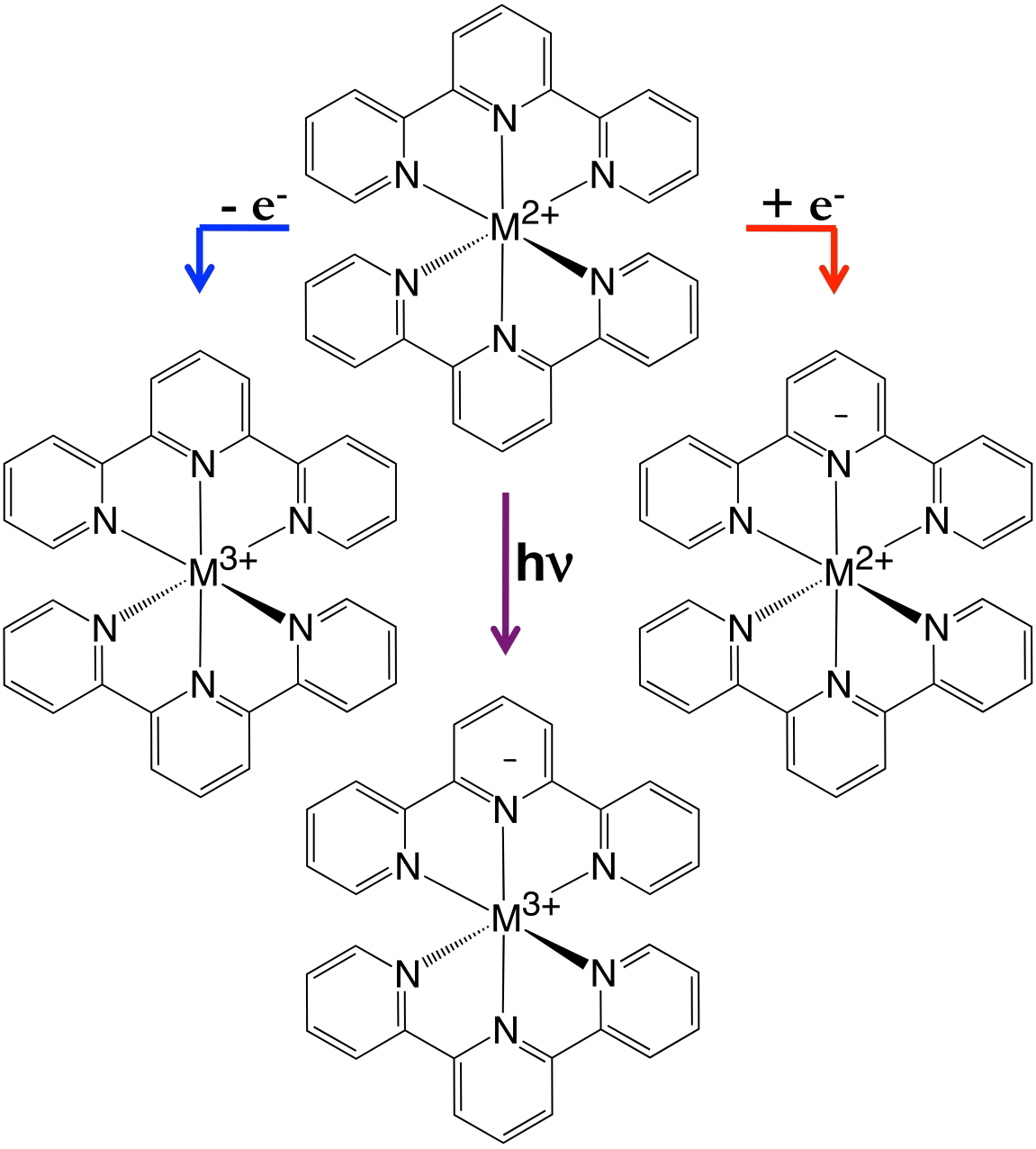

Figure 2-2: Oxidized, reduced, and photoexcited $[M^{2+}(terpy)_2]^{2+}$ complex. The metal center of the oxidized species combined with the ligand set of the reduced species can be combined to model the photoexcited species.

Figure 3 shows spectra for the ground, oxidized, and reduced species of $[Fe(terpy)_2]^{2+}$ along with the calculated ΔA spectrum compared to the photoinduced ΔA spectrum. This calculation included an η value of 0.17, meaning 17% of the ground state was excited. This

calculated spectrum does not take into consideration discrepancies between the photoexcited species and the modeled excited species, which are listed in Tables 1 and 2, but matches the photoinduced excited state pretty well. Considering that the purpose for this measurement and calculation is to identify wavelengths where the MLCT and ligand field excited states absorb differently, the level of accuracy afforded by this method is sufficient.

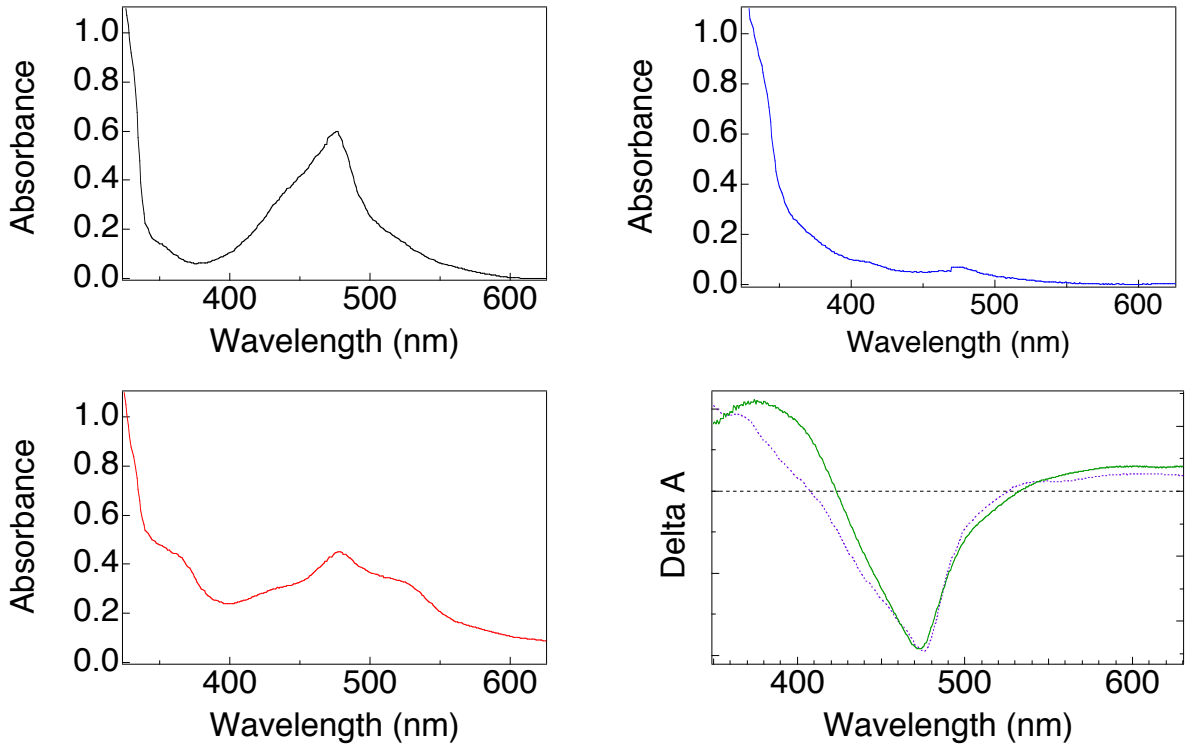

Figure 2-3: Electronic absorption spectra for the ground (black), oxidized (blue), and reduced (red) $[Ru(terpy)_2]^{2+}$ are shown and used in equations 2 and 3 to get the calculated spectrum. Photoinduced (green) and calculated (purple) change in absorbance spectra are compared with 30% excited state used in the model.

As seen in Table 2, the calculated spectrum is expected to differ from the measured photoexcited spectrum because three interactions are calculated that do not exist in the photoexcited species, and one interaction that is present cannot be calculated. Despite these inconsistencies, the measured and calculated spectra correlate quite well, as seen for

$[Ru(terpy)_2]^{2+}$ in Figure 1. In circumstances where the spectra do not match exactly, the inconsistencies can be explained by the discrepancies in the calculated versus measured complex. The features from both the reduced and oxidized species are still present and can be used to identify the type of state seen in the transient absorption data.

Table 2-1: Ligand and metal species along with interactions present in each of the ground, oxidized, and reduced forms of the generic $[ML_2]^{2+}$ complex.

Ground State	Oxidized Species	Reduced Species
M^{2+}	M^{3+}	M^{2+}
L_1	L_1	L_1^-
L_2	L_2	L_2
M^{2+} - L_1	M^{3+} - L_1	M^{2+} - L_1^-
M^{2+} - L_2	M^{3+} - L_2	M^{2+} - L_2

Table 2-2: Ligand and metal species along with interactions present in the calculated and photoexcited $[ML_2]^{2+}$ complex.

Calculated	Measured
L_1^-	L_1^-
L_2	L_2
M^{3+} - L_1	M^{3+} - L_1^-
M^{3+} - L_2	M^{3+} - L_2
M^{3+}	M^{3+}
M^{2+} - L_1^-	
- (M^{2+} - L_1)	

Variable Temperature Evan's Method NMR

Nuclear magnetic resonance (NMR) is a widely employed experimental technique typically used for identification and characterization of diamagnetic complexes.[1] Selected atoms in the molecule are interrogated with a magnetic pulse and the shift associated with relaxation for each atom is highly sensitive to its surrounding environment. Typical experiments measure the shifts of atomic isotopes with respect to one another and information is gleaned from the magnitudes and patterns of the peaks. Paramagnetic contributions mask most of the useful information by broadening peaks. Evan's method NMR takes advantage of both the sensitivity of the shift to the environment and the contribution a paramagnetic species has to that environment. From these data, magnetic properties of a molecule may be collected.

Concentric NMR tubes are used in this experiment: both the inner tube and outer tube contain deuterated solvent spiked with a standard while the outer tube also has a known concentration of the molecule of interest dissolved. The shift of the peak associated with the standard is measured. Due to the different magnetic environments felt by the standard in the inner and outer tubes, the peaks will appear at different fields. The magnitude of the change in shifts is dependent on the field of the spectrometer, the concentration of the sample, and the number of unpaired electrons in the sample, as shown in Equation 4:

$$\mathrm{X}_M = \frac{3000 * \Delta\nu}{4\pi\nu[C]} \qquad \text{Equation 4}$$

where χ_M is the measured susceptibility, ν is the frequency of the spectrometer, Δν is the difference in the peak shifts, and [C] is the concentration of the sample.

In most molecules, the number of unpaired electrons is constant over the temperature range of interest. However, those that fall into the class of spin-crossover complexes can have a very large variation in number of unpaired electrons as a function of temperature. For this reason, measurements are collected over a range of temperatures to determine the temperature-dependent magnetic properties of the complex. Temperature readings were performed with a methanol standard (an NMR tube with spectroscopic grade, but NOT deuterated, methanol). Shimming was performed prior to data collection at all temperatures, but locking and shimming is not necessary (or possible) for the methanol standard.

Data was collected in duplicate on a ~ 10 mM sample in deuterated acetone from ~ -70 °C to 30 °C on a 500 MHz spectrometer (Anubis). Temperature variation was performed with a water chiller and was determined using a methanol standard at each temperature by measuring the difference between the methyl and alcohol proton peaks. Once the temperature was adjusted, sample spectra were collected until the separation between the peaks was no longer changing. The temperature was recorded and the sample of interest was inserted. A fifteen-minute waiting period followed, which included periodic checks of the standard peaks to assure a constant temperature was reached. The sample was then collected for 32 scans. The difference in the peaks was recorded and reported as magnetic data using Equation 4. Magnetic susceptibility (X) data allowed the calculation of mole fractions of high spin and low spin Fe^{2+} using Equations 5, 6, and 7

$$m_{hs} = \frac{(\mathrm{X}_m - \mathrm{X}_{ls})}{(\mathrm{X}_{hs} - \mathrm{X}_{ls})} \qquad \text{Equation 5}$$

$$m_{ls} = \frac{(\mathrm{X}_{hs} - \mathrm{X}_{m})}{(\mathrm{X}_{hs} - \mathrm{X}_{ls})} \qquad \text{Equation 6}$$

$$K_{eq} = \frac{m_{hs}}{m_{ls}} \qquad \text{Equation 7}$$

where *hs* indicates the high spin species and *ls* indicates the low spin species. All X values are calculated (or measured) as a function of temperature. From those magnetic susceptibility values, the temperature dependent magnetic moment (μ_{eff}) could be obtained from Equation 8.

$$\mu_{eff} = 2.828\sqrt{\mathrm{X}_{M}T} \qquad \text{Equation 8}$$

The magnetic moment is used to measure the number of unpaired electrons in a system and is temperature independent.

The equilibrium constants calculated in Equation7 were graphed against temperature in using Equation 9

$$\Delta G = -RT \ln K_{eq} \qquad \text{Equation 9}$$

where ΔG is the Gibbs free energy change between high spin and low spin state in cm^{-1}, R is the gas constant in $cm^{-1}K^{-1}$. Graphing the data as $\ln(K_{eq})$ vs 1/T yields a straight line that can be fit to Equation 10.

$$\ln K_{eq} = -\frac{\Delta H}{RT} + \frac{\Delta S}{R} \qquad \text{Equation 10}$$

where ΔS and ΔH are the thermodynamic properties entropy change and enthalpy change in cm^{-1}, respectively, associated with the high spin to low spin transition. These thermodynamic constants allow for ΔG to be determined as a function of temperature.

Transient Absorption

Transient absorption spectroscopy measures the absorption spectrum of the excited state of a sample. Figure 4 shows the energy level diagram and sample orientation associated with transient absorption experiments.

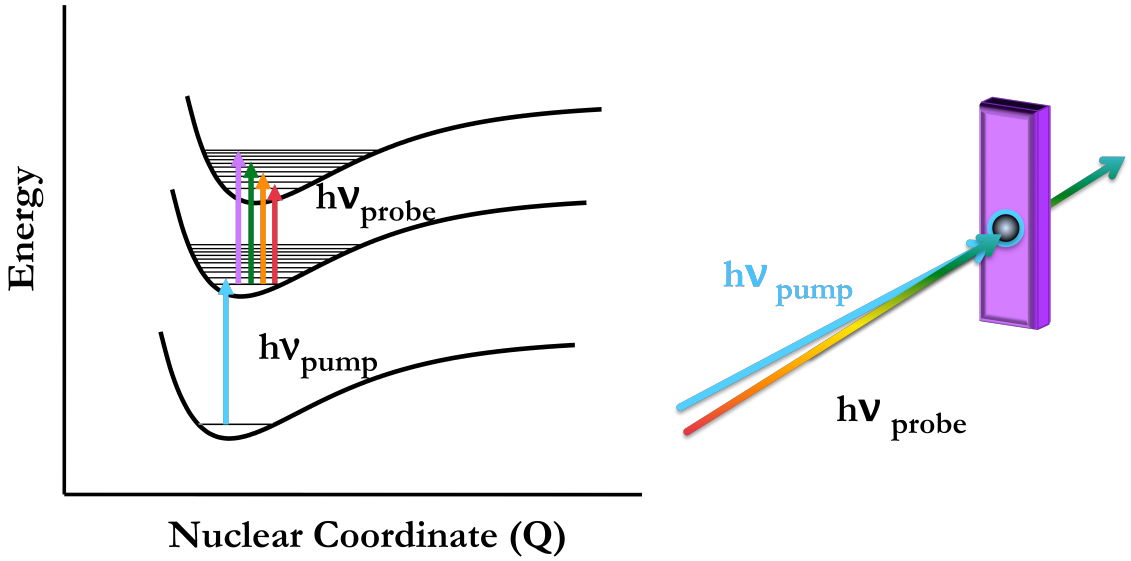

Figure 2-4: (Left Panel) Energy level diagram and (right panel) experimental setup for transient absorption pump/probe experiment. The pump beam (blue) prepares an excited state followed by a probe beam (all other colors) that measures the absorbance difference of that excited state. As seen in the right panel, pump and probe beams come in slightly non-colinear with the pump beam slightly larger than the probe.

The excited state species that is prepared by the pump beam is completely dependent on the wavelength and absorbance features of the molecule of interest. For example, many of the molecules discussed in this dissertation have MLCT transitions as well as ligand-based and ligand field transitions. Absorption spectra associated with each of these species will be unique and will be observed only when those species are present.

Unlike steady state absorption, the exact concentration of the excited state species cannot be known *a priori*. The excited state is prepared by laser light excitation and probed by a secondary beam. A small percentage of the ground state will be excited, leaving a large

background of ground state from which the excited state spectrum must be distinguished. For this reason, the signal is collected as a difference spectrum as given by Equation 3. The ground state absorbance spectrum becomes the background against which the excited state spectrum is compared. This means that the signal can be positive or negative, depending on the relative absorbance of the excited state as compared to the ground state. Figure 4 shows a simulated "ground" and "excited" state along with the difference spectrum associated with the two species.

In regions of the spectrum where the ground state absorbs more than the excited state, the difference spectrum shows a negative signal, which is called a "bleach". The term bleach comes from the fact that more light is getting through the sample in the excited state than in the original ground state. Excited state absorption regions occur where the excited state absorbs more than the ground state, less light traverses the sample, and a positive feature is observed. Absorptive features are more informative than bleach features. A bleach will always occur in a transient absorption experiment because the excitation of molecules automatically leads to a decrease in ground state concentration as the molecules are excited. It is difficult to identify small excited state absorptions on a large ground state bleach, so the magnitude of $\Delta\varepsilon$ is not clear. When a positive feature is detected, however, that always means that the excited state absorbs more than the ground state.

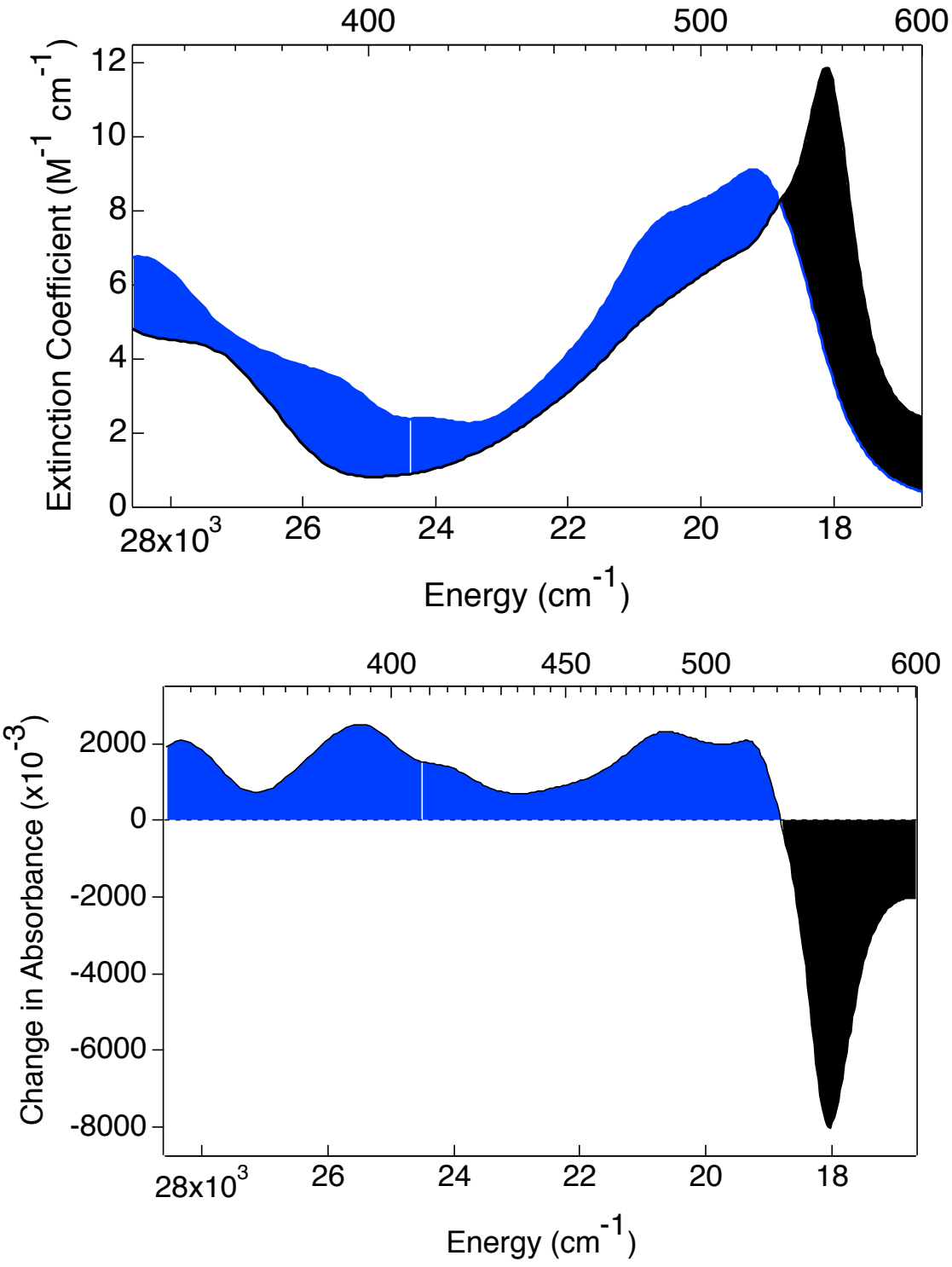

Figure 2-5: (Top panel) Ground (black) and excited (blue) state spectra. (Bottom panel) Difference spectrum for ground and excited state species. Regions where the Figure 5 (cont.): excited state species absorbs more than the ground state shows up as a positive absorption and regions where the ground state absorbs more than the excited state shows up as a negative bleach in the difference spectrum.

The absorption spectrum of the prepared excited state species can be probed for spectral features, kinetics, or a combination. Full spectral traces are collected by probing with a spectrally broad-band beam. In the visible, this manifests as white light which can be coupled into a spectrometer to record the spectrum as a function of time. Single wavelength kinetics are collected more accurately by selecting out one wavelength for detection and monitoring the intensity of that light as a function of stage position (time). The timescale on which this experiment is performed has no impact on the fundamental theoretical aspects discussed. Practical collection setup and techniques, however, will vary with timescale and temperature range over which the experiment is collected.

Variable Temperature Transient Absorption

Variable temperature transient absorption spectroscopy was performed on a nanosecond spectrometer described previously.[2,3] The 355 nm output is coupled into an optical parametric oscillator (OPO) with a repetition rate of 10 Hz. The OPO provides tunable wavelength control from 350-650 with time resolution of ~13 ns. Temperature control was established with a Janis SVT-100 optical dewar described previously.[4] Kinetic traces were collected at each probe wavelength of interest after sufficient time was allowed for temperature stabilization. Exponential decay fits were used to determine the lifetimes of the excited species as a function of temperature. Full spectra were recreated by plotting the initial amplitude as a function of time. Plots of lifetime as a function of temperature were fit to both the Arrhenius equation (Equation 11) and a Marcus form of the non-radiative decay theory equation (Equation 12)

$$k = A\exp(\frac{-E_A}{k_B T}) \qquad \text{Equation 11}$$

$$k = \frac{2\pi}{\hbar}\left|H_{AB}\right|^2 \frac{1}{\sqrt{4\pi\lambda k_B T}} \exp\left(\frac{-(\Delta G + \lambda)^2}{4\lambda k_B T}\right) \qquad \text{Equation 12}$$

where A is the frequency factor (cm^{-1}), E_A is the activation energy (cm^{-1}), k_B is the Boltzmann constant (cm^{-1}/K), T is temperature (K), H_{AB} is the coupling constant (cm^{-1}), λ is the reorganization energy (cm^{-1}), and ΔG is the energy difference between the states of interest (cm^{-1}). Fittings provided values for A, E_A, H_{AB}, λ and ΔG.

Femtosecond Transient Absorption

The combination of the nanosecond laser system along with the 100 fs laser system that had been in the lab for over 10 years provided temporal resolution from about 100 fs – 1 ns and 13 ns - 100s of microseconds. The timescale absent between these two systems had become problematic due to the number of kinetic processes that fell into this window. All of the molecules in the iron(II)-based studies described in this thesis have two time components: one was too fast to resolve on the 100 fs system while the other was too slow for the fs system and too fast for the ns system. As an answer to both of these problems, funding for a new 35 fs laser system was appropriated along with money for a 1035 mm stage. After relocation of the nanosecond system and renovations to the laser lab, both 100 fs system (Wile E) and 35 fs system (Road Runner) are located in one room. The setup for Wile E includes the 1035 mm stage, providing time delays out to 13 ns. Road Runner has the capability to detect time delays as short as 40 fs. The combination of these two systems has effectively closed the "dark window" and pushed our temporal resolution to the point of measuring the shortest time constants we have in these molecules. This section describes both laser setups.

100-fs system "Wile E" (Figure 6):

Wile E has the same setup as the 100 fs system that has been previously reported[2,5] with the addition of a 1035 mm delay stage. Time constants between 10s of picoseconds to nanoseconds can accurately be measured on this newly configured setup. A Verdi V-5 solid state diode-pumped, frequency doubled Nd:YVO_4 laser (532 nm, Coherent) pumps a Mira 900 modelocked Ti:Sapphire Oscillator (803 nm, Coherent). The output of the oscillator (100 fs, 803 nm, 13 nm FWHM, 450 mW @ 76 MHz) seeds the cavity of a Spitfire Ti:Sapphire regenerative amplifier (100 fs, 1 W @ 1 kHz, Positive Light) that is pumped by an Evolution 15 diode-pumped, intra-cavity doubled, Q-switched Nd:YLF laser (527 nm, 1 kHz, Coherent). The output from the Spitfire is split 70:30 to provide the pump and probe beams respectively.

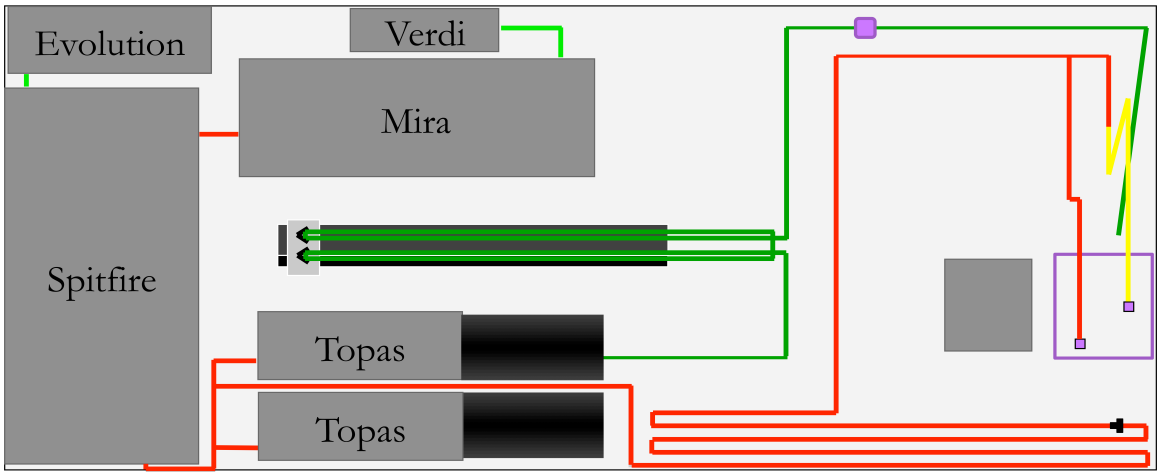

Figure 2-6: Layout of the 100 fs transient absorption spectrometer, "Wile E".

The probe beam is created from 30% of the 800 nm amplifier output. This beam is directed along the table several times to create a constant time delay long enough to maximize the positive time difference between the pump and probe. Polarization of the probe is controlled with a polarizing beam splitter along with a quarter waveplate before

being focused into a self phase modulation medium such as CaF_2 or Sapphire wherein a continuum is produced (320nm-900nm and 430nm-800nm respectively). The white light continuum is focused into the sample with off-axis parabolic mirrors. A small amount of the 800 nm probe beam is split off to serve as the reference beam before the continuum is produced.

Wavelength tunability of the pump beam between 240nm-2600nm is achieved by routing 70% of the Spitfire output into a motorized and computer controlled optical parametric amplifier (TOPAS Standard Model, Light Conversion). This output is sent down a 1035 mm delay line (linear actuator, LMAC series, Aerotech), which provides a dynamic range of 13.3 ns. The pump beam is then focused into the sample at a not-quite-colinear angle (~5-10°) to the probe. Colinear configuration would optimize pump-probe cross-section, but presents two problems. First, the geometric arrangement is physically challenging to accomplish. Second, light from the pump beam would follow the same path as the signal and be focused into the photodiode detector. Separating the signal from the pump is not a trivial process at the small non-colinear angle and directing the pump into the detector would make the task nearly impossible.

Single wavelength traces are collected to determine the timescales associated with kinetic processes initiated by photoexcitation. Selection of a probe wavelength from the continuum is performed using either 10 nm bandpass filters (CVI) or a monochromator (Jarrel Ash). Amplified silicon photodiodes (PDA36A, 350-1100 nm, Thorlabs) measure the light coming from the reference and signal beams. Before excitation occurs, signal into the reference photodiode is attenuated to equal that of the signal photodiode. Differences between the “pump on” (signal detector) and “pump off” (reference detector) are measured

with the help of a lock-in amplifier (Stanford Research Systems). The pump beam is chopped at a frequency slightly below 500 Hz and the signal at the chopper frequency is amplified. This method allows detection of transient difference signals as low as 10^{-4} with as little as one scan (the average of one back-and-forth on the stage). More scans are usually taken—4-16 scans, depending on signal size and laser stability—in order increase signal-to-noise.

Full spectral traces are collected to determine the spectral evolution over the timescale of interest. Kinetic data alone cannot determine the behavior of the complexes - decay or growth of a signal can be due to simple decrease or increase of the population of a species or it can be due to a shift in the spectrum from changing species – requiring the collection of broadband spectra, as well. Time-dependent full spectral traces distinguish between these two situations. Evolution in the intensity and shape of the spectra as a function of time can indicate and even distinguish between a change in population and/or a conversion of the species. Population information comes from the size of the signal whereas information about the species present is indicated by the spectral profile. Full spectra signals can be detected to a change in absorbance level of 10^{-3} with an average of 16-32 scans.

In order to collect full spectral traces, the white light continuum probing the sample is coupled into a liquid light guide to focus the signal into the opening of a spectrometer (SPEX 270M) and horizontally dispersed on a photodiode array (Hammamatsu HC233-0900 with a NMOS C9564 array). The grating angle can be changed with respect to the incoming light in order to select the desired center wavelength. Spectra spanning ~300 nm are collected as a function of pump stage position and movement of the stage builds up the

time-dependent full spectral evolution. Dark counts are collected in the absence of the probe beam at the beginning of each experiment to account for laser scatter. The background is collected at the beginning of each scan at negative time. This "background" spectrum acts as the reference much like the reference photo diode in the single wavelength experiment. It becomes the "zero" from which the change in absorbance is measured against. The small signals along with the noise associated with the white light spectrum requires a larger number of spectra to be collected in order to get a reliable signal.

35 fs system "Road Runner" (Figure 7):

Road Runner is a completely new system purchased for the intended extension of the time resolution to measure short time components. A Mantis modelocked Ti:Sapphire oscillator (Coherent, 80 MHz, 805 nm, > 70 nm FWHM, OPSL pump) seeds a Legend Elite USP Ti:Sapphire regenerative amplifier (Coherent, 800 nm, 30 nm FWHM, 1.4W) that is pumped by an Evolution 15 diode-pumped, intra-cavity doubled, Q-switched Nd:YLF laser (527 nm, 1 kHz, Coherent). The 1.4 W output is split 70:30 to provide for the pump:probe respectively. Wavelength tunability for the pump pulses comes from a computer controlled motorized OPerA Solo (Coherent, 290-2600 nm). OPA output is sent down a delay stage (Aerotech, ATS-100) with a time delay of 1.4 ns. After traversing a chirp compensator (discussed in the following "artifact correction" section), setup of the transient absorption experiment is the same as for Wile E. Similarly; the probe can be created by either white light continuum through sapphire or CaF_2 or with a second OPerA Solo (Coherent, 290-2600 nm). Figure 7 shows the layout of Road Runner.

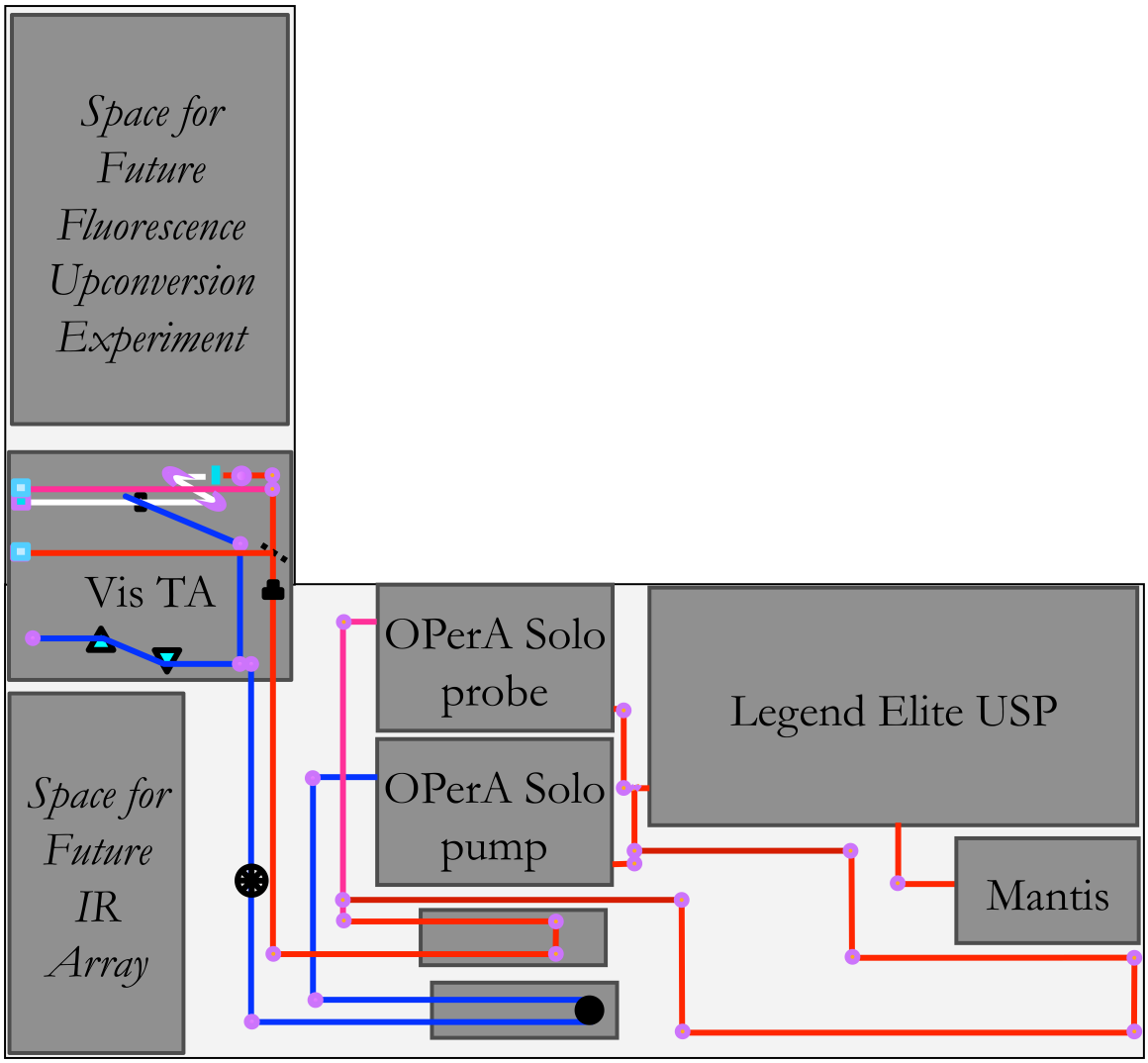

Figure 2-7: Layout for the 35 fs transient absorption spectrometer, "Road Runner".

Single wavelength data is collected with either silicon (350-1100 nm) or InGaAs (PDA-10CS, 800-1800 nm) amplified photodiodes using a similar setup as described for Wile E. When white light continuum provides the probe beam, the silicon visible detectors are used. The IR probe wavelengths necessary for electron injection dynamic detection require the use of the InGaAs photodiodes. Full spectra in both the visible (Ultrafast Systems, Grating 4, 190-800 nm) and near IR (Ultrafast Systems, 800-1700 nm) can also be collected. Labview programs of local origin[6] are used to collect raw data and calculate ΔA

values for both single wavelength and full spectra on both systems.

Artifact Correction:

Moving to the sub-picosecond regime not only precludes the use of fast electronics for data collection, but also introduces a number of possible artifacts that must be accounted for before data collection. Ultrafast transient absorption spectroscopy requires a variety of "checks" to assure data collection pertains to the kinetics associated with the molecular transition of interest, and not artifacts due to group velocity dispersion, polarization effects, changes in pump/probe overlap, and stage alignment; each of which can manifest with the appearance of a misleading kinetic signal.

Group velocity dispersion ("chirp") occurs due to the wavelength dependent index of refraction associated with different media. For example, pulses on Wile E are ~100 fs. According to the Heisenberg Uncertainty Principle for a Gaussian spectral shape, the relationship between the temporal and spectral breadths of the pulse must be $\Delta t \Delta E \geq 0.44$. For a transform limited 100 fs pulse, the spectral bandwidth must be 146.7 cm^{-1}. In the visible, the wavelength range necessary to fulfill this energy spread is small – 400-403 nm, 500-504 nm, 600-606 nm. For the 35 fs pulses of Road Runner, however, 419 cm^{-1} are needed. This is an increase in energy spread to 400-407 nm, 500-511 nm, and 600-616 nm.

The amount of dispersion for any ΔE will be determined by the wavelength distribution along with the intrinsic wavelength dependent index of refraction associated with those wavelengths. Blue wavelengths have more energy per photon than red wavelengths, so a smaller wavelength spread is needed to meet the energy requirements for the short pulses. However, the change in refractive index as a function of wavelength increases with bluer

wavelengths. This means that, although there is a smaller wavelength spread, each blue wavelength experiences more chirp through most optics. As the pulse travels through an optic, the blue photons travel slower, spreading the spectral pulse out temporally. This is illustrated in Figure 8.

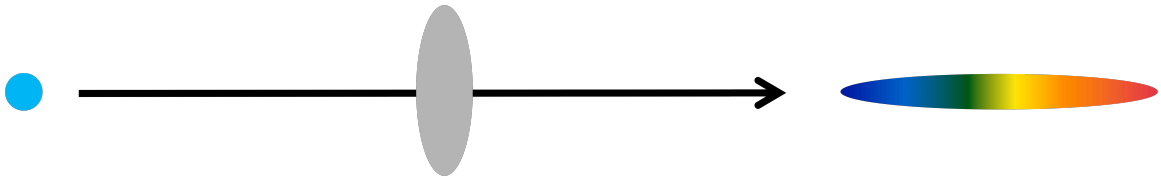

Figure 2-8: A pulse will be spread out in time as it traverses through an optic, due to the wavelength dependent dispersion of the medium as well as the large energy distribution that must accompany short pulses.

The amount of glass traversed (lenses, for the most part) by both pump and probe beams is kept to a minimum on both systems. In both setups, no more than a few hundred femtoseconds worth of chirp is introduced. Because timescales much larger than this are investigated on 100 fs system, chirp correction doe not affect the kinetics measured on the Wile E but must be compensated for on Road Runner.

Chirp correction on Road Runner is performed using a pair of Brewster prisms (Newport, LaKL21) set up in an orientation that allows the blue wavelengths to travel through less glass than the red wavelengths.[7] Since blue wavelengths are slowed down by normal travel through optics, chirp compensation is a way to delay the red wavelengths, resulting in a pulse that is as temporally compressed as possible. The amount of chirp compensation required varies for different pump wavelengths, sample size, and number of optics traversed. This can be accomplished by changing the distance between the prisms.

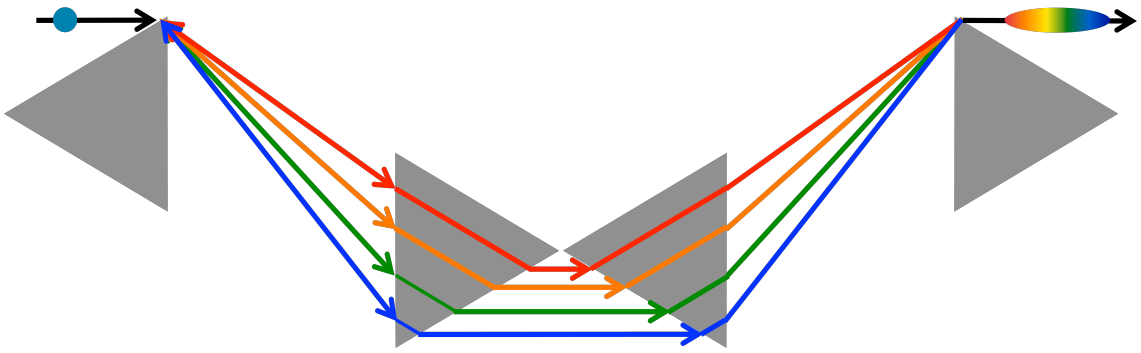

Figure 2-9: Diagram of the chirp compensation setup. Intentionally introducing negative chirp compensates for the positive dispersion that occurs as a function of beam manipulation. The amount of compensation that is introduced can be altered through the distances between prisms and can account for varying amounts of dispersion that occurs in the experiment due to the number of optics traversed, sample thickness, and wavelength. The setup on our table uses only two prisms and a mirror, but 4 prisms are shown for illustrative purposes.

Polarization:

The pump beam exciting the sample is polarized and will only excite molecules that have a dipole oriented along the polarization axis. The polarization of the probe beam will likewise only interrogate excited molecules that have dipole moments along the axis of probe polarization. The excited molecules will rotate in solution as they relax, changing the orientation of their dipole moments. Probe polarizations perpendicular and parallel to the pump can provide information about how quickly the molecules are rotating. Although this is an interesting phenomenon, it only adds complexity to the measurement of interest in these studies. Polarization of the probe is, therefore, set to the "magic angle" of 54.7° from the pump. At this orientation, only population dynamics are measured. The polarization of the probe beam is set by a waveplate and polarizing beam splitter in series. The combination allows for attenuation of the light along with changing the polarization. Since white light is made from focusing the fundamental 800 nm beam into a medium such as CaF_2 or Sapphire, overdriving the substrate results in instability of the light and damage to

the optic. The beam splitting cube determines the polarization of the light that gets through while the waveplate modulates the amount of that polarization that gets through. The rotational diffusion that results in the signal changes from polarization is seen on the order of hundreds of fs[8,9] to ps.[10] Care is taken to measure the difference in pump and probe polarization before each experiment.

Stage Alignment:

The final source of kinetic artifact arises due to the nature of the data collection method. When collecting data on the nanosecond and slower timescales, kinetic information can be gathered in "real time". This means electronics responsible for collecting the data can gather and store population information as the event occurs. Subnanosecond processes, however, occur faster than electronics can respond. This precludes the collection of data in "real time" and requires the build-up of the data and physical manipulation of the distances traveled between beams. Employing the speed of light, differences in the distance the pump and probe beams travel change the time delay between the two. As the distance traveled between the two pulses is varied throughout the experiment, population information is collected as a function of time. "Time zero" is determined to be when both pulses reach the sample at the same time (and therefore are traveling the same distance) with negative time being when the probe reaches the sample first and positive time is when the pump reaches the sample to excite it before the probe comes in to monitor the population.

The intensity of the transient absorption signal comes from a combination of the magnitude of $\Delta\varepsilon$ (goal of the experiment) between the ground state and the excited state of the complex, the sample concentration and pump power density (assumed to be constant over the course of the experiment) which determines the amount of excited state is being

formed, and the pump/probe cross-section in the sample which determines the percentage of the excited state that will be interrogated. The pump/probe cross-section can change as a function of stage position if the beam direction varies with movement of the stage. This will manifest as a change in intensity where no change in excited state absorbance exists. To assure constant pump/probe overlap, "stage scans" are collected by confirming no decay or growth on a standard molecule over the length of the stage. Standard molecules must have no kinetic processes that occur on a timescale of around 10 times the delay available for the stage.

For Road Runner, finding standard molecules is relatively straightforward. The delay available is ~1.4 ns and many molecules absorb visible light and have excited state lifetimes longer than 14 ns. For Wile E, however, the task is a bit more difficult. Molecules of interest must have excited states that last longer than 130 ns to show no decay on the 13 ns delay line. It is also necessary for the standard molecule to absorb the excitation wavelength efficiently enough to create a large enough excited state population to probe without also absorbing all of the probe wavelength photons. This would result in no I_{gr} from which to detect a change in the signal. Equation 13 is another way to frame the ΔA relationship given in Equation 3.

$$\Delta A = -\log(\frac{I_{es}}{I_{gr}}) \qquad \text{Equation 13}$$

Before data collection every day (and as a check throughout the day), a scan is collected on a molecule that is expected to show no kinetic behavior. When a "flat stage" is obtained, it can be assured that changes in population from the sample of interest are due to kinetic processes within the excited state(s) of the molecule. An example of a "flat stage" along

with data collected of a kinetic process is shown in Figure 10. Of course, even with the appropriate standard molecules, travel of the delay line one meter without movement of the beam is extremely difficult.

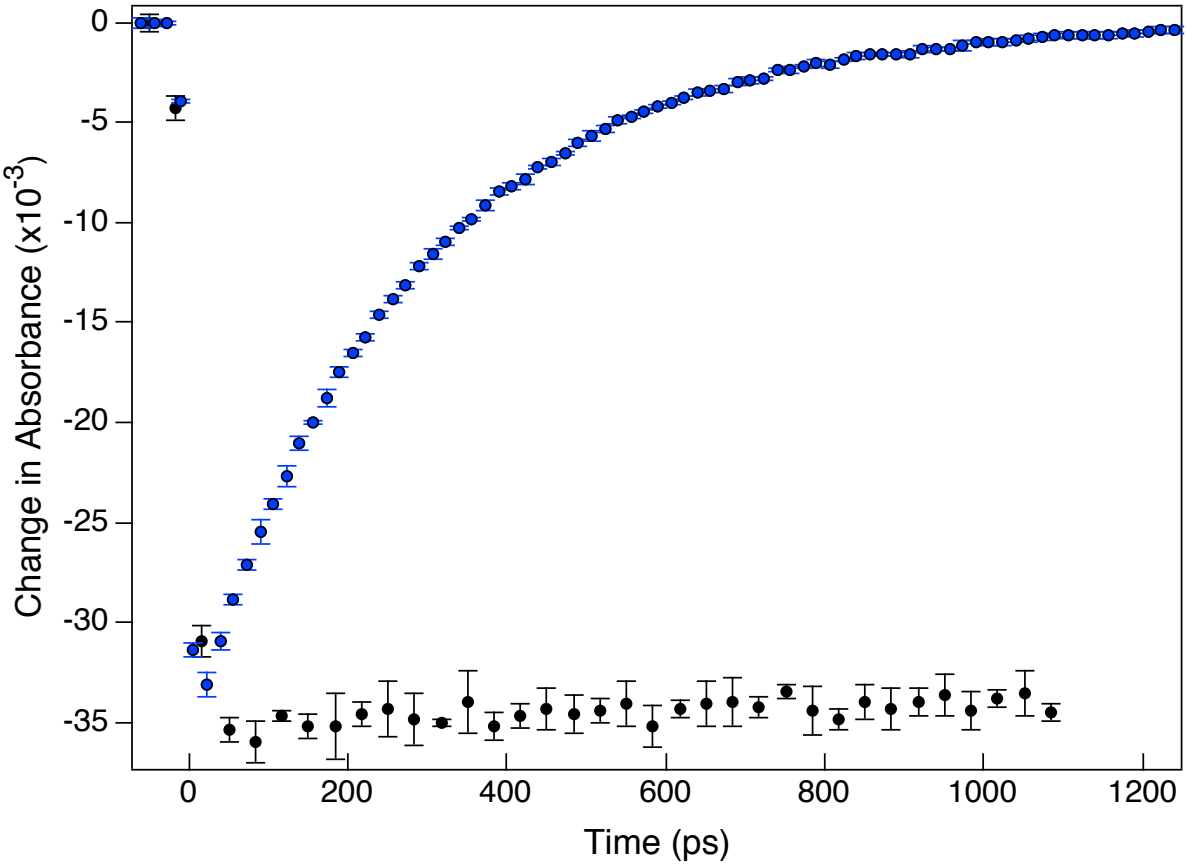

Figure 2-10: Change in absorbance versus time traces for a long-lived standard molecule (black) and a molecule that decays on the timescale of 280 ps (blue). The standard molecule must show no kinetic behavior to ensure the pump/probe overlap is not changing as a function of stage position.

Electron Injection:

With the instrumental setup available in our lab, electron injection can be measured directly or indirectly. Direct detection requires looking at a signal that originates from the presence or build up of electrons in the conduction band. This is in contrast to the indirect measurement that can be detected from the species present before and after electron injection has occurred. These can include the excited sensitizer (before) and the oxidized

sensitizer (after). One problem arising from the indirect detection of the electron is the confluence of signals. Absorptions for the signal of both the excited and oxidized sensitizers appear in the visible. In emission, multiple quenching pathways exist, giving rise to ambiguity about which signal or decay process is due to electron injection.

To eliminate as much of this ambiguity as possible, signals are built upon each other as a progression of signals are identified and measured. Before the transient signal of a complex measured on TiO_2 (into which electron injection is expected to occur) can be interpreted, the intrinsic behavior of the molecule in solution must first be determined. Both kinetic and spectral data are measured to make sure a complete picture is obtained. Once the complex has been measured in solution, the behavior of the molecule on a non-injecting surface must be identified. Any difference between the solution-based signal and the signal measured when attached to a non-injecting substrate must be due to the process of attaching to any surface, not electron injection. A wide band gap semiconductor such as ZrO_2 or Al_2O_3 is used for this purpose.[11] Once the kinetic and spectral signatures for an adsorbed complex are determined, spectra can be collected for the complex on the injecting substrate. In the present case, this is TiO_2, but much work has also been completed on other substrates such as In_2O_3, SnO_2, and ZnO.[11-30]

The new $[Fe(dkpp)_2]^{2+}$ molecule and derivatives thereof have high potential for improved electron injection (and therefore overall efficiency) in DSSCs. The synthesis for addition of the anchoring groups to this molecule is currently in progress by Lindsey Jamula. While waiting for the new sensitizer to be prepared for solar cell investigation, a

protocol for study of these processes must be determined. Although there are many detection methods for the electron injection process, the one currently available is Vis/Near-IR transient absorption spectroscopy. Signals for each of the excited and oxidized form of the complex appear in the visible region, while the conduction band electron absorbs from 700 nm and increases as a power of the wavelength to the red.[31] For each complex studied, a series of full spectra traces will need to be collected in order to identify the origin of each signal. The excited molecule in solution can be characterized by transient absorption spectroscopy and compared to the oxidized molecule by means of spectroelectrochemistry. Any place where both of these species has a negligible signal will be a good place to probe for the conduction band electron.

REFERENCES

References: Chapter 2

(1) Evans, D. F. *Journal of the Chemical Society* **1959**, 2003.

(2) Juban, E. A.; McCusker, J. K. *Journal of the American Chemical Society* **2005**, *127*, 6857.

(3) Smeigh, A. L., Michigan State University, 2007.

(4) Damrauer, N. H.; McCusker, J. K. *Inorganic Chemistry* **1999**, *38*, 4268.

(5) Damrauer, N. H.; Boussie, T. R.; Devenney, M.; McCusker, J. K. *Journal of the American Chemical Society* **1997**, *119*, 8253.

(6) Written by Niels Damrauer, Eric Juban, and Eileen Dixon

(7) Prism Compressor for Ultrashort Laser Pulses, Application Note 29, Newport Coorporations

(8) Damrauer, N. H.; Cerullo, G.; Yeh, A.; Boussie, T. R.; Shank, C. V.; McCusker, J. K. *Science* **1997**, *275*, 54.

(9) Wallin, S.; Davidsson, J.; Modin, J.; Hammarstrom, L. *Journal of Physical Chemistry A* **2005**, *109*, 9378.

(10) Malone, R. A.; Kelley, D. F. *Journal of Chemical Physics* **1991**, *95*, 8970.

(11) Wang, Y. Q.; Asbury, J. B.; Lian, T. Q. *Journal of Physical Chemistry A* **2000**, *104*, 4291.

(12) Xie, Y.; Joshi, P.; Darling, S. B.; Chen, Q. L.; Zhang, T.; Galipeau, D.; Qiao, Q. Q. *Journal of Physical Chemistry C* **2010**, *114*, 17880.

(13) Wang, H. F.; Chen, L. Y.; Su, W. N.; Chung, J. C.; Hwang, B. J. *Journal of Physical Chemistry C* **2010**, *114*, 3185.

(14) Stockwell, D.; Yang, Y.; Huang, J.; Anfuso, C.; Huang, Z. Q.; Lian, T. Q. *Journal of Physical Chemistry C* **2010**, *114*, 6560.

(15) Lu, X. J.; Mou, X. L.; Wu, J. J.; Zhang, D. W.; Zhang, L. L.; Huang, F. Q.; Xu, F. F.; Huang, S. M. *Advanced Functional Materials* **2010**, *20*, 509.

(16) Szarko, J. M.; Neubauer, A.; Bartelt, A.; Socaciu-Siebert, L.; Birkner, F.; Schwarzburg, K.; Hannappel, T.; Eichberger, R. *Journal of Physical Chemistry C* **2008**, *112*, 10542.

(17) Huang, J.; Stockwell, D.; Boulesbaa, A.; Guo, J. C.; Lian, T. Q. *Journal of Physical Chemistry C* **2008**, *112*, 5203.

(18) Guo, J. C.; Stockwell, D.; Ai, X.; She, C. X.; Anderson, N. A.; Lian, T. Q. *Journal of Physical Chemistry B* **2006**, *110*, 5238.

(19) Ai, X.; Anderson, N. A.; Guo, J. C.; Lian, T. Q. *Journal of Physical Chemistry B* **2005**, *109*, 7088.

(20) Lenchenkov, V. A.; She, C. X.; Lian, T. Q. *Journal of Physical Chemistry B* **2004**, *108*, 16194.

(21) Ai, X.; Guo, J. C.; Anderson, N. A.; Lian, T. Q. *Journal of Physical Chemistry B* **2004**, *108*, 12795.

(22) Anderson, N. A.; Ai, X.; Lian, T. Q. *Journal of Physical Chemistry B* **2003**, *107*, 14414.

(23) Anderson, N. A.; Ai, X.; Chen, D. T.; Mohler, D. L.; Lian, T. Q. *Journal of Physical Chemistry B* **2003**, *107*, 14231.

(24) Asbury, J. B.; Wang, Y. Q.; Hao, E. C.; Ghosh, H. N.; Lian, T. Q. *Research on Chemical Intermediates* **2001**, *27*, 393.

(25) Anderson, N. A.; Hang, K.; Asbury, J. B.; Lian, T. Q. *Chemical Physics Letters* **2000**, *329*, 386.

(26) Ellingson, R. J.; Asbury, J. B.; Ferrere, S.; Ghosh, H. N.; Sprague, J. R.; Lian, T.; Nozik, A. J. *Zeitschrift Fur Physikalische Chemie-International Journal of Research in Physical Chemistry & Chemical Physics* **1999**, *212*, 77.

(27) Asbury, J. B.; Wang, Y. Q.; Lian, T. Q. *Journal of Physical Chemistry B* **1999**, *103*, 6643.

(28) Asbury, J. B.; Ellingson, R. J.; Ghosh, H. N.; Ferrere, S.; Nozik, A. J.; Lian, T. Q. *Journal of Physical Chemistry B* **1999**, *103*, 3110.

(29) Ghosh, H. N.; Asbury, J. B.; Lian, T. Q. *Journal of Physical Chemistry B* **1998**, *102*, 6482.

(30) Katoh, R.; Furube, A.; Yoshihara, T.; Hara, K.; Fujihashi, G.; Takano, S.; Murata, S.; Arakawa, H.; Tachiya, M. *Journal of Physical Chemistry B* **2004**, *108*, 4818.

(31) Anderson, N. A.; Lian, T. Q. *Annual Review of Physical Chemistry* **2005**, *56*, 491.

Chapter 3: Determination of Reorganization Energy

Iron(II) complexes were briefly tested as possible alternatives to ruthenium(II)-based sensitizers in dye-sensitized solar cells (DSSCs).[1-3] Although photocurrents were measured from these experiments, the open circuit voltages, short circuit current densities, and overall efficiencies were discouragingly low; very little follow-up or optimization of the cell conditions were attempted. One possible explanation for all of these disappointing values is low electron injection yields – the percentage of injected electrons that result from excited molecules – resulting from rapid relaxation of the initially excited charge transfer state to the low energy ligand field manifold. Improvement of the iron-based sensitizer requires the extension of the charge transfer state lifetime by decreasing the rate at which deactivation to the ligand field manifold occurs. In order to determine the structural and electronic changes that affect the various kinetic processes, it is important and instructive to understand the basic thermodynamic and photophysical characteristics associated with these relaxation processes.

To that end, a series of molecules based on the scaffold of $[Fe(tren(R\text{-}py)_3)]^{2+}$ (Figure 1, where R can be either a methyl group or a proton) have been extensively studied previously and in this work. The benefit provided by this series is the modulation of the energy separation between the ground and lowest energy ligand field excited states, including inversion of these states between complexes 1 and 4.

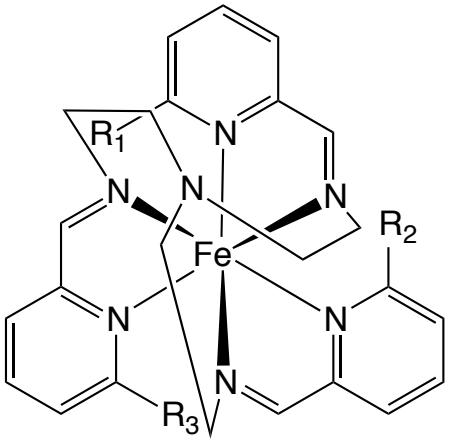

(1) $R_1 = R_2 = R_3 = H$ (low spin)

(2) $R_1 = CH_3$ $R_2 = R_3 = H$ (SCO)

(3) $R_1 = R_2 = CH_3$ $R_3 = H$ (SCO)

(4) $R_1 = R_2 = R_3 = CH_3$ (high spin)

Figure 3-1: $[Fe(tren(6\text{-}Me\text{-}py)_x(py)_{(3-x)})]^{2+}$ complexes with x=0-3. This series spans spin states from low spin (1) to high spin (4) with two thermally accessible spin cross-over complexes (2) and (3).

As seen in the Tanabe-Sugano diagram for d^6 complexes (Figure 2), the $^1A_1$ excited state for high spin Fe^{2+} complexes becomes the ground state when the ligand field becomes large enough to stabilize spin pairing and the low spin complex is favored. The inverse is also true: the $^5T_2$ ground state in the high spin complex becomes the lowest energy excited state at stronger fields. Due to the ability to synthesize and have "in hand" both the high spin and low spin version of this complex, spectroscopic information about the lowest energy excited state of (1) can be obtained by studying the ground state of (4). The pair of complexes has provided information about spectroscopic signatures,[4,5] Fe-N bond lengths,[6] and relaxation timescales[7,8] associated with the $^1A_1$ to $^5T_2$ transition. All of these parameters appear to be consistent with corresponding results for other low-spin Fe^{2+} polypyridyl complexes,[9-20] making the comparisons between complexes 1 and 4 valid for generalization of similar iron(II) complexes.

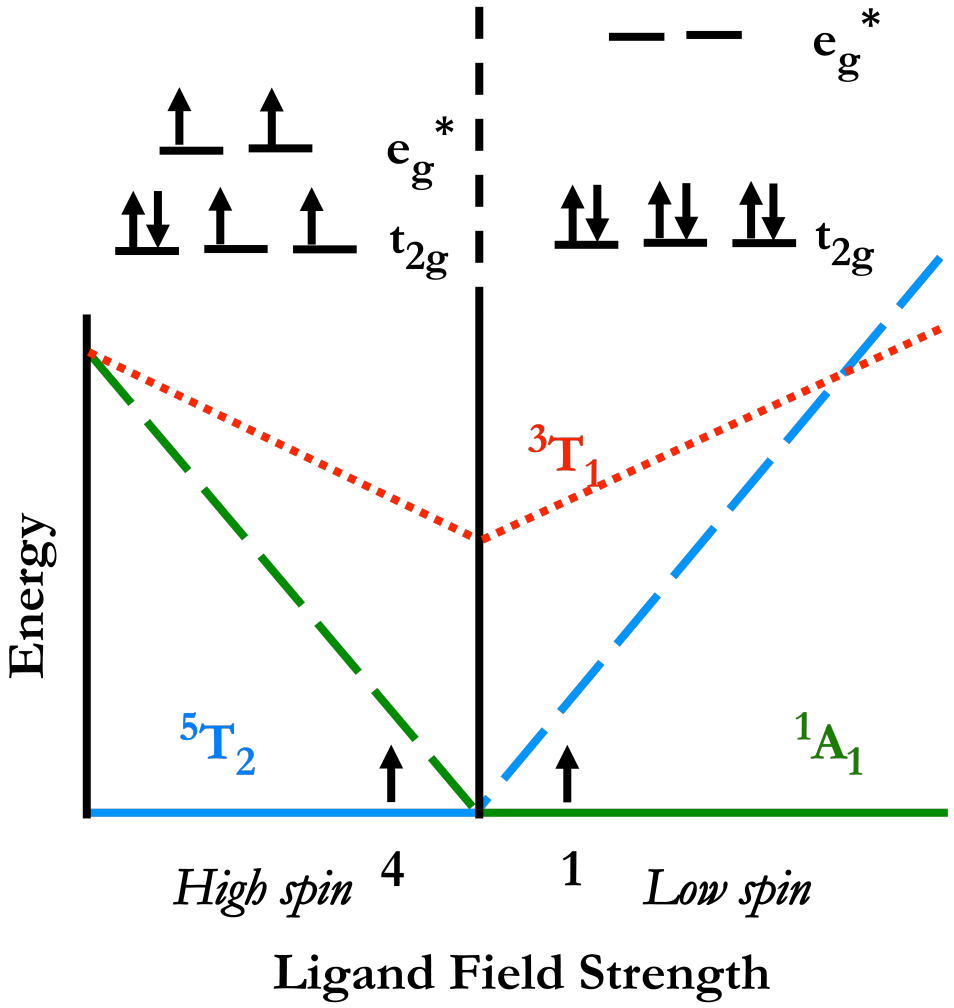

Figure 3-2: The lowest energy ligand field states as calculated in the Tanabe-Sugano diagram for d^6 complexes. At the spin-crossover point, the lowest energy excited state and ground state are inverted. One-electron pictures are shown for the ground states for both the high spin and low spin regions where complex 4 and 1 lie, respectively. The $^3T_1$ state is shown to emphasize its role in providing electronic communication between the singlet and quintet states.

Spectroscopic Identification of Lowest Energy Excited State

As pointed out in chapter 1, attributes of a good sensitizing molecule include the ability to effectively absorb light in the solar spectrum, contain an excited state that is both energetically favorable for electron injection as well as long-lived to optimize efficient injection, and be stable in the oxidized form of the complex between the time of

electron injection and subsequent regeneration. As shown in Figure 2, the $^1A_1$ state places all six electrons in the t_{2g} orbitals while the high spin $^5T_2$ state moves two of those electrons into the e_g^* orbitals. Population of the anti-bonding e_g^* orbitals in the high spin complexes results in significant (10%) elongation of the Fe-N bonds.[6] Longer bonds decrease the electronic overlap between the metal center and the ligands, decreasing the occurrence of MLCT transitions. High spin Fe^{2+} complexes, therefore, lack the large extinction coefficients of charge transfer bands as well as stability in the oxidized form, resulting in more labile complexes. Reversible redox chemistry between Fe^{2+} and Fe^{3+} is more stable in low spin complexes. It is the low spin complexes that are of interest for sensitizers, but the comparison between the high spin and low spin species allows for greater insight into the photophysics associated with the long-lived excited and ground states of the sensitizers.

Low spin iron (II) complexes have both ligand field and metal-to-ligand charge transfer (MLCT) transitions that appear in the visible region of the absorption spectrum. In order to spectroscopically identify a state and measure its lifetime, distinguishing features associated with each of the ligand field and MCLT states must be identified. Once a spectroscopic signature for the transition from one state to the other has been determined, the timescale of that transition can be measured. Because the absorbance spectrum for the excited state of complex 1 is the ground state of complex 4, the absorbance difference can be identified and measured.[21] Using experiments including time resolved X-ray[6,7], raman[8], and absorption[5], the spectroscopic identification of each

state as well as the timescale associated with the transition from one state to the other have been measured. In all of these experiments, it has been determined that the lowest energy excited state is the $^5T_2$ ligand field state and is formed within the first 100 fs after excitation into the ^{1}MLCT band. The mechanism for the rapid $\Delta S=2$ conversion in this and other group 8 polypyridyl complexes has been proposed to follow the sequence $^1A_1 \rightarrow {}^1$MLCT$\rightarrow {}^5T_2$.[18,22-25] Figure 3 shows the plethora of electronic states that lie between the initially excited ^{1}MLCT state and the $^5T_2$ ligand field state and may contribute to the rapid conversion.

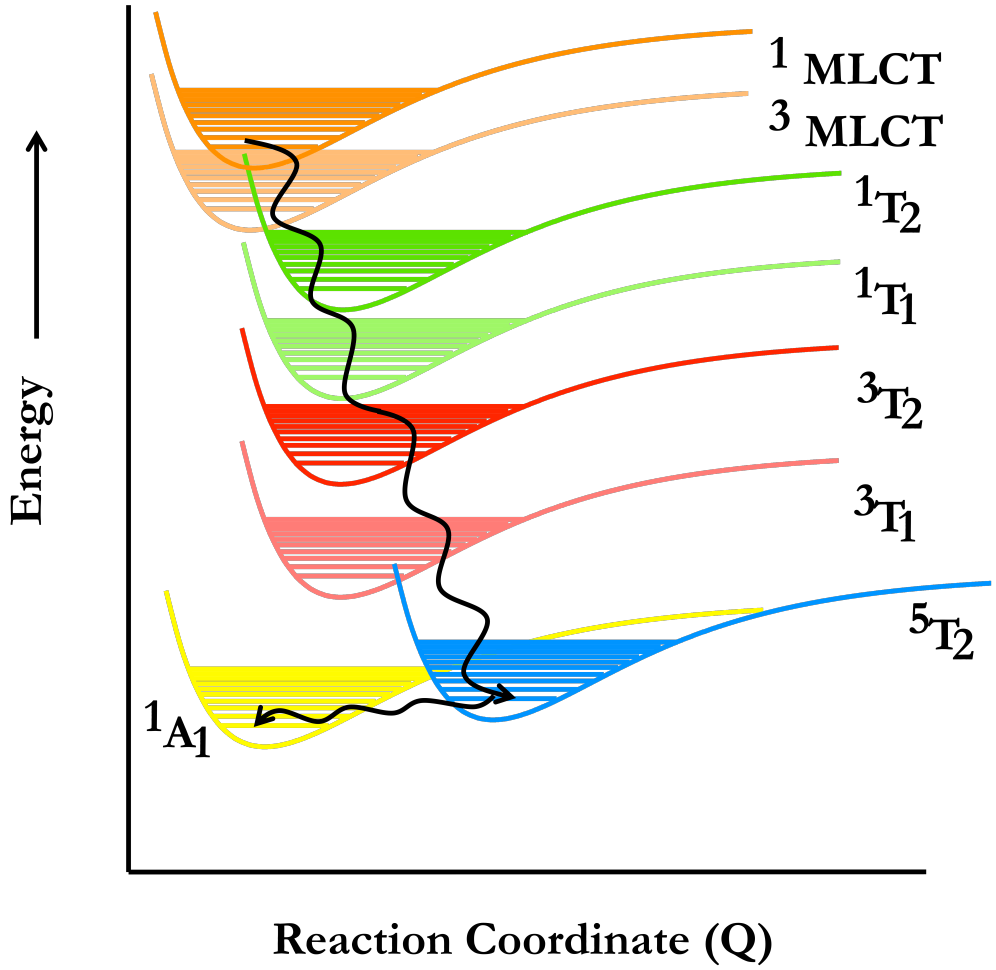

Figure 3-3: Lowest energy charge transfer states along with ligand field states of iron(II) complexes as calculated by Tanabe and Sugano for d^6 complexes. The relative ordering is correct for low spin Fe^{2+} systems, but the diagram is not quantitative.

Kinetic processes associated with the $^1MLCT \rightarrow {}^5T_2$ transition are fast enough that spectroscopic determination of the timescales has only recently been attainable. Before the availability of sub-picosecond time resolution, only the upper limit on the timescale of this transition could be measured. Calculations were used to supplement the kinetic data and provided insight into the mechanism of transition by identifying the states available for mixing.[26,27] Various possibilities for which states mix, are coupled, or are

sampled during this rapid transition from singlet charge transfer state to quintet ligand field state have been proposed. In other Fe(II) complexes, evidence has been seen that the ^{3}MLCT state is sampled during the transition from initial to long-lived excited state.[10] Calculations have also been employed that suggest a large mixing of the $^3T_1$ state to aid ground state recovery.[27] Despite these observations, no state involved in the transition from initial to longest-lived has a long enough lifetime to build up a significant population that might aid in the identification of the states. Repeated verification that the $^5T_2$ state is the long-lived excited state for complex 1 (as well as all other known low-spin iron(II) complexes) and the ground state for complex 4 has provided the necessary framework to verify the notion that spectroscopic information about the excited state of 1 can be gleaned from the ground state of 4. Using a combination of spectroelectrochemistry and transient absorption spectroscopy, a spectroscopic tag was established to determine the timescale of ligand field state formation after charge transfer state population.[4-6]

Using [Fe(tren(6-R-py))$_3$]$^{2+}$ to Determine Thermodynamic Values

Previous work has shown that, upon excitation into the ^{1}MLCT state, population of the $^5T_2$ state in low spin iron(II) complexes is unity.[28] Ground state recovery from the $^5T_2$ state to the $^1A_1$ state was likewise identified and measured for complex 1. Since the entire population of complex 1 in the ground state at room temperature is $^1A_1$ and the

entire excited state population ends up in $^5T_2$, a first order decay kinetic model was used to determine the lifetime of the $^5T_2$ state. In this case, the observed rate is the same as the rate for the $^1A_1 \leftarrow {}^5T_2$ process.

$$^1A_1 \xleftarrow[k_{-1}]{} {}^5T_2 \qquad \text{Equation 1}$$

Variable temperature transient absorption data was collected throughout a temperature range where the $^5T_2$ state was not thermally accessible from the ground state. The rate and temperature data can be fit to the Arrhenius equation (Equation 2):

$$k = A\exp(\frac{-E_A}{k_B T}) \qquad \text{Equation 2}$$

where k is the rate of the relaxation process in s^{-1}, A is the frequency factor in s^{-1}, E_A is the activation barrier in cm^{-1}, k_B is the Boltzmann constant in $cm^{-1}K^{-1}$, and T is temperature in K. Although, historically, this data has been fit to a straight line in the form ln(k) vs 1/T, new graphical and fitting programs make it simple to use the unmodified equation and avoid the error associated with manipulating the data to be linear. As depicted in Figure 4, the activation energy is the energy difference between the reactant ($^5T_2$) zero-point energy and the crossing point of the two potential wells. In the absence of a barrier, the rate would be equivalent to the frequency factor, which is dependent on the reorganization energy as well as the electronic coupling between the two states. This correlation can be determined when comparing the Arrhenius equation to a Marcus form of non-radiative decay theory as shown in Equation 3:

$$k = \frac{2\pi}{\hbar}\left|H_{ab}\right|^2 \frac{1}{\sqrt{4\pi\lambda k_B T}} \exp\left(\frac{-(\Delta G+\lambda)^2}{4\lambda k_B T}\right)$$ Equation 3

where H_{ab} is the coupling constant in cm^{-1}, λ is the reorganization energy in cm^{-1}, and ΔG is the energy difference between the reactant and product in cm^{-1} as shown in Figure 4. Obtaining values for ΔG, λ, and H_{ab} that can be correlated to variations in rate provides insight into the parameters affecting the lifetimes of states. This allows a structure/function correlation to be made, and provides a mechanism by which intelligent modifications of molecules/sensitizers can be attempted.

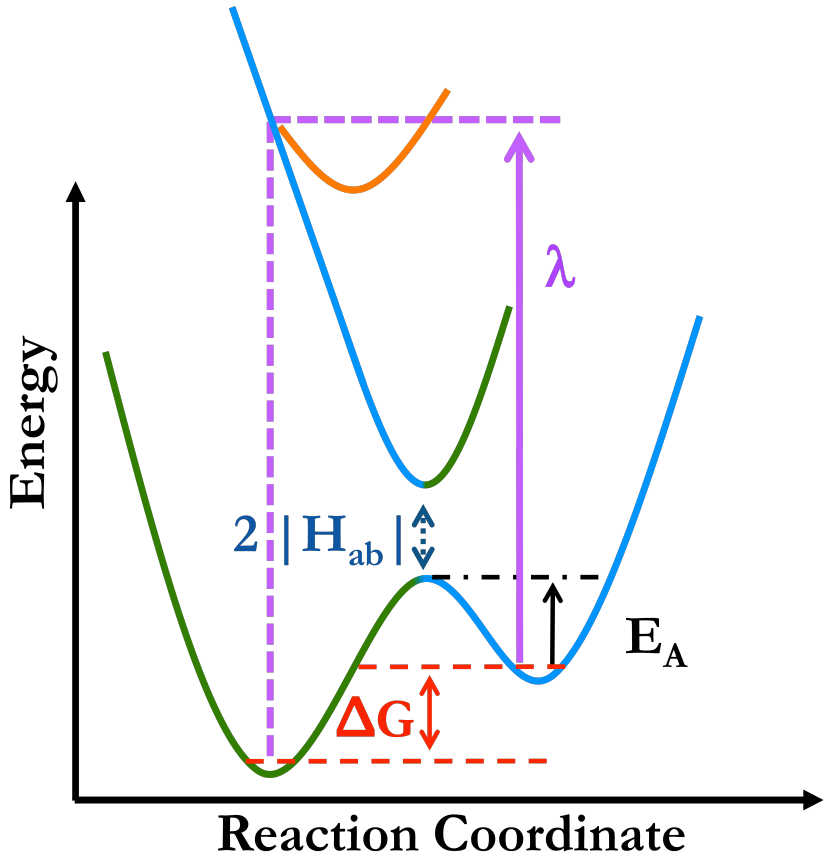

Figure 3-4: Illustrative depiction of the energy separations determining rates of relaxation from the $^5T_2$ excited state to the $^1A_1$ ground state.

The variable temperature transient absorption data shown in Figure 5 provides the values for E_a and A of Complex 1 when fit to Equation 2. At each temperature, a decay trace was collected on the nanosecond transient absorption spectrometer and fit to a single exponential decay

$$I = I0 + A\exp(\frac{-(t - t0)}{\tau}) \qquad \text{Equation 4}$$

where I is the intensity of the signal at time (t), I0 is the intensity offset at negative time, t0 is time zero, A is the initial amplitude of the signal, and τ is lifetime in nanoseconds.

The lifetime (τ) and rate (s^{-1}) are related by Equation 5.

$$k = \frac{1}{\tau} \qquad \text{Equation 5}$$

As stated earlier, because no thermal population of the $^5T_2$ state occurs in complex 1, the observed rate was also the rate of decay for the quintet to singlet process. These data were collected in two different solvents and lead to values for A and E_a within error of each other. Previous measurements of this type have shown solvent and concentration dependences and comparison between literature values and data presented in this thesis suggests a counter-ion dependence of these values.[29] Given the variation for these parameters, comparison between data sets requires a great deal of care to be taken to assure sample conditions are the same.

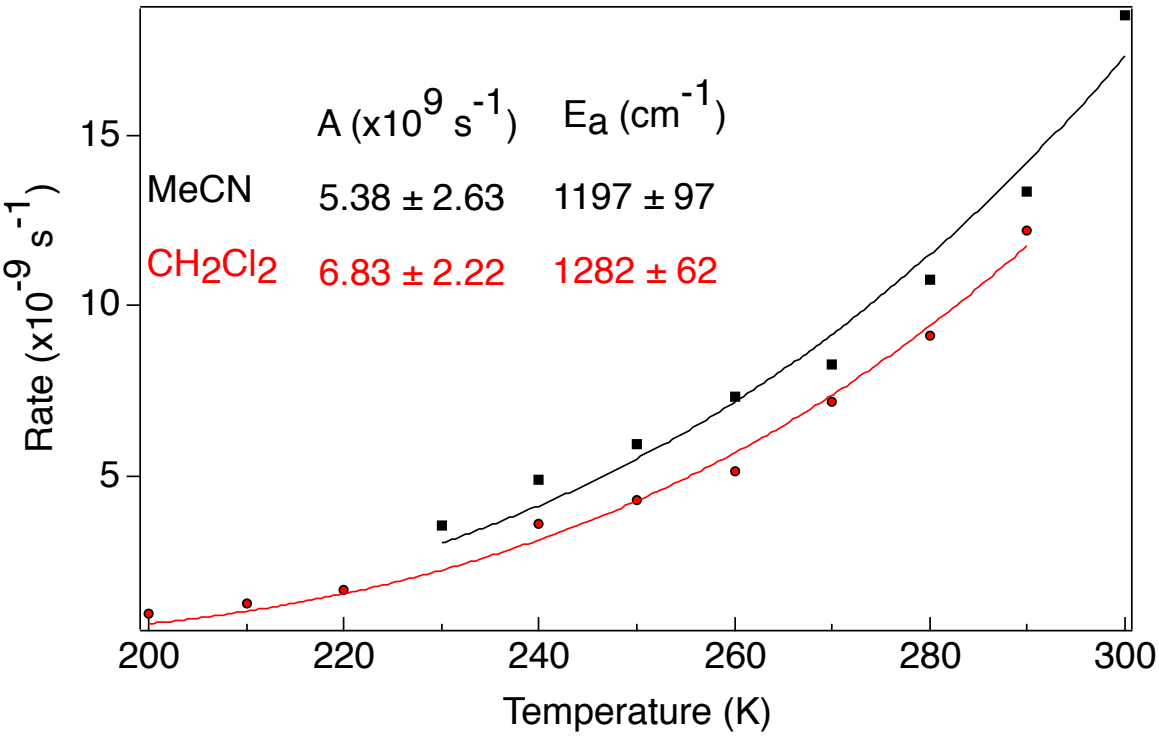

Figure 3-5: Variable temperature kinetic data of $[Fe(tren(py)_3)]^{2+}$ (Complex 1) in acetonitrile and dichloromethane and fit to equation 2.

Fitting the variable temperature data to equation 3 becomes a bit more troublesome, as there are three variables: H_{ab}, λ, and ΔG. Without knowledge of the reasonable range, or better yet, independent determination of one of these variables, many combinations of values can fit the data and no firm conclusions can be drawn from any fits. With the goal of measuring one of these values experimentally and providing the opportunity to fit other two analytically, complexes 2 and 3 were prepared.

Complexes 2 and 3 have the same basic structure as Complex 1, with the addition of one and two methyl groups, respectively, adjacent to the coordinating nitrogen of the pyridine rings. This provides structural changes without adding an electronic component. The steric bulk that accompanies each additional methyl group adds stability to the high spin form of the complex. Both complexes are thermally accessible

spin crossover complexes. This means that over an experimentally accessible temperature range, the fractional populations of low spin $^1A_1$ state and high spin $^5T_2$ states vary. Higher temperatures increase the fractional population of the high spin state which increases the total spin of the system. Equation 5 is the expression for this equilibrium constant.

$$K_{eq} = \frac{\left[{}^5T_2\right]}{\left[{}^1A_1\right]} \qquad \text{Equation 5}$$

The K_{eq} for complex 1 is 0, with no population of the high spin state at any temperature studied. Complexes 2 and 3 have K_{eq} values that vary with temperature. These temperature-dependent K_{eq} values can be determined from magnetic susceptibility data by comparing the temperature to the measured number of unpaired electrons. Magnetic susceptibility provides information about the number of unpaired spins in a system through Equation 6.

$$\mu_{eff}(spin\ only) = g\sqrt{S(S+1)} \qquad \text{Equation 6}$$

where μ_{eff} is the effective magnetic moment of the sample taking into consideration contributions from only the spin of the system, g takes a value of 2 for the spin only approximation, and S is the total spin of the system and is ½ times the number of unpaired electrons. Every molecule in the system is either in the $^1A_1$ state with 0 unpaired electrons or in the $^5T_2$ state with 4 unpaired electrons. From the measured μ_{eff} value, Equation 7 can be used to determine K_{eq}

$$K_{eq} = \frac{x\mu_{eff}^{\left[{}^5T_2\right]}}{y\mu_{eff}^{\left[{}^1A_1\right]}} \qquad \text{Equation 7}$$

where x is the fractional population of the $^5T_2$ state and y is the fractional population of the $^1A_1$ state in the complex.

This can be done in the solid state using SQUID measurements or in the solution phase using Evan's method NMR.[30] Susceptibility data have been previously measured on Complexes 1-4 using both methods[19] and have been remeasured using Evans method in this work. Figure 6 shows the μ_{eff} data obtained in this work for both Complexes 2 and 3.

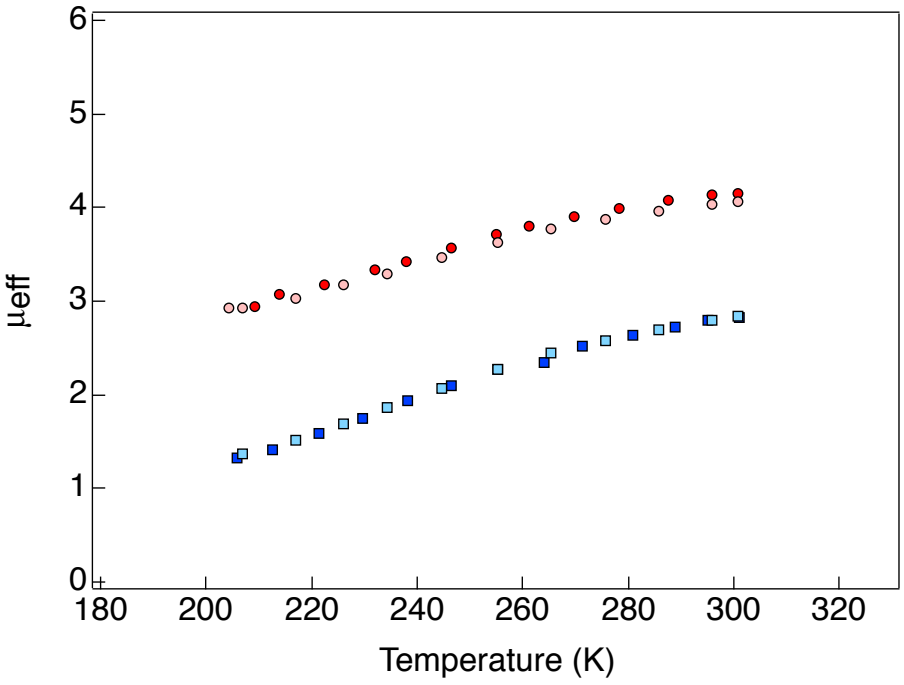

Figure 3-6: Magnetic moment versus temperature data collected from Evan's method NMR for Complexes 2 (red circles) and 3 (blue square). Samples were taken in duplicate

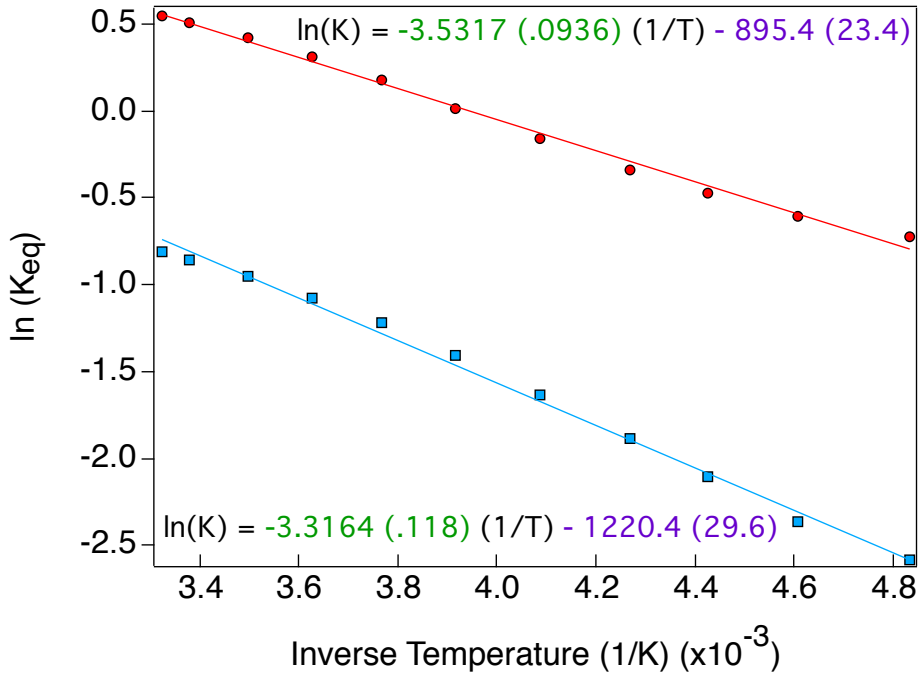

Figure 3-7: Graphical Van't Hoff relationship for Complexes 2 (blue squares) and 3 (red circles). The equations listed provide the thermodynamic values of ΔH (purple) and ΔS (green) along with their errors in parentheses.

The temperature dependent Keq values can then be used to find ΔG, ΔS, and ΔH values using the Van't Hoff relationship

$$\Delta G = -RT \ln K_{eq} \qquad \text{Equation 8}$$

$$\ln K_{eq} = -\frac{\Delta H}{RT} + \frac{\Delta S}{R} \qquad \text{Equation 9}$$

where ΔG, ΔH, and ΔS are the thermodynamic parameters Gibbs free energy, enthalpy change, and entropy change, respectively, for the $^5T_2$ and $^1A_1$ state separation; R is the gas constant in $cm^{-1}mol^{-1}K^{-1}$; T is the temperature in K; and K_{eq} is the equilibrium constant. The fit values are shown on the graph in Figure 7 and can be compared to

literature values.[19] The errors associated with the fits originate from the values used for the high spin and low spin μ_{eff} values from which the X_m values were determined.

Variable temperature nanosecond transient absorption kinetics were collected on complexes 2 and 3 to accompany the thermodynamic values determined by the magnetic data. With the ΔG variable from Equation 3 now determined, the other two can be fit to and values for λ and H_{ab} can be determined exactly. However, the kinetic picture for complexes 2 and 3 is different than for complex 1. Since some of the $^5T_2$ state is thermally populated in the ground state, equation 1 no longer provides a complete description of the kinetics. Instead, two rates must be considered, k_{-1} and k_1.

$$^1A_1 \underset{k_{-1}}{\overset{k_1}{\rightleftharpoons}} {}^5T_2 \qquad \text{Equation 10}$$

$$k_{obs} = k_1 + k_{-1} \qquad \text{Equation 11}$$

$$K_{eq} = \frac{k_1}{k_{-1}} \qquad \text{Equation 12}$$

From the observed rate and the equilibrium constant, the rate of relaxation from the $^5T_2$ state to the $^1A_1$ state can be determined as a function of temperature. Figures 6 and 7 show the temperature/rate relationship for complex 3 in acetone along with the fit to Equation 3 using solution-based thermodynamic parameters of ΔH = -895.4 cm^{-1} and ΔS = -3.532 $cm^{-1}K^{-1}$ for complex 3 and ΔH = -1220.4 cm^{-1} and ΔS = -3.316 $cm^{-1}K^{-1}$ for complex 2.

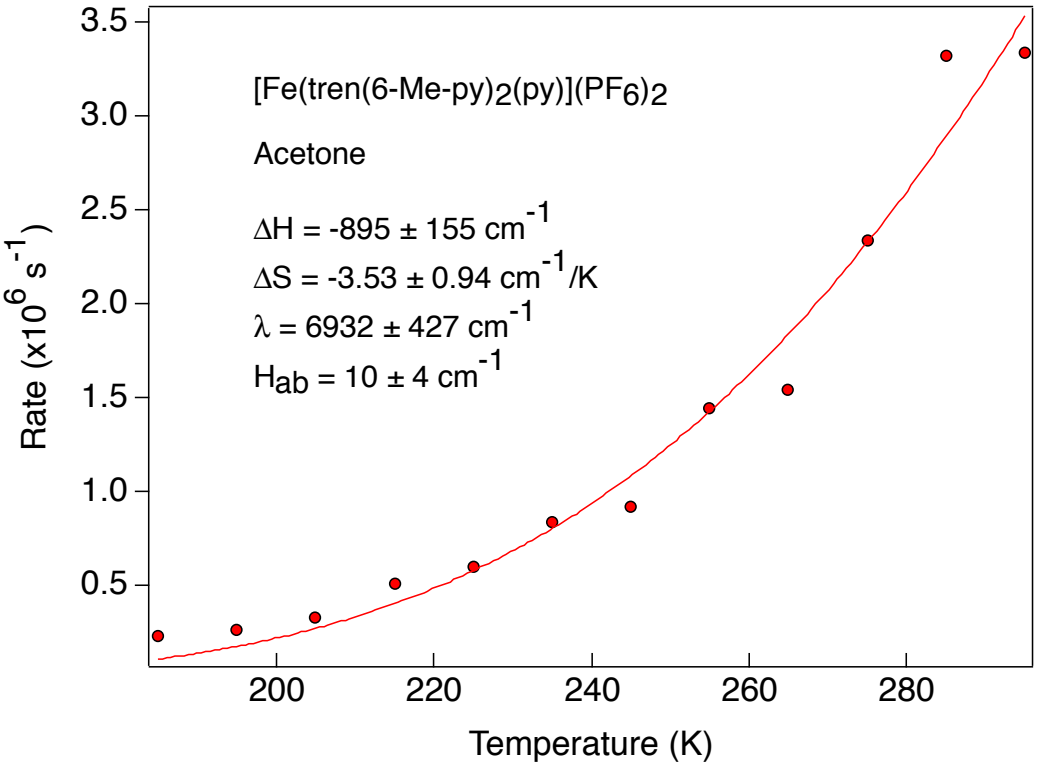

Figure 3-8: Temperature vs rate graph for Complex 3. The solid line is a fit to equation 3 using the solution phase thermodynamic values from this work and the parameters listed in the plot.

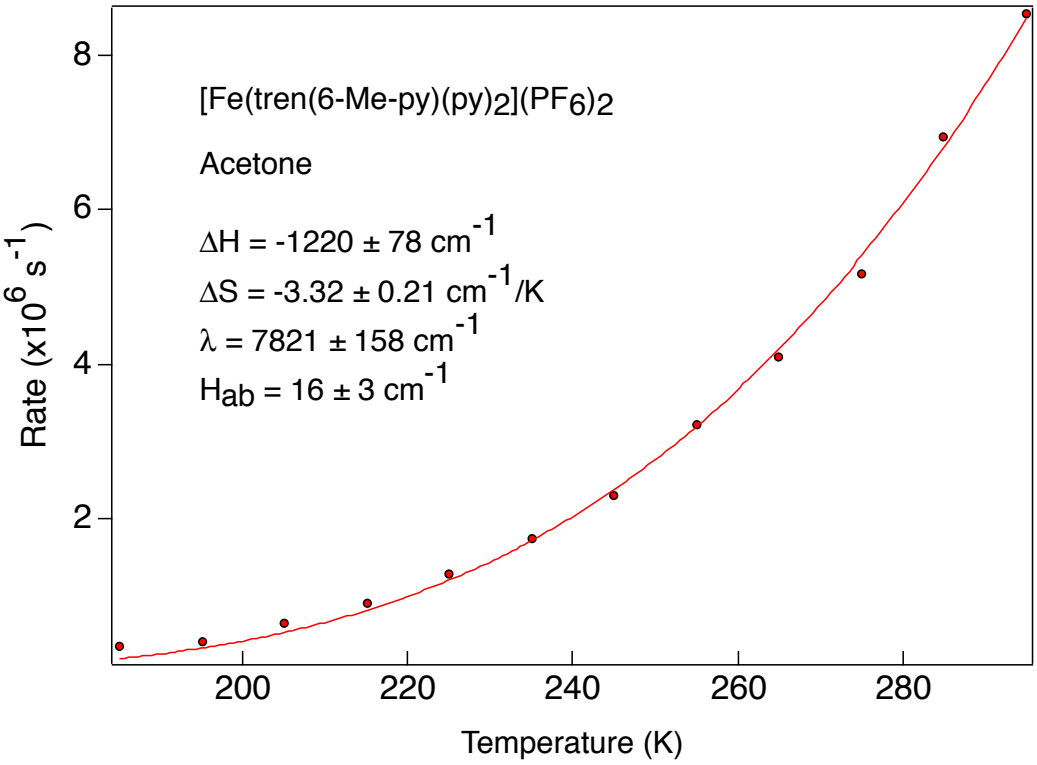

Figure 3-9: Temperature vs rate graph for Complex 2. The solid line is a fit to equation 3 using the solution phase thermodynamic values from this work and the parameters listed in the plot.

The values for reorganization energy and electronic coupling vary with molecule, as is to be expected; however, the differences are small enough to provide a ballpark from which other iron(II) complexes can be predicted or approximated. This provides a range for reasonable fits of complexes for which no parameter can be directly or quantitatively determined. This is the first experimental determination of the parameters for reorganization energy and electronic coupling for iron(II)-based complexes.

Using these ranges as guides, complex 1 was reexamined. No ΔG values has been measured for complex 1, but is estimated to be around 1000 cm^{-1} at room temperature.[29] From this starting point, combinations of ΔH and ΔS values providing ΔG

values ranging between -500 and -1500 cm^{-1} were used to fit the variable temperature data and extract numbers for reorganization energy and the electronic coupling constant. A representative fit is shown in Figure 8, along with the parameters used to fit the data throughout the range of ΔG values.

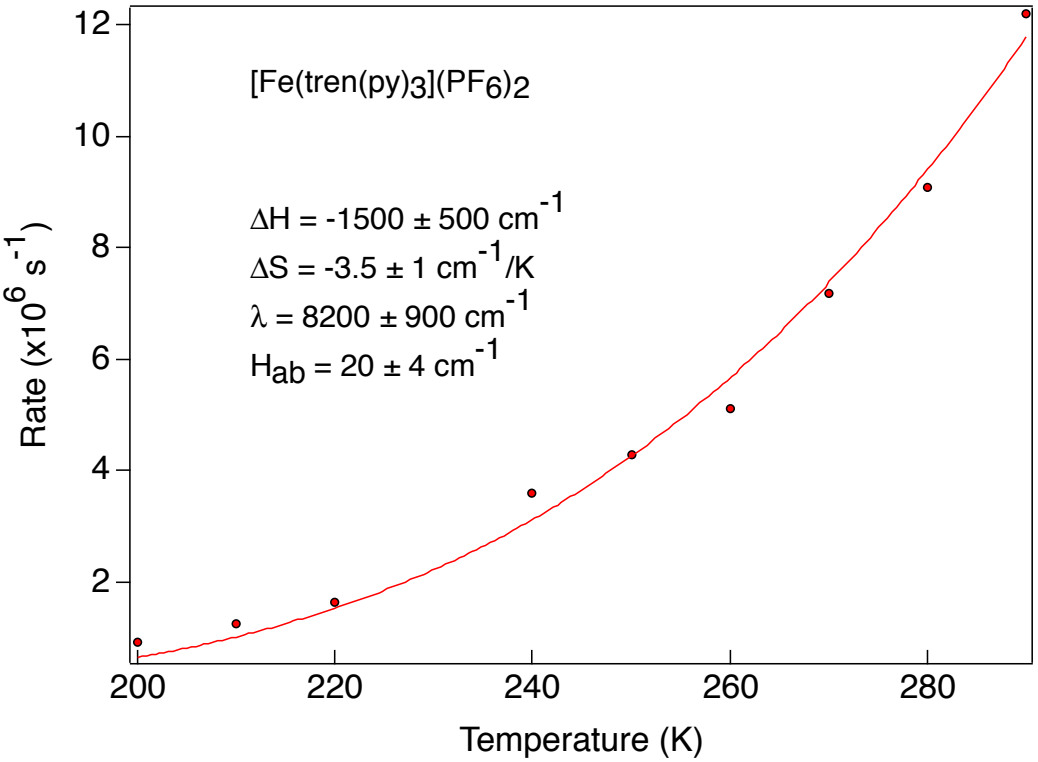

Figure 3-10: Variable temperature kinetic data along with a fit to equation 3 for complex 1. ΔH values ranging between -1000 cm^{-1} and -2000 cm^{-1} and ΔS values ranging between -3 cm^{-1}/K and -4 cm^{-1}/K were used for the fits. Associated values for the reorganization energy and H_{ab} terms are listed in the graph.

As the low spin state becomes more stable (complex 3 → 2 → 1), the difference between the values for reorganization energy and coupling constant get smaller. This predicts that it will asymptotically reach a set of values that are stable and can be used for all low spin complexes with large enough ligand field splitting. Contour plots using ΔH values of -1000 to -2000 cm^{-1} and ΔS values of -3 to -4 cm^{-1} are shown in Figure 11. These plots

show the error associated with fits using the corresponding values of reorganization energy and coupling constant. From these fits, reasonable ranges of 7000-10,000 cm^{-1} for reorganization energy and 20 – 40 cm^{-1} for the coupling constant were determined for complex 1.

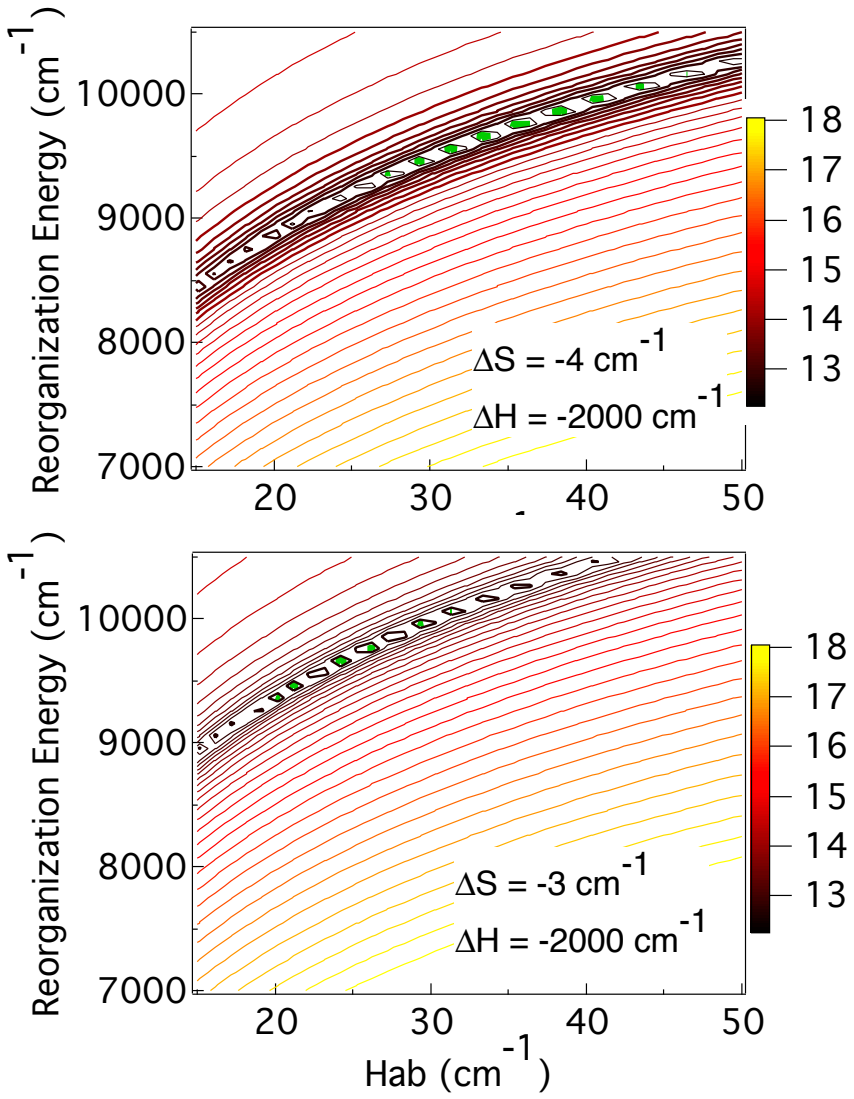

Figure 3-11: Contour plots of complex 1 showing the error associated with fits to equation 3 using various values for ΔS and ΔH. The range of reorganization energies is 7500 – 10,000 cm^{-1} and the range of coupling constant values is 20 – 50 cm^{-1}.

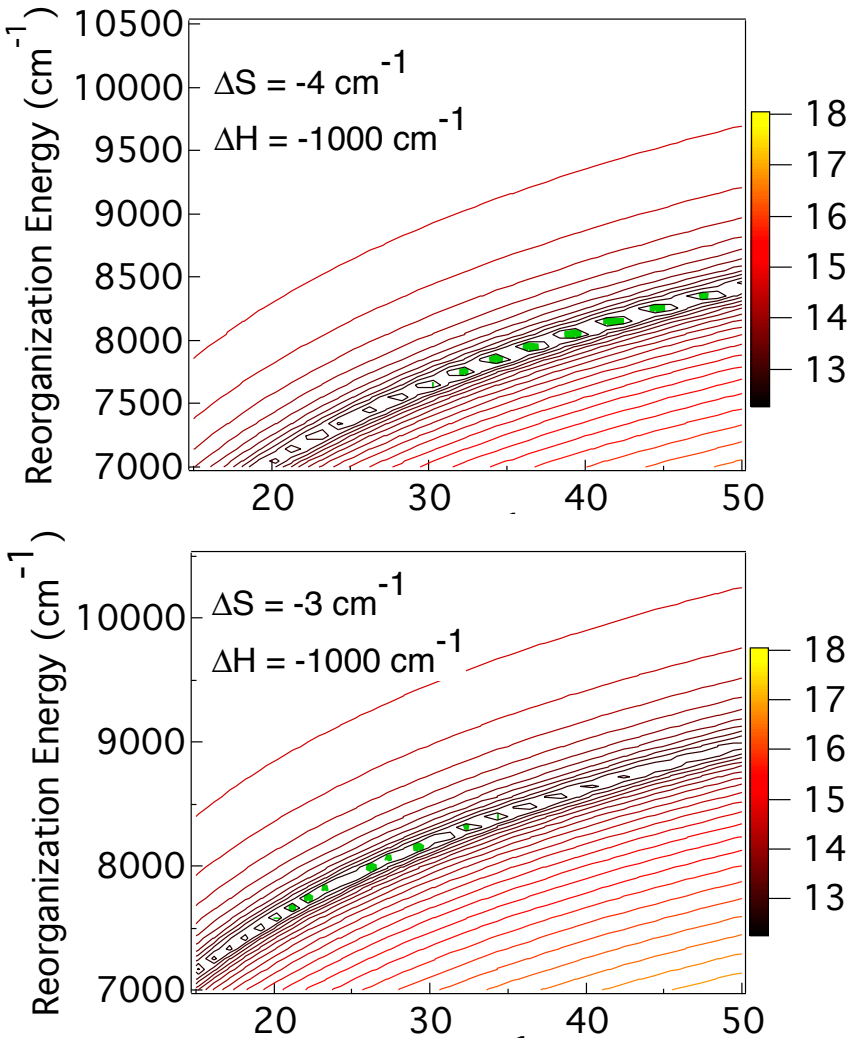

Figure 3-12 (cont.): Contour plots of complex 1 showing the error associated with fits to equation 3 using various values for ΔS and ΔH. The range of reorganization energies is 7500 – 10,000 cm^{-1} and the range of coupling constant values is 20 – 50 cm^{-1}.

These contour plots also illustrate that ΔH has the largest effect on reorganization energy and ΔS affects Hab. This is useful when looking at future molecules. Instead of looking at every possible combination of ΔH and ΔS, the only two values of each (at the

extremes of the ranges) can be used to determine the range of reorganization energies and coupling constants possible for the molecule.

Calculations are currently in progress by Andrew Kouzelos to corroborate these energy values. Energy calculations will be performed on the high spin ($^5T_2$) and low spin ($^1A_1$) geometries for complexes 1-3. The energy separations between the high and low spin states represent the ΔG values at room temperature. Also, the low spin geometry for the high spin state will allow for calculations of the reorganization energy. Agreement between the values from calculations and experiment provides a methodology for determination of these values in future molecules. Validation of the calculations will add a very powerful tool to the arsenal used to determine thermodynamic values in these complexes and present a system for establishing a correlation between structure and rates. In the context of replacing ruthenium-based sensitizers in dye-sensitized solar cells with iron-based dyes, this correlation will be priceless.

REFERENCES

References: Chapter 3

(1) Ferrere, S. *Inorganica Chimica Acta* **2002**, *329*, 79.

(2) Ferrere, S. *Chemistry of Materials* **2000**, *12*, 1083.

(3) Ferrere, S.; Gregg, B. A. *Journal of the American Chemical Society* **1998**, *120*, 843.

(4) Juban, E. A.; Smeigh, A. L.; Monat, J. E.; McCusker, J. K. *Coordination Chemistry Reviews* **2006**, *250*, 1783.

(5) Monat, J. E.; McCusker, J. K. *Journal of the American Chemical Society* **2000**, *122*, 4092.

(6) Khalil, M.; Marcus, M. A.; Smeigh, A. L.; McCusker, J. K.; Chong, H. H. W.; Schoenlein, R. W. *Journal of Physical Chemistry A* **2006**, *110*, 38.

(7) Huse, N.; Cho, H.; Hong, K.; Jamula, L.; de Groot, F. M. F.; Kim, T. K.; McCusker, J. K.; Schoenlein, R. W. *Journal of Physical Chemistry Letters* **2011**, *2*, 880.

(8) Smeigh, A. L.; Creelman, M.; Mathies, R. A.; McCusker, J. K. *Journal of the American Chemical Society* **2008**, *130*, 14105.

(9) Krivokapic, I.; Chakraborty, P.; Bronisz, R.; Enachescu, C.; Hauser, A. *Angewandte Chemie-International Edition* **2010**, *49*, 8509.

(10) Cannizzo, A.; Milne, C. J.; Consani, C.; Gawelda, W.; Bressler, C.; van Mourik, F.; Chergui, M. *Coordination Chemistry Reviews* **2010**, *254*, 2677.

(11) Bressler, C.; Milne, C.; Pham, V. T.; ElNahhas, A.; van der Veen, R. M.; Gawelda, W.; Johnson, S.; Beaud, P.; Grolimund, D.; Kaiser, M.; Borca, C. N.; Ingold, G.; Abela, R.; Chergui, M. *Science* **2009**, *323*, 489.

(12) Halcrow, M. A. *Polyhedron* **2007**, *26*, 3523.

(13) Gawelda, W.; Pham, V. T.; Benfatto, M.; Zaushitsyn, Y.; Kaiser, M.; Grolimund, D.; Johnson, S. L.; Abela, R.; Hauser, A.; Bressler, C.; Chergui, M. *Physical Review Letters* **2007**, *98*.

(14) Gawelda, W.; Cannizzo, A.; Pham, V. T.; van Mourik, F.; Bressler, C.; Chergui, M. *Journal of the American Chemical Society* **2007**, *129*, 8199.

(15) Marchivie, M.; Guionneau, P.; Letard, J. F.; Chasseau, D. *Acta Crystallographica Section B-Structural Science* **2005**, *61*, 25.

(16) Hauser, A. *Spin Crossover in Transition Metal Compounds Ii* **2004**, *234*, 155.

(17) Brady, C.; McGarvey, J. J.; McCusker, J. K.; Toftlund, H.; Hendrickson, D. N. *Spin Crossover in Transition Metal Compounds Iii* **2004**, *235*, 1.

(18) Creutz, C.; Chou, M.; Netzel, T. L.; Okumura, M.; Sutin, N. *Journal of the American Chemical Society* **1980**, *102*, 1309.

(19) Hoselton, M. A.; Drago, R. S.; Wilson, L. J.; Sutin, N. *Journal of the American Chemical Society* **1976**, *98*, 6967.

(20) Hoselton, M. A.; Wilson, L. J.; Drago, R. S. *Journal of the American Chemical Society* **1975**, *97*, 1722.

(21) For a more complete explanation of transient absorption and difference spectra, please see chapter 2.

(22) McCusker, J. K.; Rheingold, A. L.; Hendrickson, D. N. *Inorganic Chemistry* **1996**, *35*, 2100.

(23) McCusker, J. K.; Walda, K. N.; Dunn, R. C.; Simon, J. D.; Magde, D.; Hendrickson, D. N. *Journal of the American Chemical Society* **1993**, *115*, 298.

(24) McCusker, J. K.; Toftlund, H.; Rheingold, A. L.; Hendrickson, D. N. *Journal of the American Chemical Society* **1993**, *115*, 1797.

(25) McCusker, J. K.; Walda, K. N.; Dunn, R. C.; Simon, J. D.; Magde, D.; Hendrickson, D. N. *Journal of the American Chemical Society* **1992**, *114*, 6919.

(26) Buhks, E.; Navon, G.; Bixon, M.; Jortner, J. *Journal of the American Chemical Society* **1980**, *102*, 2918.

(27) Purcell, K. F. *Journal of the American Chemical Society* **1979**, *101*, 5147.

(28) Bergkamp, M. A.; Chang, C. K.; Netzel, T. L. *Journal of Physical Chemistry* **1983**, *87*, 4441.

(29) Conti, A. J.; Xie, C. L.; Hendrickson, D. N. *Journal of the American Chemical Society* **1989**, *111*, 1171.

(30) Evans, D. F. *Journal of the Chemical Society* **1959**, 2003.

Chapter 4: Ground State Recovery and Charge Transfer State Deactivation Correlation

Deactivation of the initially excited charge transfer state of iron(II) complexes is likely a major contributing factor to the loss of efficiency when incorporated into dye-sensitized solar cells. In order to increase the charge transfer state lifetime (which is predicted to increase electron injection yield and overall efficiency), the reaction coordinate responsible for deactivation must be identified in order to be manipulated. As a first step toward identifying and understanding the mode(s) and motion(s) associated with deactivation, a series of $[Fe(R\text{-terpy})_2]^{2+}$ molecules were prepared with increasing steric bulk with respect to the torsional twisting motion as shown in Figure 1. Increasing the size of the substituent adds a physical barrier to rotation, a motion shown to be associated with ground state recovery of iron(II) polypyridyls.[1] It is the correlation between two relaxation processes, charge transfer to ligand field and ligand field to ground state, that will determine whether this reaction coordinate and associated motions affect the charge transfer state lifetime.

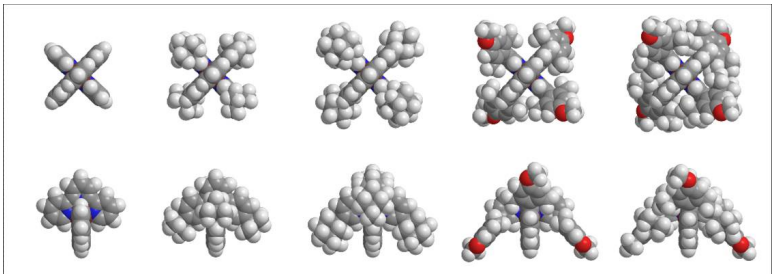

Figure 4-1: Spartan calculations[2] of the series of substituted $[Fe(terpy)_2]^{2+}$ complexes prepared to study the correlation between steric bulk along the torsional twisting motion and charge transfer state deactivation time.

As discussed in chapter 3, the ligand field states involved in ground state recovery for d^6 complexes are $^5T_2$ and $^1A_1$. The $\Delta S=2$ of this transition prevents direct communication between the excited and ground states and should, therefore, be absolutely forbidden. Despite the forbidden nature, the process does, indeed, take place. In 1979, Keith Purcell published a paper discussing the influence ligand field mixing has on the mechanism of intersystem crossing in d^6 complexes.[3] These calculations were initially performed to help explain the fast racemization of $[Fe(bpy)_3]^{2+}$ as compared to the ruthenium(II) and osmium(II) counterparts. His calculations show increased singlet/triplet and triplet/quintet ligand field state coupling associated with a twisting motion along the primary rotation axis. Mixing between the singlet and triplet along with similar coupling between the same triplet and the quintet provides a mechanism for communication between the singlet and quintet.[4] The increased coupling accompanying the twisting motion is believed to assist in ground state recovery of iron(II) complexes.[1,5,6] A metal-ligand bond elongation accompanies the twisting motion to assist in the movement from one enantiomer to the other. Energetic separations between ground and excited ligand field states are larger for second and third row transition metals, resulting in less mixing and preventing the coupling that assists rapid racemization in the first row analog.

Purcell's theoretical findings were experimentally corroborated in the 1990s by McCusker and Hendrickson.[1] Using a series of iron(II) complexes with varying degrees of flexibility around the primary rotation axis, variable temperature transient absorption measurements provided activation energies and frequency factors as a function of steric

hindrance to twisting. Results from this study showed a correlation between the flexibility to twisting and ground state recovery rate. This $^5T_2 \rightarrow {}^1A_1$ process is spin forbidden by a $\Delta S = 2$. Without coupling of the higher energy $^3T_1$ state, the ground state recovery process would take a very long time. Instead, second order coupling allows this transition to occur on the timescale of picoseconds to nanoseconds.

A similar overall $\Delta S = 2$ transition occurs upon photoexcitation of most low spin iron(II) complexes. When excited in the visible, the initially populated excited state for these complexes is a ^{1}MLCT that rapidly decays to a $^5T_2$ ligand field state.[7-10] Whereas ground state recovery occurs between two metal-centered electronic states, ligand-based orbitals are involved in the initial charge transfer state from which the deactivation process of interest occurs. In order to ascertain whether charge transfer state deactivation follows the same reaction coordinate and is dependent on the same motions as ground state recovery, a series of substituted $[Fe(R\text{-terpy})_2]^{2+}$ molecules was designed to monitor both processes.

Substitution of the 5- position of the terpyridine rings with consecutively bulkier groups should lead to a systematic increase in the ground state recovery time. Since it is the twisting motion that improves mixing of the states that assist the relaxation process, physically blocking the molecule's ability to perform the twist should lead to a larger activation barrier and a corresponding decrease in the ground state recovery rate. The analogous prediction cannot be made about the charge transfer state deactivation since no equivalent experiments have been performed for this process. The sub-hundred femtosecond timescale of charge transfer-to-ligand field transitions requires the use of ultrafast spectroscopic methods. This study represents the first attempt to determine the

reaction coordinate—modes and motions—associated with the charge transfer deactivation for iron(II) polypyridyl complexes.

Synthetic: All synthetic procedures and characterization were performed by Lindsey Jamula and are described in her Master's and Ph.D. theses.

Ground State Absorption: Extinction coefficients were collected in acetonitrile for all of the terpy series complexes, as shown in Figure 2. The similar shapes for all complexes in the charge transfer region indicate a minimal change in electronic states as the substituents are changed. This was a very important aspect of the series since the goal was to determine the impact of structural, not electronic, changes on the rates. It is clear that the ligand set has an effect on the absorbance characteristics for the ligand localized transitions.

The aromatic complexes have ligand-based transitions that are shifted to the red compared to the aliphatic substituents. It is important to note that although differentiation can clearly be made between ligand sets in the UV region of the spectra, that same effect is not present in the charge transfer region.

All five molecules were synthesized and characterized by Lindsey Jamula. Absorption spectra for the complexes are shown in Figure 2. The complexes will be discussed according to their substituents, falling into three categories: unsubstituted, aliphatic, and aromatic. Substitutions were made at the 5,5'- positions for two reasons. Steric bulk at the 6,6'- positions have been shown to produce high spin complexes and substitution at the 5,5' positions mitigates electronic coupling into the parent terpy ring. In order to determine whether the same motions govern both transitions, it is important to have complexes that are both low spin and free from electronic contributions. Identification of the reaction

coordinate requires the ability to change one variable at a time. Addition of electronic changes complicates the data and prevents a clean separation of contributions.

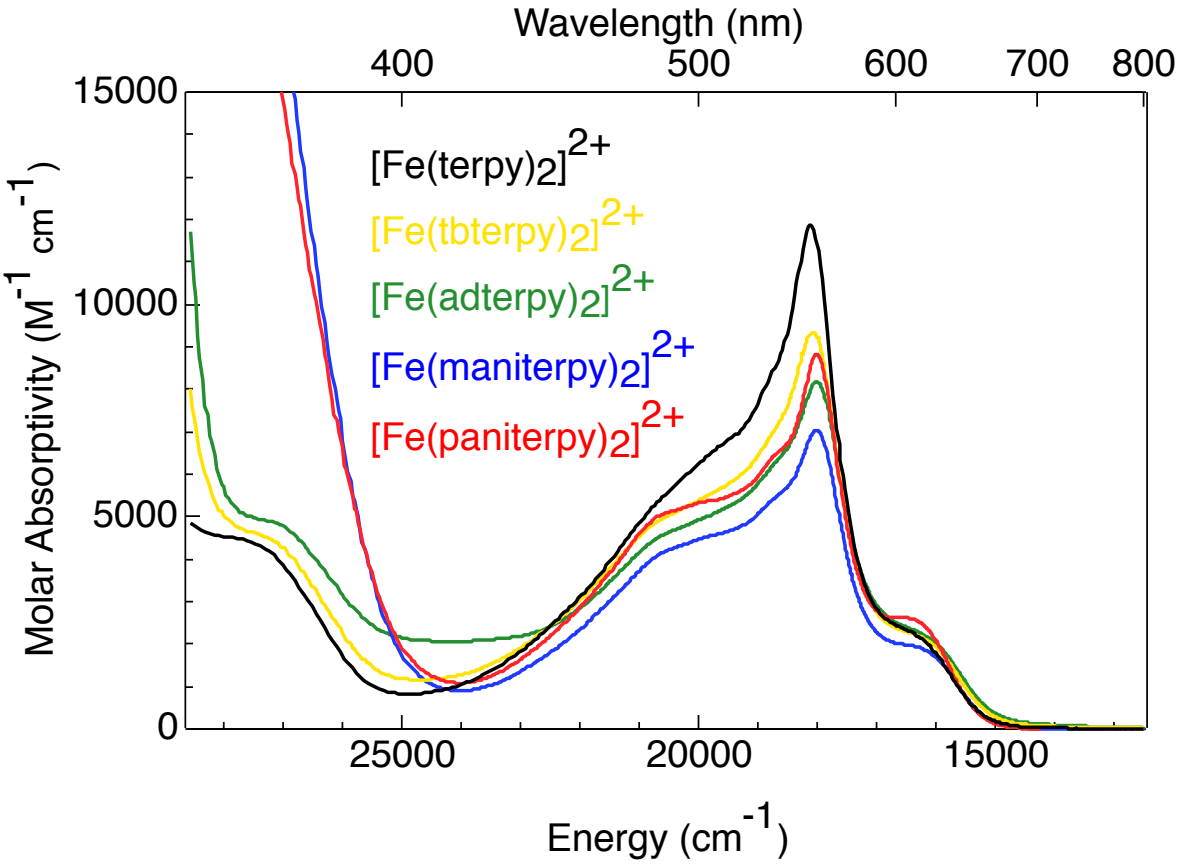

Figure 4-2: Extinction coefficients for the $[Fe(R\text{-terpy})_2]^{2+}$ series in spectrophotochemical grade acetonitrile.

The intense features centered around 540 nm have been assigned as metal-to-ligand charge transfer transitions and the bluer transitions are consistent with ligand-centered absorptions. Although there is some variation in the extinction coefficients for the MLCT transitions, the consistent maximum wavelength and shape give evidence that the charge transfer transitions are not greatly affected by the addition of the different substituents. Differences in the extinction coefficients may be due to a small amount of intensity stealing

between MLCT and ligand-centered transitions. As can be seen in Figure 2, the complexes with lower intensities for the charge transfer absorptions increase in intensity in the blue. The lack of conjugation associated with aliphatic substituents mitigates their electronic contribution to the π system of the terpy. The aromatic substituents raised concerns about coupling to the π system, extending the conjugation of the terpy, and adding electronic contributions in an experiment designed to determine the effect solely of steric bulk. Attempts were made to find bulkier groups than the t-butyl and adamantine substituents, but none could be found. Due to the lack of aliphatic systems with more bulk, it was decided to include the aromatic substituents in the study. Geometry calculations and crystal structure information showed the appended phenyl as orthogonal to the main terpy system.[11,12] Additionally, ground state absorption spectra of the aromatic complexes showed very similar MLCT behavior to the aliphatic complexes. These observations are consistent with a ground state that does not increase electronic contributions with the aromatic substitutions. The ligand-based transitions have shifted with the different ligand substitutions, falling again into the three classes. Substituting with aliphatic groups results in a small red shift of the ligand localized transitions and variation in intensities as compared to the unsubstituted terpy. Aromatic groups decrease the energy of the ligand reduction potential, resulting in a more dramatic red shift in the ligand localized transitions.

Electrochemical data provide complementary results to the ground state absorption spectra. As shown in Table 1, addition of any substituent shifts the first reduction potential more negative compared to the unsubstituted complex. The electron donating effect of the aliphatic groups is somewhat offset by the addition of aromaticity. The reduction potentials

of the aromatic groups move slightly positive of the aliphatic groups. Oxidation potentials follow no obvious trend and seem to be fairly consistent with keeping the oxidation/reduction separation constant within 100 mV.

Table 4-1: Electrochemical potentials of the first oxidation and reduction events for the $[Fe(R\text{-}terpy)_2]^{2+}$ series. All potentials were measured in MeCN with Pt-disk working electrode and tabulated with reference to NHE. All values are accurate to 20 mV.

	First Oxidation Potential (mV)	*First Reduction Potential (mV)*
$[Fe(terpy)_2]^{2+}$	*1356*	*-1035*
$[Fe(tbterpy)_2]^{2+}$	*1348*	*-1039*
$[Fe(adterpy)_2]^{2+}$	*1321*	*-1081*
$[Fe(maniterpy)_2]^{2+}$	*1391*	*-931*
$[Fe(paniterpy)_2]^{2+}$	*1532*	*-890*

Ground State Recovery: Ground state recovery kinetic traces of the terpy series are shown in Figure 3. The unsubstituted terpy has a lifetime of 2.54 ± 0.13 ns in water as measured 1980 by Sutin and Creutz.[7] Changing the solvent to acetonitrile resulted in a lifetime of 5.21 ± 0.07 ns for the unsubstituted complex.[13] Aliphatic substituents have the expected effect of increasing ground state recovery time as seen in Figure 3 and Table 2. The aromatic substituents, although providing more steric bulk, show an increase in ground state recovery rate. This result is unexpected from the trend observed in previous studies, indicating the influence of another factor. The deviation from the expected results requires a closer look at temperature dependent rates of the complexes.

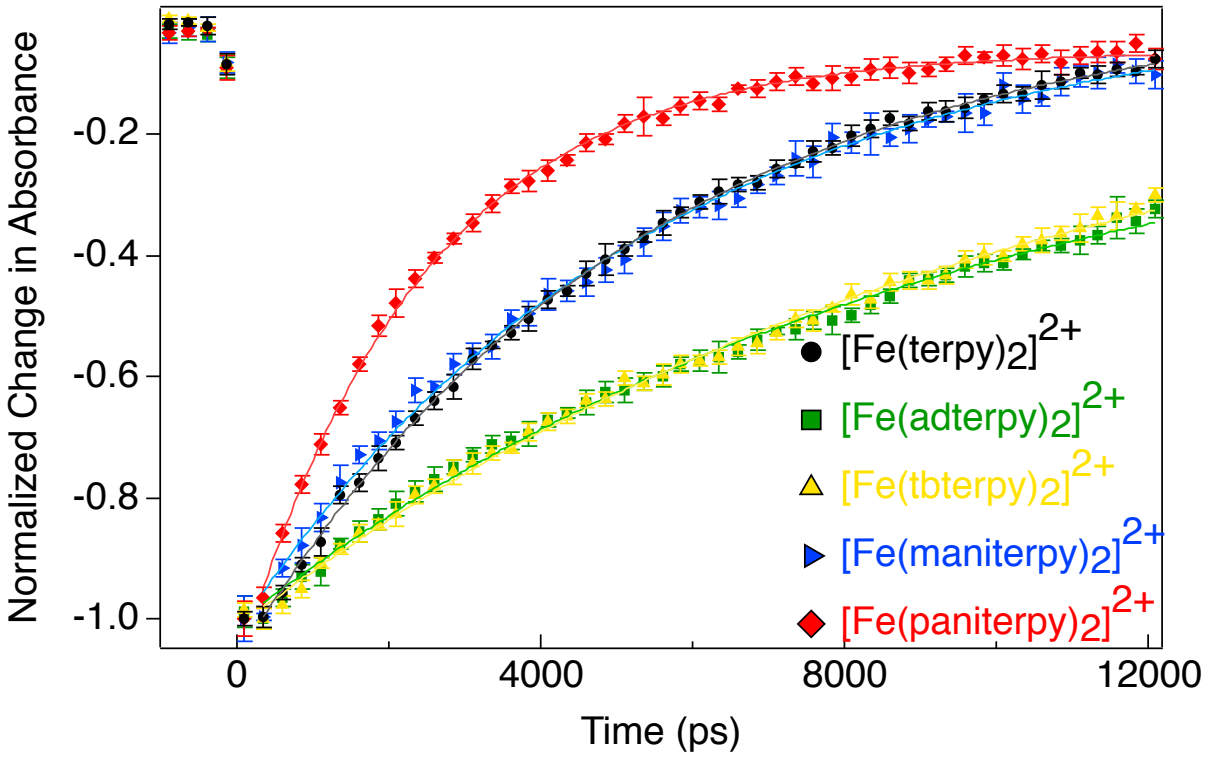

Figure 4-3: Ground state recovery single wavelength traces for the [Fe(R-terpy)$_2$]$^{2+}$series. Data were collected in MeCN at room temperature.

Table 4-2: Ground state recovery lifetime data for the [Fe(R-terpy)$_2$]$^{2+}$series.

	Lifetime in MeCN (ns)
[Fe(terpy)$_2$]$^{2+}$	5.21 ± 0.07
[Fe(tbterpy)$_2$]$^{2+}$	10.05 ± 0.56
[Fe(adterpy)$_2$]$^{2+}$	9.07 ± 0.53
[Fe(maniterpy)$_2$]$^{2+}$	5.43 ± 0.18
[Fe(paniterpy)$_2$]$^{2+}$	2.40 ± 0.03

The Arrhenius equation (Equation 1) was used to fit the temperature dependent data shown in Figure 4. From the fits, values for the activation energy as well as the frequency factor can be extracted. The first comparison to make is between the substituted complexes and the unsubstituted parent complex. Addition of any substituent, aromatic or aliphatic, introduces an increase in the activation barrier. This is expected, as the twisting movement will be hindered by any extra steric bulk in the twisting path. A correlation between the amount of steric bulk added by each substituent and the extent to which the relaxation rate decreased was also anticipated, but no such trend appeared. Instead, it can only be concluded from this series that addition of the extra bulk increased the activation barrier—no trend in activation barrier can be determined when comparing the substituents within the series.

$$k = A\exp(\frac{-E_A}{k_B T}) \qquad \text{Equation 1}$$

Although the increase in lifetime for the aliphatic substituents can be explained by the increase in activation energy, the more rapid ground state recovery of the aromatic substituted systems also show increased activation energies. Were the rates of relaxation dependent solely on the steric bulk of the systems, an increase in the activation barrier would always result in a longer-lived excited state. Instead, it seems as though the sterics of the system are not the only, nor the biggest, factor in determining the rate of ground state recovery.

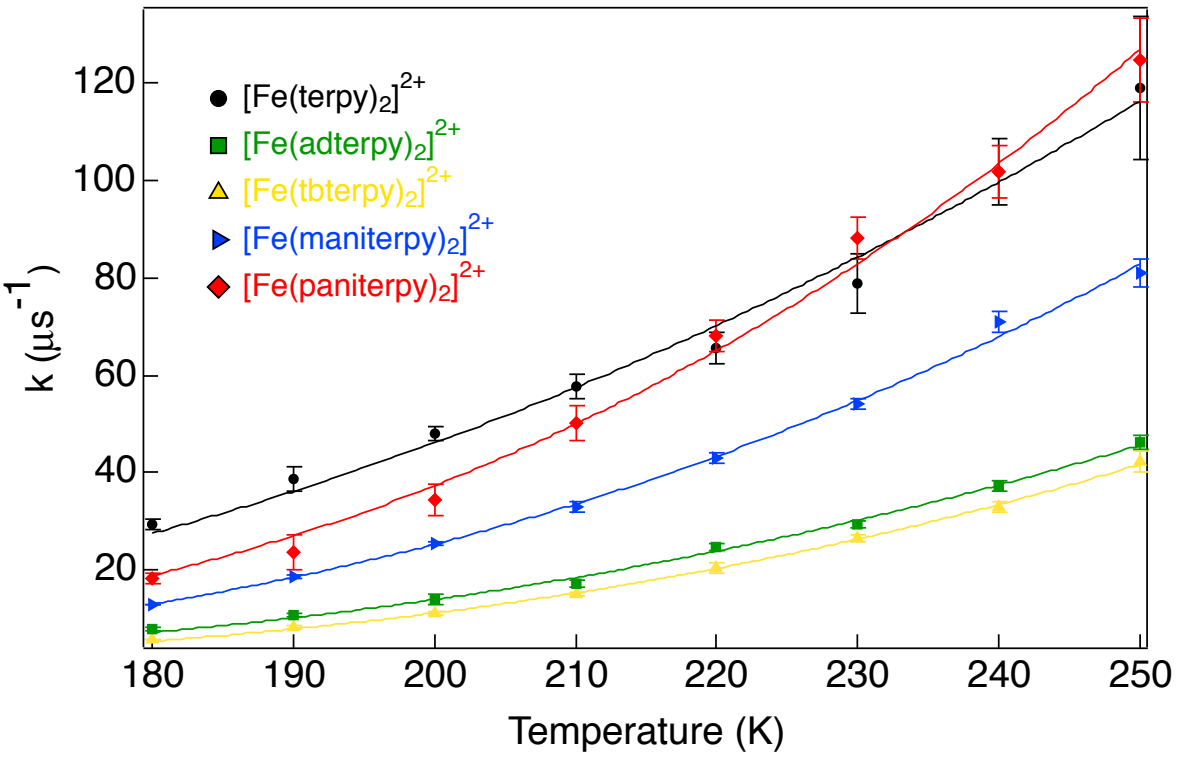

Figure 4-4: Variable temperature lifetime data for the $[Fe(R\text{-}terpy)_2]^{2+}$ series in methanol. Solid lines correspond to fits using equation 1.

In addition to the expected change in activation barrier, a trend in frequency factor along the series was also observed. As seen in Figure 4, an increase in the frequency factor follows the increase in overall steric bulk, although large error is associated with this value. One clear outlier is the aromatic pani substituent—the bulkiest substituent in the series with the fastest rate of ground state recovery. This complex exhibited a surprising result opposite of what was expected by relaxing the fastest instead of the relaxation rate being retarded the most due to steric bulk. Since the expected result was for this complex to show the most retardation of the relaxation rate, it is interesting that it relaxed the fastest instead. The activation barrier differences do not explain this observation, but there is a clear separation in frequency factors. The values for the frequency factor follow a trend associated with increasing steric bulk; however, the errors associated with the values

preclude making definite correlations between steric bulk and the frequency factor—except for the pani substituent.

The frequency factor provides information about the rate of the relaxation if there were no activation barrier for the process. This description provides a way to picture the effect of the variable, but provides little information on how to moderate the value. In order to find a parameter that can be modulated to change the frequency factor, a comparison was made between the Arrhenius equation and the Marcus equation for electron transfer (Equation 2).

$$k = \frac{2\pi}{\hbar}\left|H_{AB}\right|^2 \frac{1}{\sqrt{4\pi\lambda k_B T}} \exp\left(\frac{-(\Delta G + \lambda)^2}{4\lambda k_B T}\right) \qquad \text{Equation 2}$$

Both equations can be readily separated into pre-exponential terms and exponential terms. From the exponential, the activation energy can be related to a combination of the energy gap (ΔG) and the reorganization energy (λ). The pre-exponential terms in the Marcus equation include many constants along with the reorganization energy (λ) and the coupling constant (H_{ab}). The contribution to the pre-exponential term from the reorganization energy is $\lambda^{-1/2}$ while the contribution from the coupling constant is H_{ab}^2. Since the coupling constant contributes only to the pre-exponential factor while the reorganization energy is present in both terms, the variation in frequency factor along with a constant activation energy provides evidence that the coupling term in the series is responsible for the variation in frequency factors.

In conjunction with the results of the measurements discussed in chapter 3 to determine λ of two low spin Fe^{2+} complexes, calculations to determine the magnitude of the coupling

constant along with the variation along the series have been performed. Although the free energy differences for the $^5T_2$ and $^1A_1$ states for these complexes are not known, a range of 1000 cm^{-1} – 5000 cm^{-1} at room temperature should bracket the values. These values are based on the knowledge that the $[Fe(terpy)_2]^{2+}$ $^1A_1/^5T_2$ energy gap is smaller than $[Fe(bpy)_3]^{2+}$ and is larger than $[Fe(tren(py)_3)]^{2+}$. For these calculations, the rate vs. temperature graph was fit to the Marcus equation with the thermodynamic values held constant while the reorganization energy and H_{ab} terms were allowed to float. This was done over a range of ΔH and ΔS values. Figures 5, 6, and 7 show the results of the errors of the fits for the various thermodynamic values used. The fits with the smallest error for each contour graph indicate the best fit. With the range of thermodynamic values used, reasonable ranges for reorganization energy and electronic coupling can be determined. Additional information obtained by calculations could be helpful in narrowing down the range of thermodynamic values used in this process.

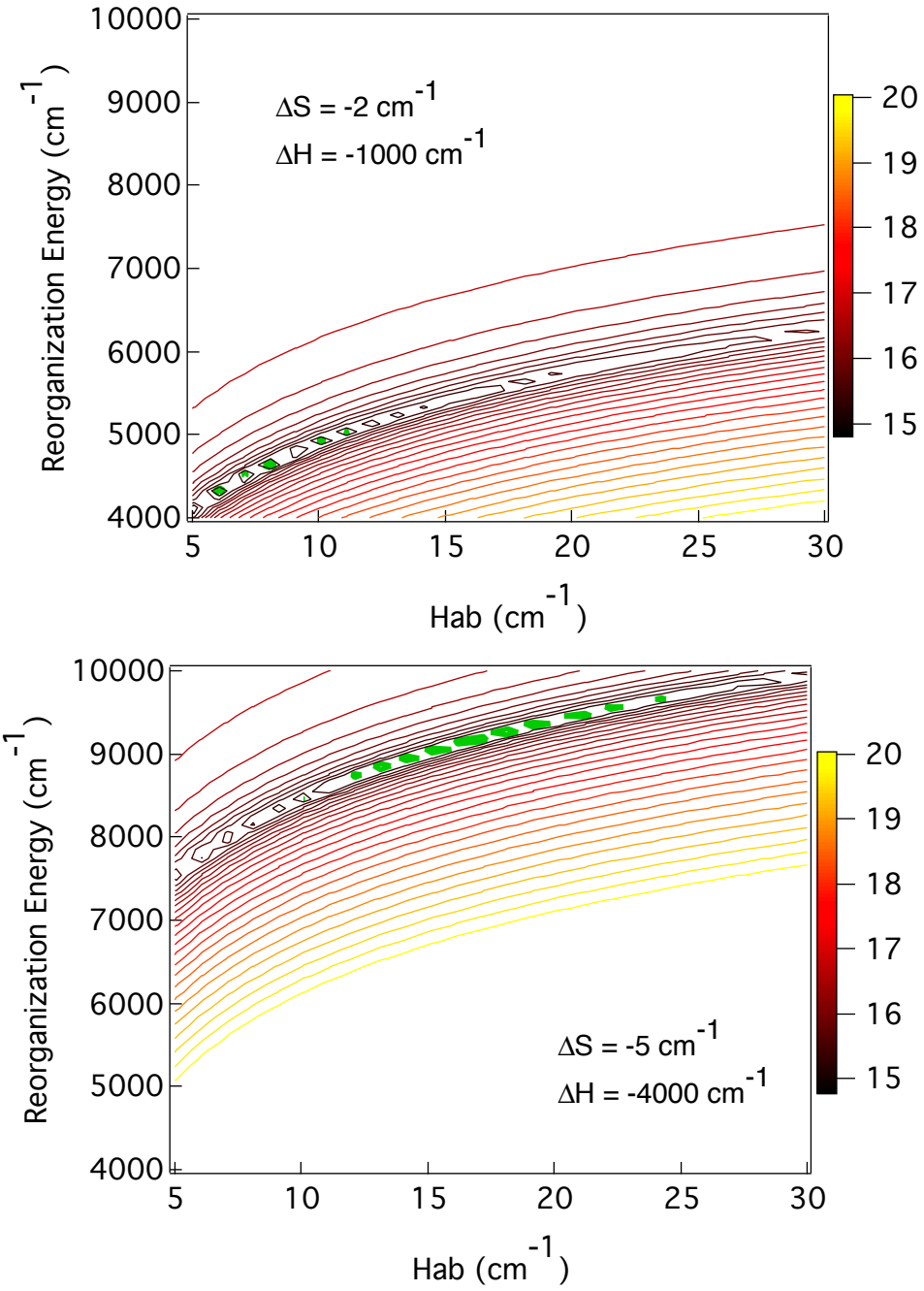

Figure 4-5: Contour plots of $[Fe(terpy)_2]^{2+}$ showing the error associated with the fits using the range of Hab and λ values shown. Smaller values represent better fits, with green indicating the smallest error fits. With the ΔS and ΔH values used for the fits, a range of coupling constants (5 – 25 cm^{-1}) and reorganization energies (4000 – 9500 cm^{-1}) were calculated.

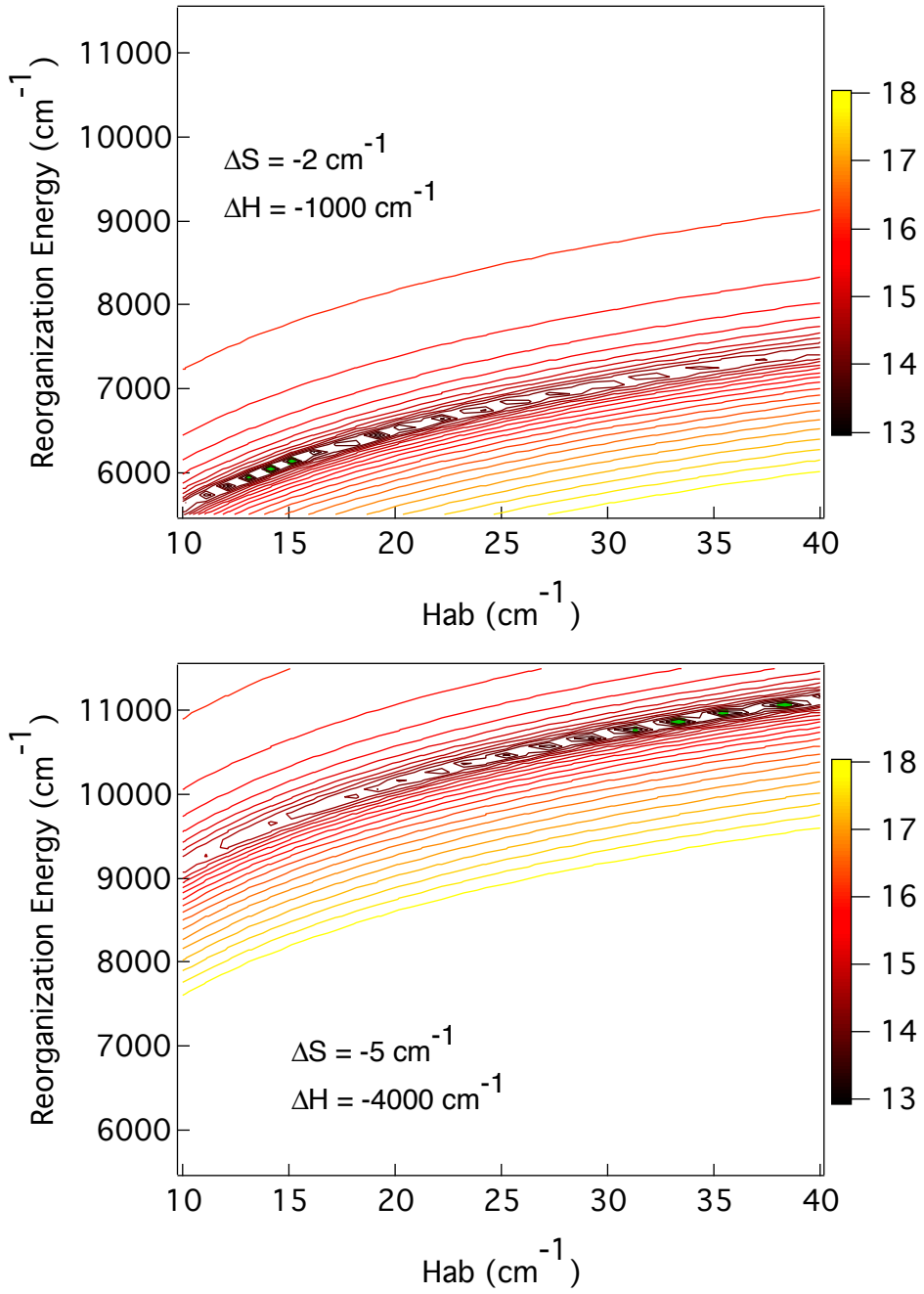

Figure 4-6: Contour plots of $[Fe(tbterpy)_2]^{2+}$ showing the error associated with the fits using the range of Hab and λ values shown. Smaller values represent better fits, with green indicating the smallest error fits. With the ΔS and ΔH values used for the fits, a range of coupling constants (13 – 40 cm^{-1}) and reorganization energies (6000 – 11,000 cm^{-1}) were calculated.

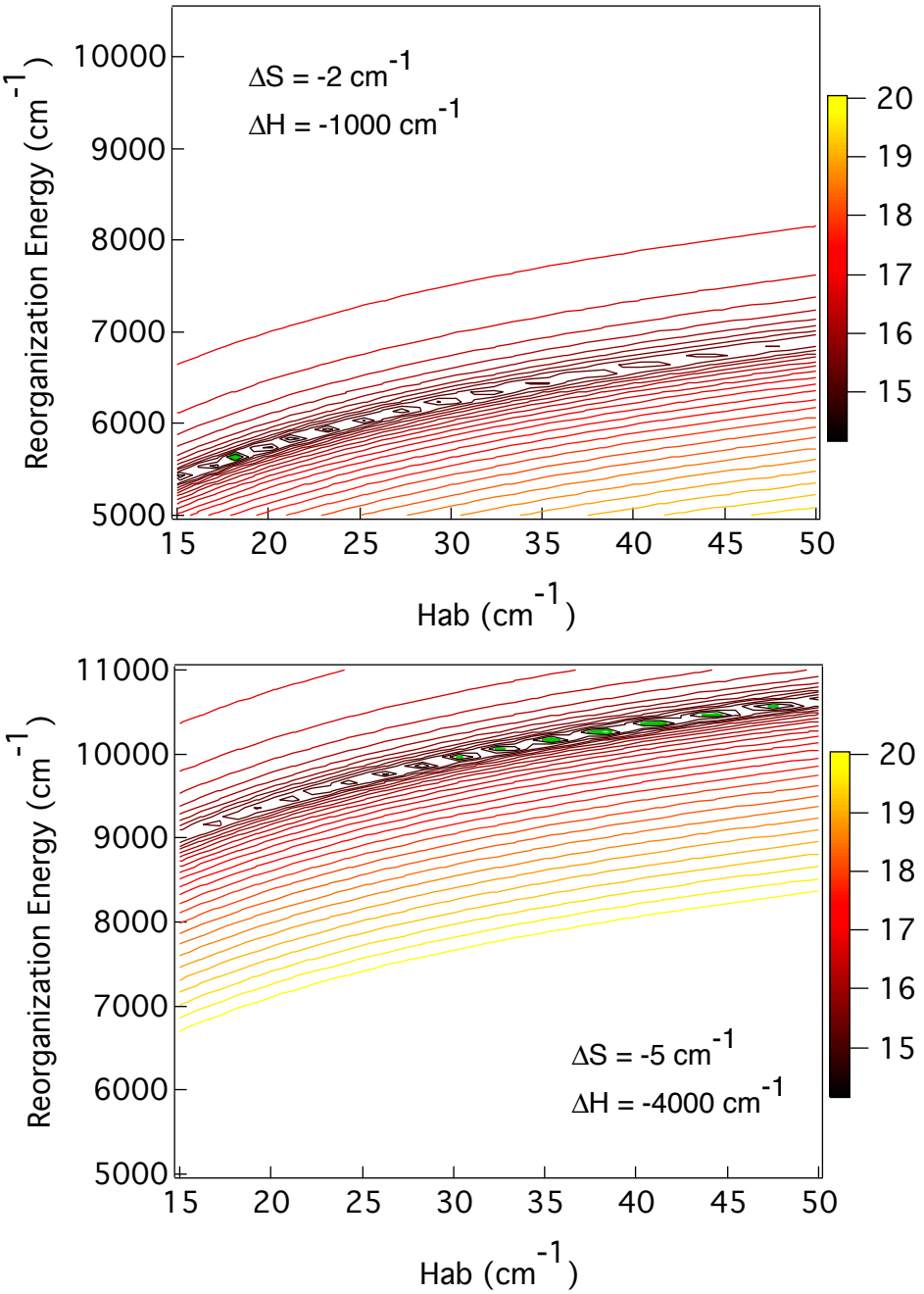

Figure 4-7: Contour plots of $[Fe(paniterpy)_2]^{2+}$ showing the error associated with the fits using the range of Hab and λ values shown. Smaller values represent better fits, with green indicating the smallest error fits. With the ΔS and ΔH values used for the fits, a range of coupling constants (17 – 50 cm^{-1}) and reorganization energies (5500 – 10,000 cm^{-1}) were calculated.

The unsubstituted complex requires a smaller reorganization energy for ground state recovery, while a small increase in λ is seen for addition of both the t-butyl and pani substituent. As was seen for the Arrhenius equation, any addition to the parent terpy ring has the effect of increasing reorganization energy with little difference between aromatic and aliphatic or between the amount of steric bulk.

Whereas no trend was found between ligand substituent and reorganization energy, a correlation does seem to be present between the frequency factor determined from fits to the Arrhenius equation and the coupling constant determined from Marcus theory fits. A larger coupling constant accompanies the pani substituent, providing information on the origin of the faster rate associated with this complex. Although the ligand shows no evidence of increased electronic coupling in the ground state, there is evidence that excited state species do change geometry and can decrease the angle between aromatic rings with respect to the plane of the rest of the ligand.[14,15]

The ground state recovery rates for the terpy series were not as straightforward as was originally predicted. Although it was expected that steric bulk would increase the ground state recovery rate, it is clear that the physical barrier to twisting is not the only influence on the rate. By fitting the variable temperature data to both the Arrhenius equation and Marcus theory for electron transfer equation, contributions from activation barriers as well as electronic couplings have been extracted. Due to the large errors associated with these variables, it is difficult to identify quantitative trends associated with the ligand sets. However, qualitative outliers can be identified. It is clear that adding a physical barrier to the twisting motion has the effect of increasing the activation barrier and reorganization

energy. Also, addition of aromatic groups increases the electronic coupling that facilitates ground state recovery.

One explanation that has been considered to account for these results involves the placement of the ground state potential surface in relation to the excited state along the reaction coordinate. If the motion associated with the transition is the torsional twist accompanied by a bond length change (as has been shown in other molecules), it is reasonable to think that the more steric hindrance there is, the closer the ground state geometry is to the excited state geometry. With less motion required to reach the excited state geometry, less reorganization energy would be required to complete the transition. Although this argument is consistent with the data presented in chapter 3 for the $[Fe(R\text{-}tren(py)_3)]^{2+}$ series, the more sterically hindered complexes in this series - which would push the ground state geometries closer to those of the excited states - have the larger reorganization energies. Ground state optimized geometries (N-Fe-N bond angles and Fe-N bond lengths) are also quite similar for the series. Substitutions at the meta position mitigate electronic inductive effects as does the orthogonal angle of the aromatic groups to the rest of the terpy ligand.

The second explanation for the trends shown in this series is that the aliphatic substituents behave exactly as would be predicted by the literature. Addition of the t-butyl group, for example, increases the activation barrier, reorganization energy, and the electronic coupling in relation to the unsubstituted parent complex. The same effects are also present in the adamantyl substituted ligand, but the aromatic complexes deviate from expectations. This deviation could be explained by the allowing for increased electronic communication of the methoxy group with the terpy. Electronic differences in the excited

state would create discrepancies from the expected correlation between complexes. In other words, all bets are off if the methoxy groups are no longer orthogonal and have some electronic interaction with the ligand.

Excited state geometry optimizations would provide information about the relative angular orientation of the aromatic groups in the excited state and help quantify the effect that orientation would have on the electronic communication between the terpy ligand and the aromatic substituent. This would help to elucidate the nature of the steric effect that the ligands produce as well as the extent to which the orthogonal geometry between the parent terpy ring and the methoxy ring of the aromatic substituents is maintained throughout the excitation and subsequent relaxation. Changes in geometry throughout the transition would have implications for the electronic coupling involved in the excited state as compared to the ground state.

Charge Transfer State Deactivation:

Study of ground state recovery has been well documented and studied over the years and for many classes of molecules. The difference with the study presented herein is the coupled examination of ground state recovery along with the deactivation of the initially excited charge transfer state. A similar set of experiments to those just presented for ground state recovery was performed on a shorter timescale. Due to the recent commercialization of ultrafast lasers such as the ones used in this spectrometer, the ability to examine processes on ultrashort timescale is very recent.

As was discussed in chapter 2, in order to follow the kinetic process, spectroscopic signatures for starting and ending states must be identified. In this case of the charge transfer deactivation, the starting state is the initially excited metal-to-ligand charge

transfer state and the ending state is the long-lived $^5T_2$ ligand field excited state just discussed. Using spectroelectrochemistry, a spectroscopic tag for this state can be identified.[16] The grow in and subsequent decay of this state can be monitored by watching the positive signal associated with the ligand radical decay to a negative signal corresponding to the metal centered state. This signal is universal for low-spin iron(II) polypyridyl complexes studied on this timescale and has been positively identified for $[Fe(terpy)_2]^{2+}$.[17,18]

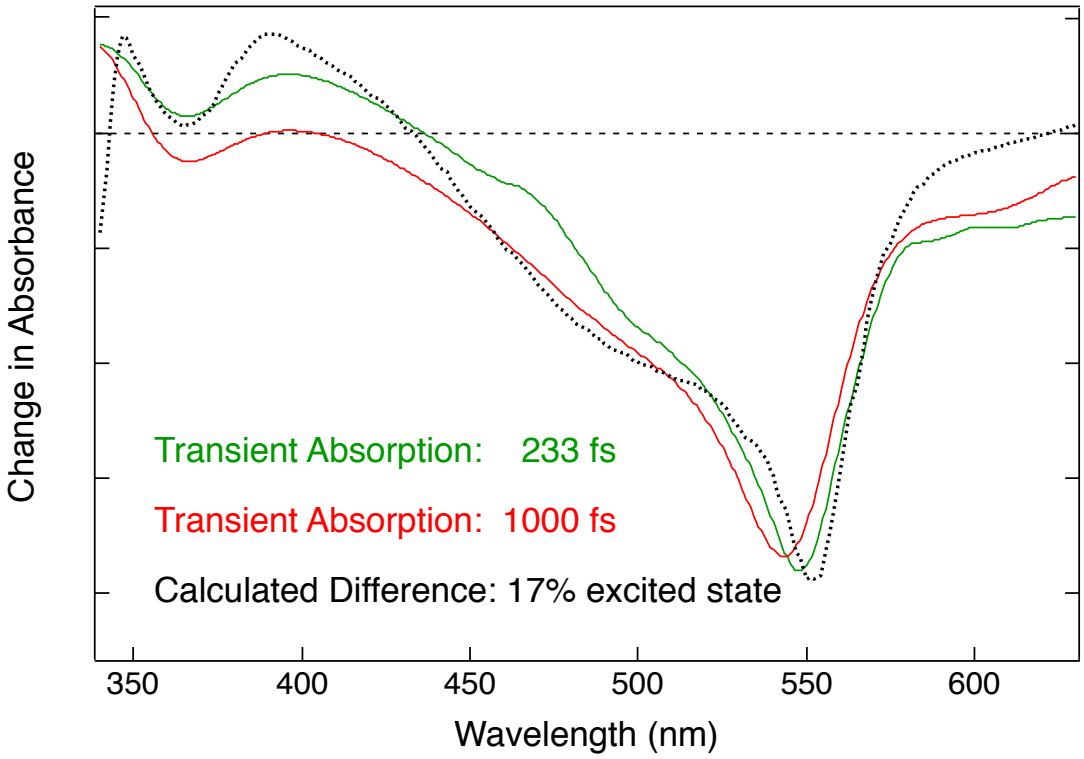

Figure 4-8: Difference spectra for $[Fe(terpy)_2]^{2+}$ from transient absorption spectroscopy at 233 fs (green), 1000 fs (red) after photoexcitation at 560 nm and the calculated spectrum from spectroelectrochemistry (black). The calculated spectrum represents the signature of the charge transfer species. The features associated with the charge transfer species are present at early time, but go away at later time, indicating a change in excited state identity.

The spectra shown in Figure 7 correspond to the $[Fe(terpy)_2]^{2+}$ species 233 fs (green) and 1000 fs (red) after photoexcitation. The black spectrum is the theoretical charge transfer species calculated through the methods discussed in Chapter 2. Immediately following photoexcitation, spectroscopic features matching those of the calculated charge transfer species are present. As soon as 1 ps after initial excitation, however, these features are gone. Figure 8 shows a more detailed progression of the decay of the feature centered around 400 nm. The new spectrum is associated with the long-lived ligand field state and has a time constant of 5.4 ns in acetonitrile.

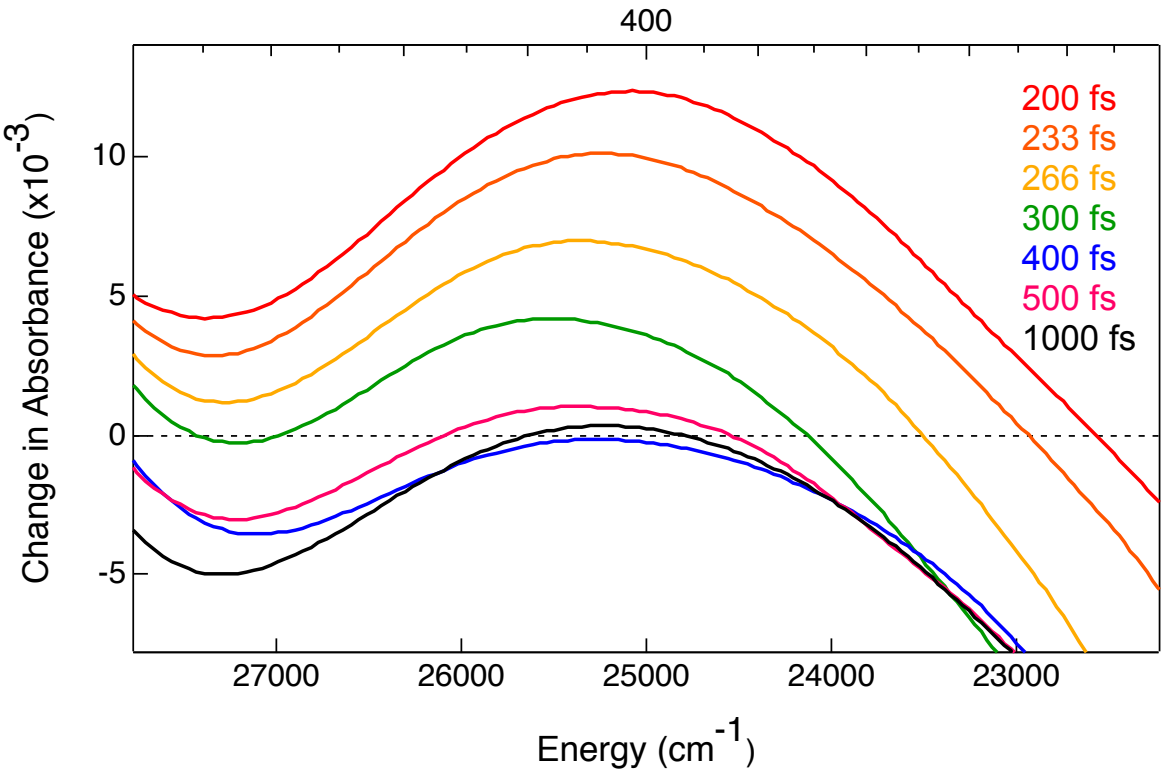

Figure 4-9: Early time spectral snapshots of $[Fe(terpy)_2]^{2+}$ immediately following photoexcitation at 560 nm. The initial positive feature that decays to a negative feature around 410 nm is a clear transition of species from the charge transfer state to the ligand field state.

Although the basic shape and kinetics for this transition are the same throughout the series, the presence of the aromatic substituents produced a shift of the positive-to-negative feature. As shown in Figure 9 which compares the spectra of the complexes at 1 ps after excitation, the positive feature centered at 400 nm never changes sign in the aromatic systems. Conversely, no positive feature is seen red of this signal for the unsubstituted and aliphatic complexes.

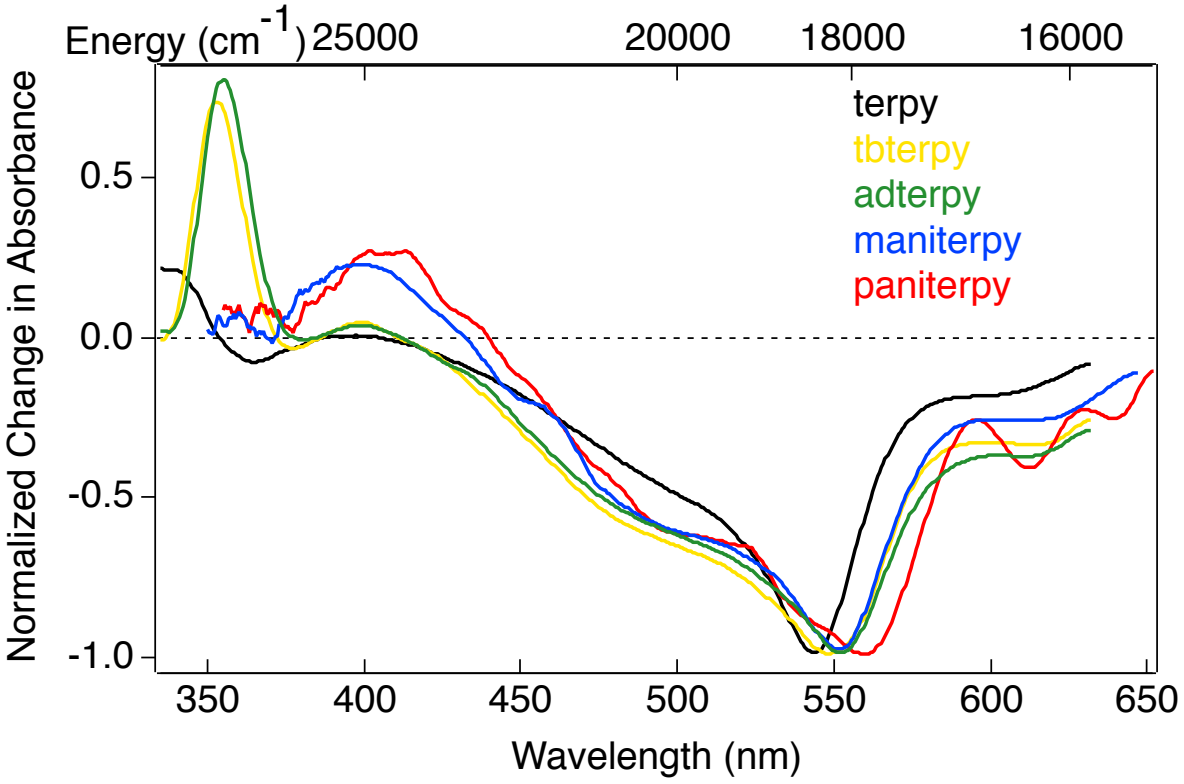

Figure 4-10: Spectral snapshots of the difference spectra for the $[Fe(terpy)_2]^{2+}$ series at 1 ps after photoexcitation at 560 nm. Although the general shape is similar, the difference in aromaticity of the substituents has a slight effect on the ligand radical placement.

For this reason, different probe wavelengths were used to monitor the positive-to-negative signals and measure the kinetics associated with the charge transfer-to-ligand field transitions shown in Figures 10 and 11.

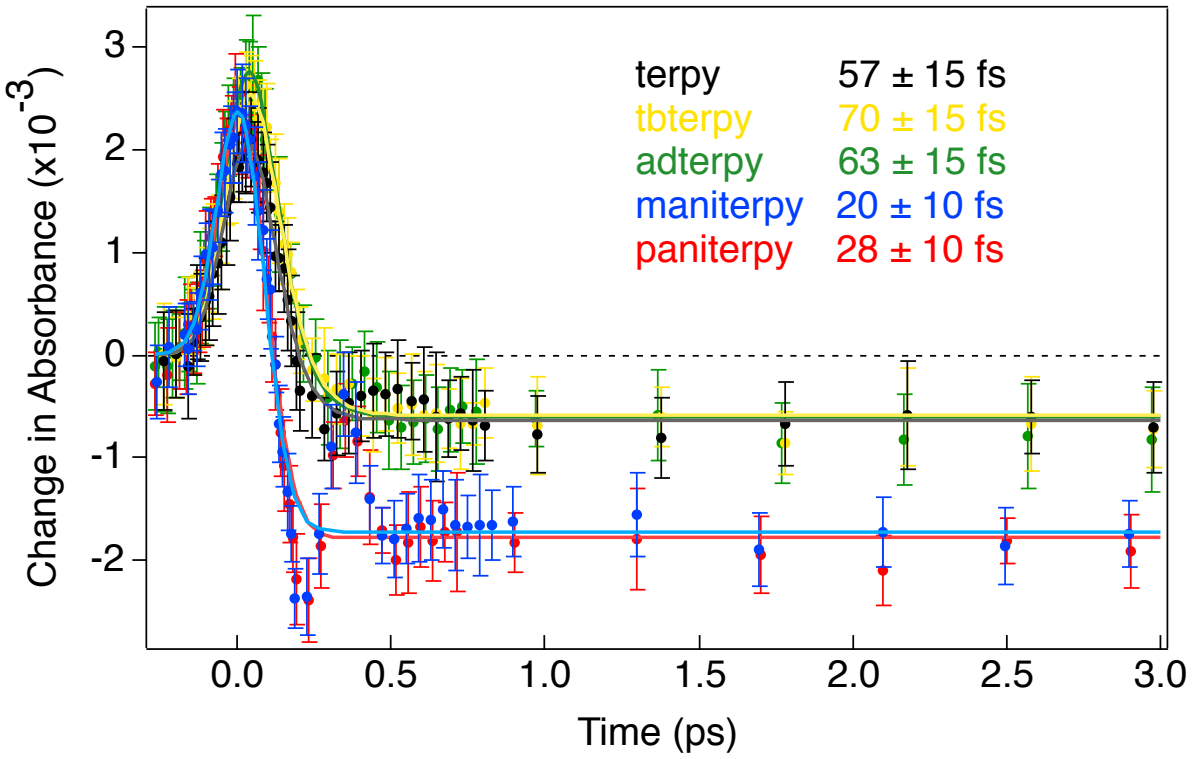

Figure 4-11: Charge transfer to ligand field transition for the $[Fe(terpy)_2]^{2+}$ series along with the deconvolved fits. Following 560 nm excitation, the protio and aliphatic complexes were probed at 410 nm while the aromatic complexes were probed at 450 nm. Solid lines represent the deconvolved fits with the time constants listed in the legend and a 75 fs instrument response function.

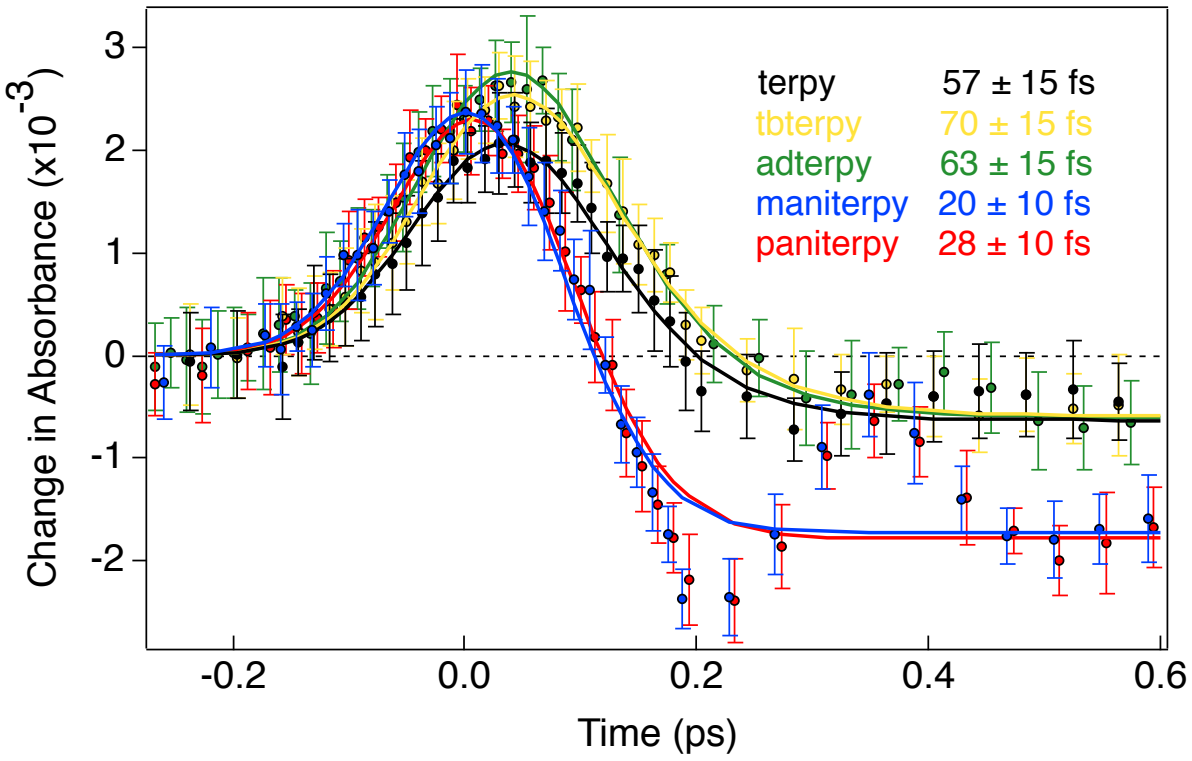

Figure 4-12: Zoom-in of Figure 10 with the early-time kinetic traces for the $[Fe(terpy)_2]^{2+}$ series and deconvolved fits.

Figures 10 and 11 show the data and deconvolved fits for the terpy series on the ultrashort timescale. All complexes were excited at 560 nm with absorbance values between 0.4-0.6. The unsubstituted and aliphatic substituted complexes were probed at 410 nm while the aromatic substituted complexes were probed at 450 nm. These wavelengths were chosen to maximize the positive-to-negative amplitude changes for each molecule. Time zero was identified by measuring the solvent response for each pump/probe wavelength combination. This solvent signal was more prominent at 450 nm probe and the signal can be seen at later times in the traces for the aromatic complexes. Figure 12 shows the trace for the paniterpy along with the acetonitrile solvent signal. The deconvolution program used is of local origin and allows for optimization of the fit using t0,

IRF, long-time offset, amplitudes, and time constants for 1-3 exponential functions. In order to fit the traces with the oscillations, those points were omitted during deconvolution. Errors on the fits were determined by iterative fitting with different time constants that reasonably fit both the rise and the decay of the signal as evaluated by eye. All time constants were ascertained using the same IRF of 75 fs.

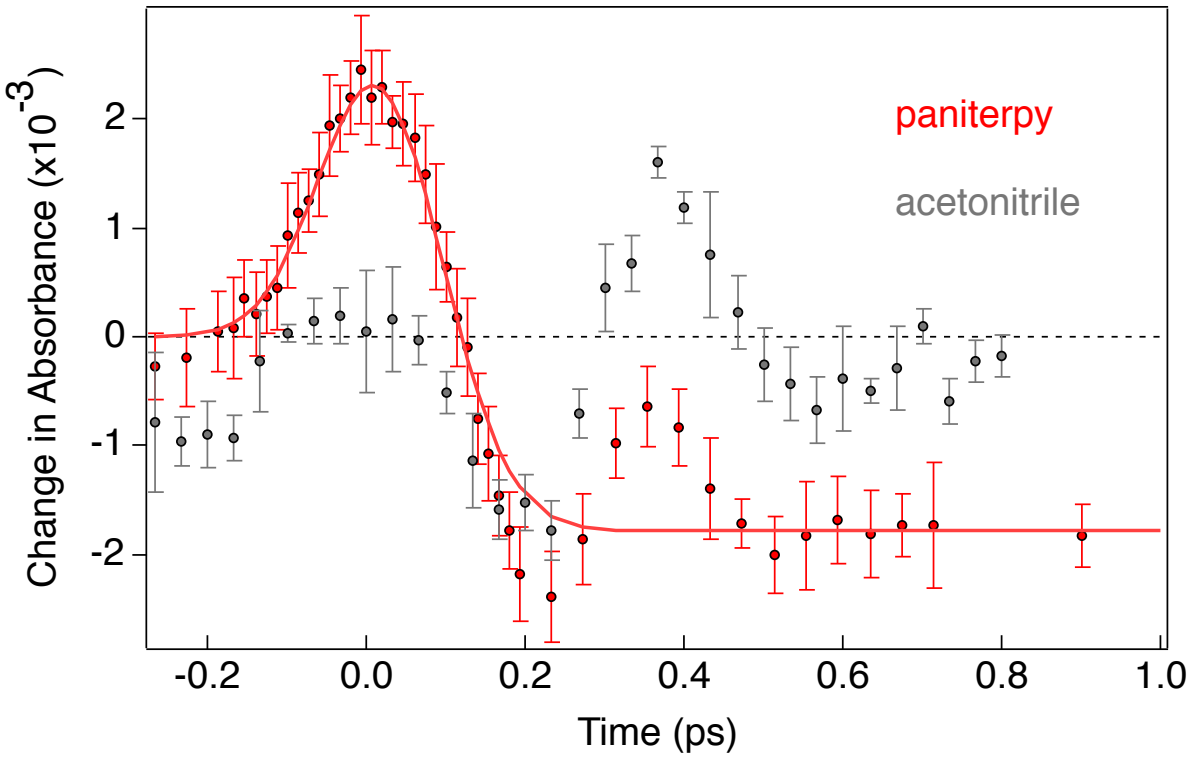

Figure 4-14: Early time kinetic trace of $[Fe(paniterpy)_2]^{2+}$ along with the solvent response from acetonitrile.

The fits from Figures 10 and 11 show a trend in rates that can be separated into two categories: unsubstituted/aliphatic substituents and aromatic substituents. When comparing the unsubstituted terpy with the t-butyl and adamantyl aliphatic substituents, a slight increase in charge transfer-to-ligand field conversion time is detectable. It should be noted, however, that the values are within the error associated with the measurement so definite conclusions cannot be made about steric bulk affecting the charge transfer

deactivation rate based on this data alone. The rates of deactivation for the aromatic substituted complexes are outside of experimental error and can be said to be different from the unsubstituted and aliphatic complexes, although not different from each other. These aromatic substituents do have a similar rate increasing effect for the charge transfer deactivation as they did for the ground state recovery.

Although it would provide more information about the behavior of these systems, variable temperature transient absorption data is not a practical possibility for measurements on the 35 fs system: extra glass introduced into the sample holder from the dewar adds chirp to the system, finding the correct overlap in the dewar would be extremely difficult at best, the amount of white light getting through the setup will be drastically reduced, and scatter issues will be amplified. If absolutely necessary, these problems could be overcome, but a practical limit to the amount of information gained should be taken into consideration. For this case, the goal is to increase the charge transfer state lifetime to 10 ps, or a factor of 100 longer than the current lifetime. This corresponds to a decrease in the coupling constant by a factor of ten. A simple calculation can be made to estimate the coupling constant for this process.

The energy separation between the $^1A_1$ ground state and $^5T_2$ lowest energy excited state of terpy is thought to lie in between that for tren (~1000 cm^{-1})[19] and bpy (~6000 cm^{-1})[9]. The reorganization energy between the ^{1}MLCT and $^5T_2$ is predicted to be similar to the reorganization energy between $^5T_2$ and $^1A_1$ due to the similar spin state changes and the greatest structural change coming from population of the $^5T_2$ state. The onset of the

absorption spectrum of the ground state can provide an approximate energy splitting for the $^1A_1$ and ^{1}MLCT. These values allow for the estimation of the energy separation between the ^{1}MLCT and $^5T_2$. By assuming a reorganization energy 7000 cm^{-1} and 13,500 cm^{-1} energy separation, a coupling constant of 10,000 cm^{-1} is necessary to produce a charge transfer deactivation rate on the order of $1x10^{13}$ s^{-1}. In order to decrease the rate to $1x10^{11}$ (which would allow for efficient electron injection) the coupling constant must be decreased by a factor of 10.

Coupling between the ^{1}MLCT and $^5T_2$ excited states might occur by a number of mechanisms. First, the density of ligand field states that may be involved in coupling the states is quite large. Although the singlet to quintet transition is $\Delta S=2$ and should be slow due to its spin-forbidden nature, the ultrafast transition infers extensive mixing of the states. This is both electronically and energetically reasonable. Second, it is well documented that charge transfer states respond to solvent effects. These effects have also been seen for ligand field transitions (which will be discussed further in chapter 6). Solvent modulated coupling could occur through the stabilization of the metal centered states where the charged ligand is less favorable. Finally, the ^{1}MLCT and $^5T_2$ transition is in the Marcus normal region. As the driving force increases, so should the coupling, manifesting in a faster rate. This argument is supported by the similar responses of the substituted complexes for both transitions.

The final effort in this direction of the project is to make a cage ligand with very little structural flexibility. The thought is to restrict all movement; both the torsional twist and

the bond elongation. Because the ^{1}MLCT excited and $^{1}A_1$ ground states are thought to have similar geometries, photoexcitation can result in population of the charge transfer state, but reorganization will be hindered to the extreme and formation of the $^{5}T_2$ state will be as difficult as we can think to make it.

REFERNCES

References: Chapter 4

(1) McCusker, J. K.; Rheingold, A. L.; Hendrickson, D. N. *Inorganic Chemistry* **1996**, *35*, 2100.

(2) Spartan calculations were performed by Lindsey Jamula.

(3) Purcell, K. F. *Journal of the American Chemical Society* **1979**, *101*, 5147.

(4) Buhks, E.; Navon, G.; Bixon, M.; Jortner, J. *Journal of the American Chemical Society* **1980**, *102*, 2918.

(5) McCusker, J. K.; Walda, K. N.; Dunn, R. C.; Simon, J. D.; Magde, D.; Hendrickson, D. N. *Journal of the American Chemical Society* **1993**, *115*, 298.

(6) McCusker, J. K.; Toftlund, H.; Rheingold, A. L.; Hendrickson, D. N. *Journal of the American Chemical Society* **1993**, *115*, 1797.

(7) Creutz, C.; Chou, M.; Netzel, T. L.; Okumura, M.; Sutin, N. *Journal of the American Chemical Society* **1980**, *102*, 1309.

(8) Bergkamp, M. A.; Chang, C. K.; Netzel, T. L. *Journal of Physical Chemistry* **1983**, *87*, 4441.

(9) Gawelda, W.; Cannizzo, A.; Pham, V. T.; van Mourik, F.; Bressler, C.; Chergui, M. *Journal of the American Chemical Society* **2007**, *129*, 8199.

(10) McCusker, J. K.; Walda, K. N.; Dunn, R. C.; Simon, J. D.; Magde, D.; Hendrickson, D. N. *Journal of the American Chemical Society* **1992**, *114*, 6919.

(11) Geometry calculations were performed by Lindsey Jamula.

(12) Loren, J. C.; Gantzel, P.; Linden, A.; Siegel, J. S. *Organic & Biomolecular Chemistry* **2005**, *3*, 3105.

(13) This change in lifetime with a different solvent will be addressed more completely in chapter 6.

(14) Damrauer, N. H.; Weldon, B. T.; McCusker, J. K. *Journal of Physical Chemistry A* **1998**, *102*, 3382.

(15) Damrauer, N. H.; Boussie, T. R.; Devenney, M.; McCusker, J. K. *Journal of the American Chemical Society* **1997**, *119*, 8253.

(16) Monat, J. E.; McCusker, J. K. *Journal of the American Chemical Society* **2000**, *122*, 4092.

(17) Smeigh, A. L., Brown, A. M., McCusker, J. K. *Manuscript in Preparation* **2011**.

(18) Brown, A. M.; McCusker, C. E.; McCusker, J. K. *Manuscript in Preparation* **2011**.

(19) Conti, A. J.; Xie, C. L.; Hendrickson, D. N. *Journal of the American Chemical Society* **1989**, *111*, 1171.

Chapter 5: Geometry Effect on Rates

Chapter 4 discusses an attempt to decrease the charge-transfer to ligand-field conversion of Fe^{2+} polypyridyl complexes through the inhibition of one mode of motion that has been previously reported to affect the ground state recovery process in these molecules. Although the experiments provided a good foundation and some encouraging results for correlating the reaction coordinates for both charge transfer state deactivation and ground state recovery, it became clear early on in the research that another avenue to extend the charge transfer state lifetime should be pursued concurrently.

Achieving Octahedral Geometry

A pictorial representation for the electronic structure of low spin d^6 complexes was shown in chapter 3. The picture shown and the Tanabe-Sugano diagrams from which it is based assume octahedral geometry with regards to the metal center. Octahedral symmetry supports the three-fold symmetry seen in the diagram and the "T" state manifesting as the low energy excited state for the iron(II) complexes studied. The substituted terpy ligands that were discussed take on a formal D_{2d} symmetry with a "pseudo-octahedral" geometry in the nitrogen environment surrounding the metal center. Although the environment around the iron center in these complexes is pseudo-octahedral, bond angles are not the 180/90 required for true octahedral symmetry. As soon as octahedral symmetry is removed, the three-fold degeneracy that is supported in O_h symmetry is reduced. Each of the T states are, therefore, split. With more energy levels, the density of states and coupling

between them may increase and provide a faster route from initially excited charge transfer state to ligand field manifold.

In order to decrease the number/density of states between charge transfer and lowest energy ligand field states as much as possible, a ligand set designed to place the Fe^{2+} complex as close to octahedral geometry as possible was the goal. A ruthenium-based complex with an extended terpy-type ligand and nearly perfect octahedral geometry was reported in early 2009.[1] Lindsey Jamula was able to modify the synthetic procedure in order to prepare the Fe^{2+} analog of the complex, $[Fe(dkpp)_2]^{2+}$, where dkpp is 2,6-di(2-ketopyridyl)pyridine.[2] Figure 1 is a picture of the crystal structure as solved by Dr. Dong Guo and Tables 1 and 2 provides relevant bond lengths and angles.

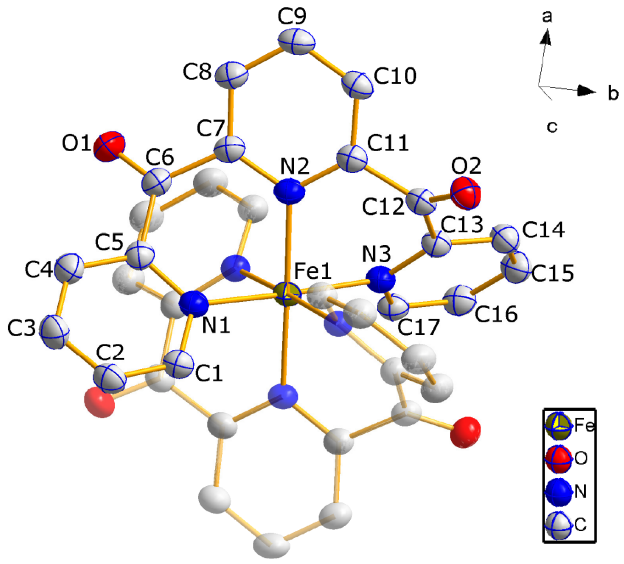

Figure 5-1: Crystal structure of $[Fe(dkpp)_2]^{2+}$.

Table 5-1: Selected bond lengths from the $[Fe(dkpp)_2]^{2+}$ crystal structure.

Atoms	X-ray Crystal Bond Length (Å)
Fe1—N2^{i}	1.972(2)
Fe1—N2	1.972(2)
Fe1—N1	1.982(2)
Fe1—N1^{i}	1.982(2)
Fe1—N3^{i}	1.986(2)
Fe1—N3	1.986(2)

Table 5-2: Selected bond angles from the $[Fe(dkpp)_2]^{2+}$ crystal structure.

Atoms	X-ray Crystal Bond Angles (°)
N2^{i}—Fe1—N2	178.82(12)
N2^{i}—Fe1—N1	90.31(9)
N2—Fe1—N1	88.86(9)
N2^{i}—Fe1—N1^{i}	88.86(9)
N2—Fe1—N1^{i}	90.31(9)
N1—Fe1—N1^{i}	90.64(12)
N2^{i}—Fe1—N3^{i}	88.92(9)
N2—Fe1—N3^{i}	91.90(9)
N1—Fe1—N3^{i}	88.95(9)
N1^{i}—Fe1—N3^{i}	177.74(8)
N2^{i}—Fe1—N3	91.90(9)
N2—Fe1—N3	88.92(9)
N1—Fe1—N3	177.74(8)
N1^{i}—Fe1—N3	88.95(9)
N3^{i}—Fe1—N3	91.54(12)

The pyridine rings making up the backbone of the ligand are not directly bonded to one another. This spatially removes the rings from direct electronic communication with each

other and limits aromatic interaction. The carbonyls are proposed to assist in the conjugation between pyridyl rings, extending the pi system further than for the bpy and terpy ligands. Although there is a relatively large canted angle between rings, the position of the carbonyl group seems to bridge the gap and provide a mechanism for conjugation throughout the ligand.

As shown in Figure 2, the average N-Fe-N bond angles for $[Fe(dkpp)_2]^{2+}$ are much closer to the 90°/180° expected for an octahedral geometry than either $[Fe(terpy)_2]^{2+}$ (D_{2d}) or $[Fe(bpy)_2]^{2+}$ (D_3), which have been shown to have rapid charge transfer deactivation.[3,4]

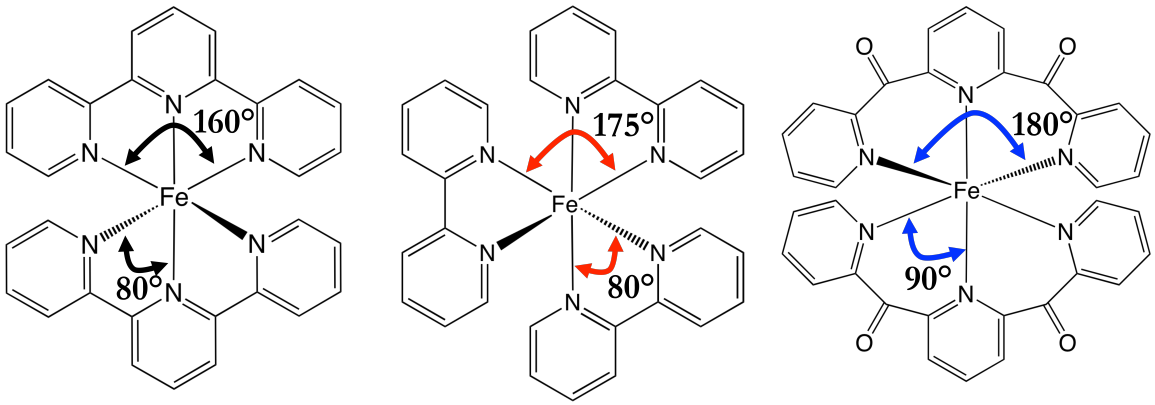

Figure 5-2: Structures and average bond angles for $[Fe(dkpp)_2]^{2+}$(blue), $[Fe(bpy)_3]^{2+}$(red), and $[Fe(terpy)_2]^{2+}$(black). The geometry around the iron center is much closer to octahedral for $[Fe(dkpp)_2]^{2+}$ than $[Fe(bpy)_3]^{2+}$ and $[Fe(terpy)_2]^{2+}$.

The impact of the desired ligand geometry was immediately noticed through the color of the complex and ground state electronic absorption spectrum (Figure 3). Iron(II) complexes contain both metal-to-ligand charge transfer as well as ligand field transitions, but similar energy separation for both sets of orbitals buries the weaker metal-based absorptions under the much more intense charge transfer bands. Since the assignments for $[Fe(bpy)_3]^{2+}$ and $[Fe(terpy)_2]^{2+}$ have previously been established,[5] the electronic

absorption spectrum of $[Fe(dkpp)_2]^{2+}$ can be interpreted by comparison. As shown in Figure 3, all three complexes have strong absorptions in the visible corresponding to charge transfer transitions and resulting in vibrant coloring of both the solid and solution phases. The color of the complexes evolves from pink to purple to blue as the λ_{max} is shifted red, indicating a lower energy charge transfer transition (as is consistent with the electrochemical data, Table 1). Due to the breadth of the charge transfer absorption bands and the coincident energies of the spin-allowed ligand field transitions, the latter are buried beneath the former in both $[Fe(bpy)_3]^{2+}$ and $[Fe(terpy)_2]^{2+}$. The expected stronger ligand field associated with $[Fe(dkpp)_2]^{2+}$ is expected to push the ligand field transitions further to the blue, making separation from the charge transfer absorptions unlikely.

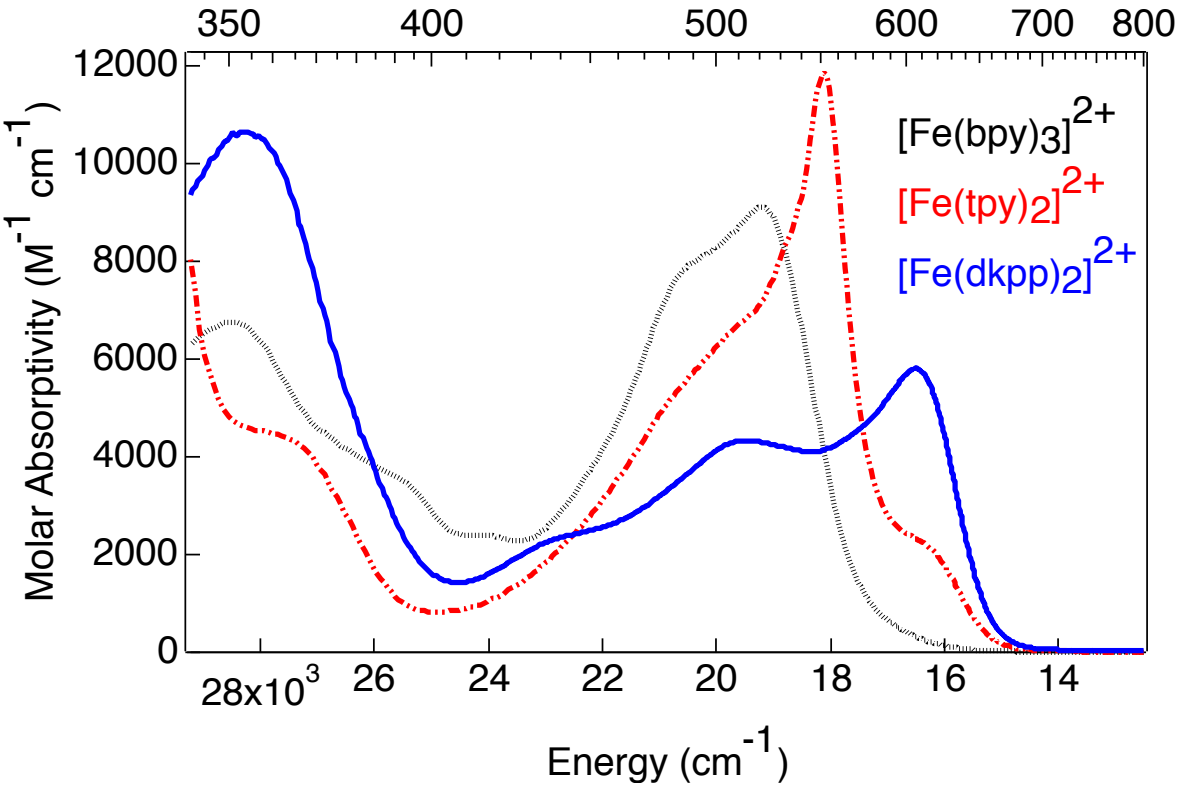

Figure 5-3: Ground state electronic absorption spectra for $[Fe(dkpp)_2]^{2+}$(blue), $[Fe(bpy)_3]^{2+}$(red), and $[Fe(terpy)_2]^{2+}$(black).

When compared as light absorbers in the context of sensitizers, the red-shifted absorption maximum for $[Fe(dkpp)_2]^{2+}$ increases the wavelength range that can be turned into useful energy. This is done without a loss in overall oscillator strength. The absorption spectra graphed in Figure 3 are plotted in terms of extinction coefficient. The more relevant measure of light absorbing ability is the oscillator strength, which can be measured by integrating the extinction coefficient spectrum of a complex when graphed as a function of energy (cm^{-1}) instead of wavelength (nm). Although the maximum extinction coefficient of $[Fe(dkpp)_2]^{2+}$ appears smaller than the other two complexes, the oscillator strengths are quite similar when integrated over energies from 25,000 cm^{-1} to 10,000 cm^{-1}. The similar oscillator strengths indicate similar light absorption behaviors. Based on these two properties (oscillator strength and low energy onset), $[Fe(dkpp)_2]^{2+}$ would make the better sensitizer.

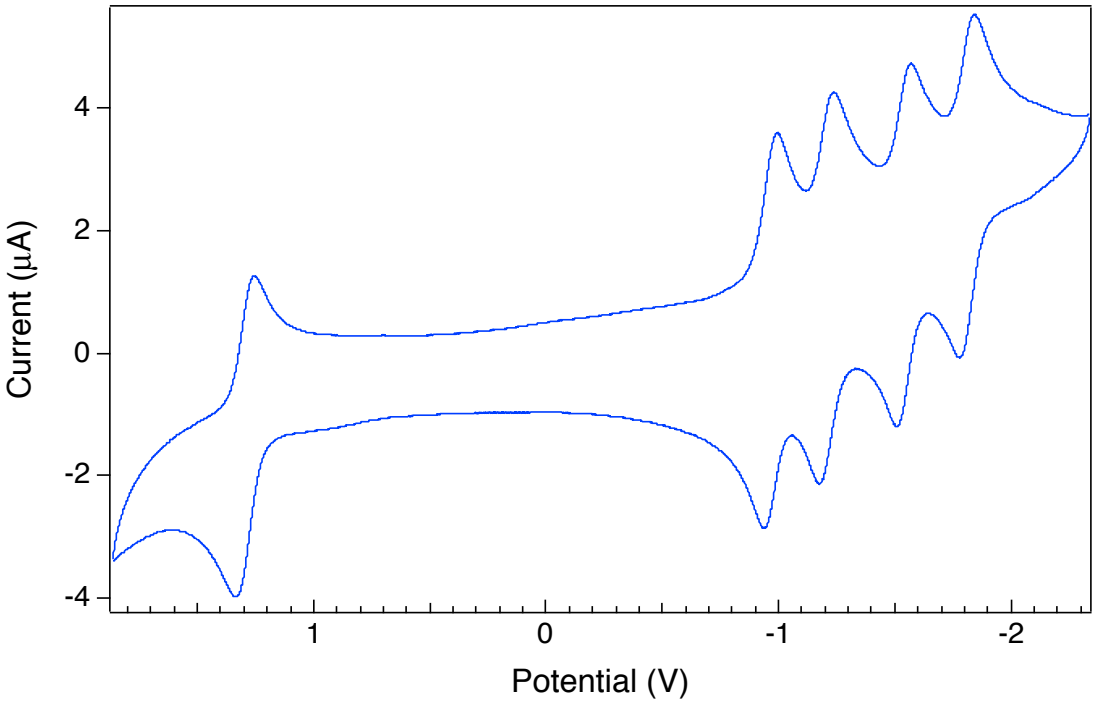

Figure 5-4: Cyclic voltammagram of $[Fe(dkpp)_2]^{2+}$.

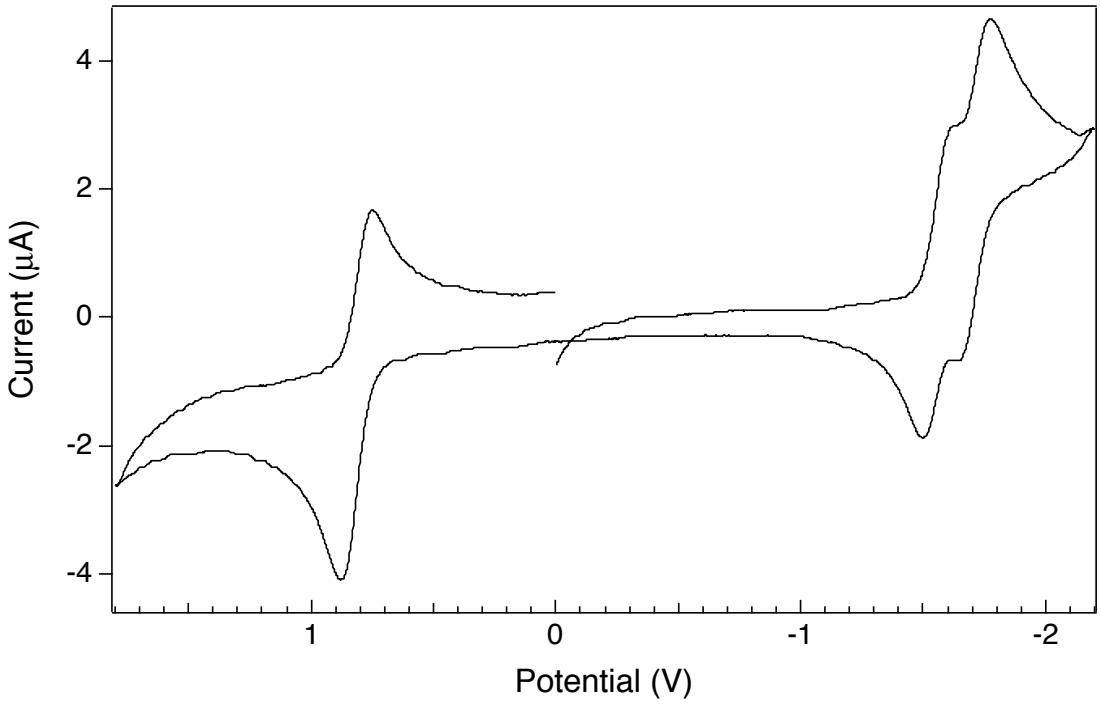

Figure 5-5: Cyclic voltammagram of $[Fe(terpy)_2]^{2+}$ in MeCN.

Two significant changes in electrochemical behavior were also measured: the number of reductions and their potentials. Figures 4 and 5 are the cyclic voltammagrams of $[Fe(dkpp)_2]^{2+}$ and $[Fe(terpy)_2]^{2+}$, respectively. From the CV plots, the first thing to notice is the difference in the number of peaks. Both $[Fe(dkpp)_2]^{2+}$ and $[Fe(terpy)_2]^{2+}$ have two ligands to reduce. $[Fe(terpy)_2]^{2+}$ has two corresponding reduction waves, but $[Fe(dkpp)_2]^{2+}$ has four. The difference implies two different mechanisms for reduction between the two complexes. With the presence of the carbonyl groups to assist in conjugation, electron movement and the loss of conjugation as a result may assist in the ability to accept four electrons. Figure 6 is a proposed scheme for these consecutive reductions of $[Fe(dkpp)_2]^{2+}$. Using the carbonyl groups, the incoming electron can be stabilized on one oxygen, while the other half of the ligand remains conjugated and able to accept the next electron.

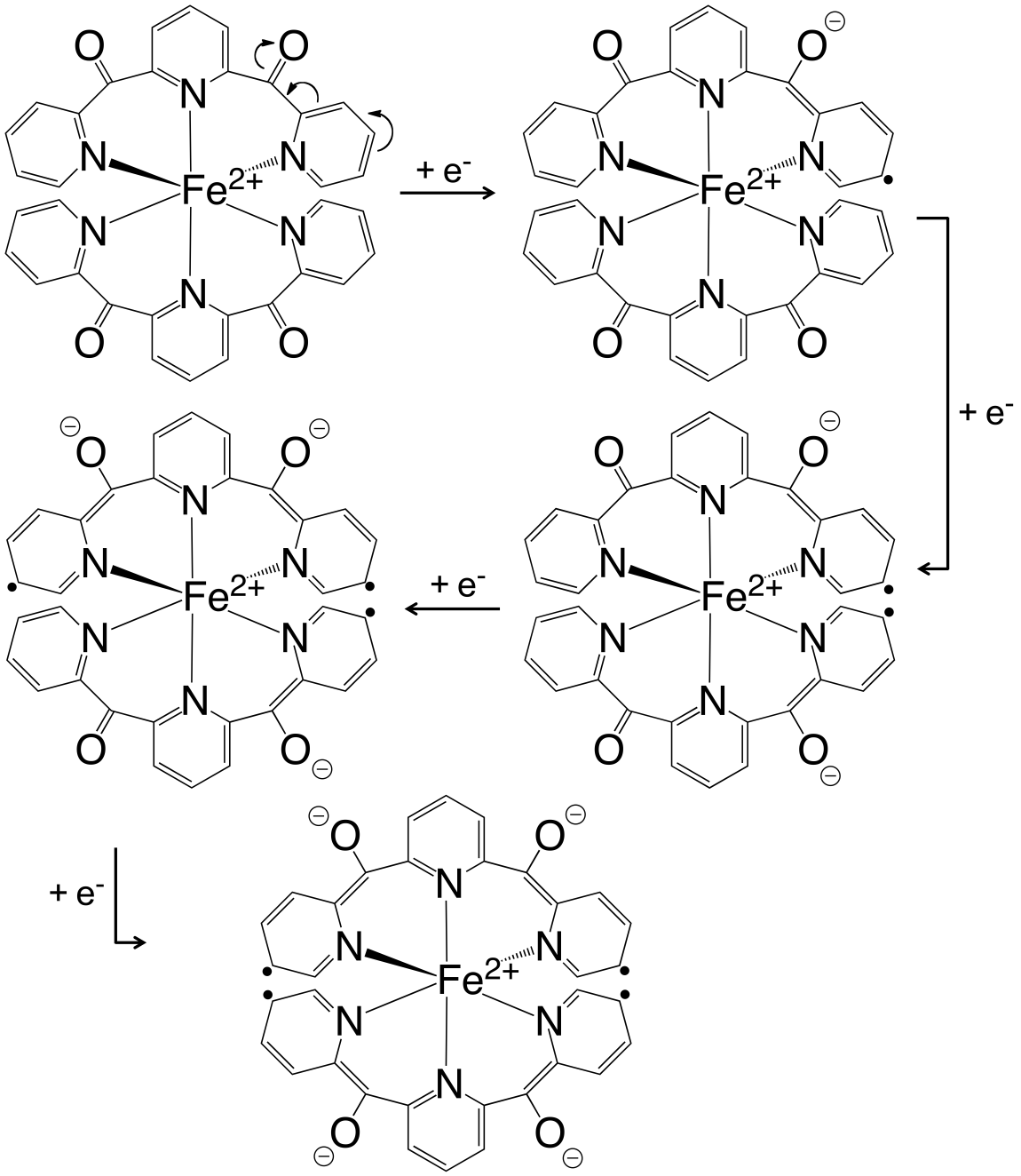

Figure 5-6: Proposed electron movement and species formed upon each successive reduction.

The other electrochemical difference shows up in the reduction potentials of the three complexes. Table 1 provides the electrochemical potentials for the $[Fe(dkpp)_2]^{2+}$, $[Fe(bpy)_3]^{2+}$, and $[Fe(terpy)_2]^{2+}$. Despite their differences in bite angles and chelation,

$[Fe(bpy)_3]^{2+}$ and $[Fe(terpy)_2]^{2+}$exhibit similar electrochemical behavior. The slight positive shift in the reduction potential would be predicted for the extended aromatic system of $[Fe(terpy)_2]^{2+}$ as compared to $[Fe(bpy)_3]^{2+}$. That difference, however, is small compared to what is observed for $[Fe(dkpp)_2]^{2+}$. The ~700 mV positive shift of the reduction potential infers an increased conjugation throughout the ligand as compared to $[Fe(terpy)_2]^{2+}$ that results in a dramatic stabilization of the π-system of the dkpp ligand. A similar positive shift in the Fe^{2+}/Fe^{3+} oxidation potential indicates less electron density at the metal center with the dkpp ligand than with terpy or bpy. The better geometric match of the ligand nitrogen orbitals with the metal σ–orbitals provides increased overlap and a stronger interaction. Increased bonding can be expected due to the better overlap, allowing stronger electron withdrawing character of the dkpp ligand provided by the carbonyl groups.

Table 5-3: Electrochemical potentials for the first oxidations and reductions of $[Fe(dkpp)_2]^{2+}$, $[Fe(bpy)_3]^{2+}$, and $[Fe(terpy)_2]^{2+}$. All complexes were measured in MeCN against a platinum disk working electrode in 0.1 M $TBAPF_6$ and externally referenced to Fc/Fc^+.

	Oxidation Potential	First Reduction Potential
$[Fe(dkpp)_2]^{2+}$	1.29 V	-0.97 V
$[Fe(bpy)_3]^{2+}$	0.66 V	-1.78 V
$[Fe(terpy)_2]^{2+}$	0.71 V	-1.68 V

Lowest Energy Ligand Field Excited State

The metal-based electronic structure of d^6 complexes was predicted through calculations[6] over 55 years ago and verified experimentally shortly thereafter[7]. High spin complexes have a $^5T_2$ ground state, while that is replaced by a $^1A_1$ ground state when the ligand field strength increases to a point where the low spin complex is more energetically favorable. For all known examples of iron(II) complexes, the ground state and lowest energy excited state of the low spin complex are inverted for the high spin complex. As discussed in chapter 2, a series of ultrafast experiments including transient absorption spectroscopy[8], raman spectroscopy[9], and X-ray absorption spectroscopy[10] have provided spectroscopic handles for each electronic state. Of specific interest is the ability to see the structural changes associated with transitioning between the high spin and low spin complexes. Identification of the motion associated with the transition can help to determine the relevant reaction coordinate to follow for kinetic and spectroscopic measurements. A similar X-ray absorption spectroscopy experiment was performed on $[Fe(bpy)_3]^{2+}$.[11] Time resolved structural changes established that the lowest energy excited state of $[Fe(bpy)_3]^{2+}$ is also $^5T_2$. A bond length change of approximately 0.2 Å was observed in both studies and is consistent with all studies on iron(II) complexes undergoing a $^5T_2$ <-> $^1A_1$ transition.

Although it has never been seen in any Fe^{2+} complex, Tanabe and Sugano determined that, given a strong enough ligand field, the lowest energy excited state of a low-spin d^6 complex will no longer be the $^5T_2$ but rather the $^3T_1$. Even the strong ligand field of

$[Fe(CN)_6]^{4-}$ is not strong enough to undergo this reorganization of lowest energy excited states[12]. However, with the additional charge density of Co^{3+} as compared to Fe^{2+}, the $^3T_1$ has been assigned as the lowest energy excited state for $[Co(CN)_6]^{3-}$.[13] This observation verifies that a strong enough ligand field will indeed invert the two lowest energy excited states. The following discussion presents evidence that the first example of an Fe^{2+} complex with a $^3T_1$ lowest energy excited state has been prepared. The implications that the complex of interest, $[Fe(dkpp)_2]^{2+}$, has a stronger ligand field than CN^- redefines the field of low-spin Fe(II) photophysics and expands the possible uses for this family of complexes. With a combination of the electrochemical and structural data already discussed along with lifetime data, a comparison between the complex of interest and known polypyridyl complexes provides evidence for the assignment of this unique species.

Along with the increase in orbital overlap due to the structural considerations discussed, the energetic match between the ligand π^* orbitals and the metal t_{2g} orbitals is also observed. Electrochemical measurements show a positive shift of 700 mV for the first reduction potential of $[Fe(dkpp)_2]^{2+}$ as compared to the $[Fe(bpy)_3]^{2+}$ and $[Fe(terpy)_2]^{2+}$, as is seen in Table 1. This shift has been attributed to the presence of the strongly electron withdrawing carbonyl groups. Stabilization of the ligand π^* orbitals allows for increased mixing with metal t_{2g} orbitals and results in a larger splitting of the t_{2g} and t_{2g}^* energy levels. The oxidation potential of these stabilized orbitals is shifted a correspondingly large 500 mV positive compared to the iron(II) reference complexes. When compared to the

Ru^{2+} analog, the Fe^{2+} complex shows a much larger positive shift in the oxidation potential. This is evidence that the mixing between the ligand and metal-based π orbitals is much larger in the iron ion than in the ruthenium counterpart. Shorter bonds and increased overlap are most likely the cause of this mixing.

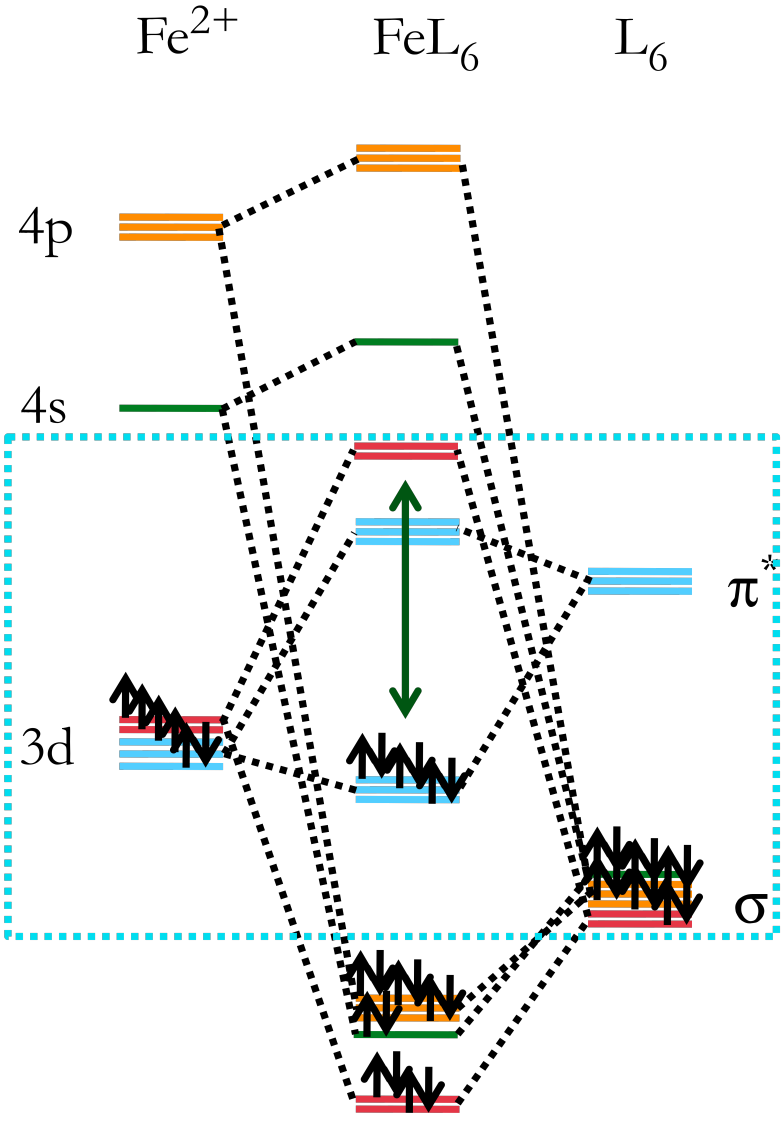

Figure 5-7: General molecular orbital diagram for $[FeL_6]^{2+}$. The region in the box will be expanded to describe the orbital movement affecting the observed photophysical and electrochemical differences between $[Fe(dkpp)_2]^{2+}$ and $[Fe(terpy)_2]^{2+}$.

The diagrams in Figures 7 and 8 provide a pictorial explanation of how the change in ligand set from terpy to dkpp has affected the ligand field strength. Figure 7 is a general molecular orbital diagram for a FeL_6^{2+} complex. Mixing between ligand and metal orbitals based on energetic match and electronic communication creates new molecular orbitals that combine and split to the extent that mixing occurs. Figure 8 compares that mixing/splitting between $[Fe(terpy)_2]^{2+}$ and $[Fe(dkpp)_2]^{2+}$ and the effect it has on the ligand field splitting/strength.[14] Arrows are numbered in the diagram to provide a clearer explanation of how each interaction affects the orbital movement.

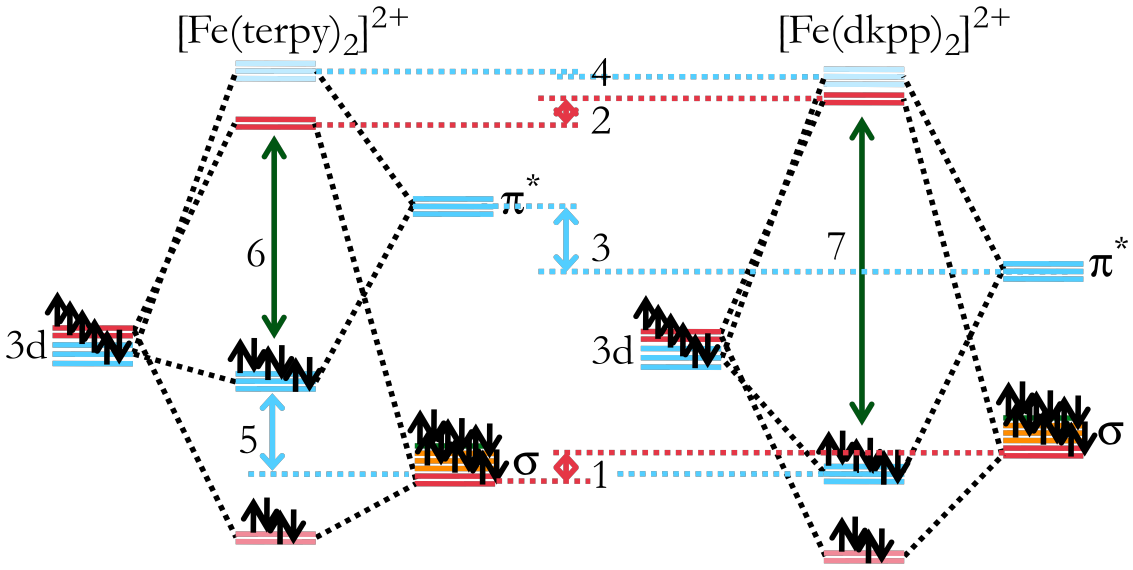

Figure 5-8: Molecular orbital diagrams for $[Fe(terpy)_2]^{2+}$ and $[Fe(dkpp)_2]^{2+}$ showing the effects of ligand orbital movement on ligand field splitting. No splitting shown in either diagram is measured or quantified.

Increased σ-interaction is introduced with the dkpp ligand due to the larger bite angle providing a more perfect octahedral geometry surrounding the metal center. Better overlap between the metal and ligand results in destabilization of the σ orbitals due to increased electron-electron repulsion. This is represented by arrow 1. Destabilization of

these ligand σ orbitals improves the energetic match between the atomic σ orbitals and results in larger splitting of the σ/σ^* orbitals. Arrow 2 represents the resulting destabilization of the metal-based σ^* (e_g^*) orbital. As indicated by electrochemistry, the reduction potential of the dkpp ligand is shifted significantly positive compared to the terpy ligand, which indicates a stabilization of the π^* orbitals (arrow 3). This has two effects: first, the barycenter of the π-symmetry molecular orbitals has a corresponding positive shift; second, the energetic match of these orbitals improves, increasing the mixing and splitting. The combination of these two movements results in a small (if any) shift of the π^* ligand-based molecular orbitals (arrow 4), along with a significant positive shift of the π-character t_{2g} metal-based orbitals (arrow 5). The combination of the destabilization of the e_g^* (arrow 2) and stabilization of the t_{2g} ligand field orbitals (arrow 5) has the effect of increasing the ligand field splitting, indicated by arrows 6 and 7.

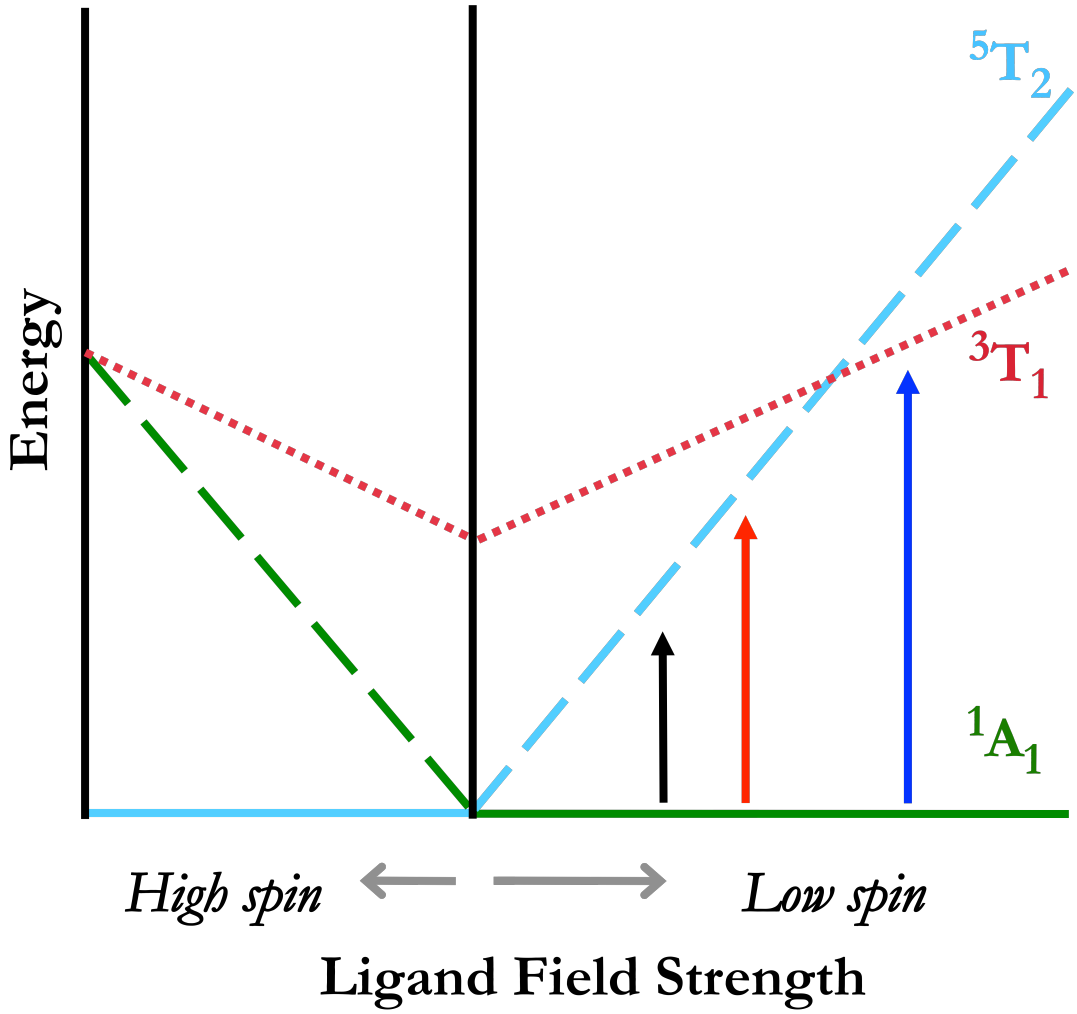

Figure 5-9: Tanabe-Sugano diagram for d^6 complexes. Arrows represent predicted relative ligand field strengths for $[Fe(terpy)_2]^{2+}$ (black), $[Fe(bpy)_2]^{2+}$ (red), and $[Fe(dkpp)_2]^{2+}$ (blue).

Moving from a molecular orbital picture to an energy level picture, Figure 9 brings back the d^6 Tanabe-Sugano diagram from chapter 2 with an extension of the strong field limit. The arrows on the diagram represent the relative (but not quantitative) ligand field strength proposed for $[Fe(terpy)_2]^{2+}$ (black), $[Fe(bpy)_2]^{2+}$ (red), and $[Fe(dkpp)_2]^{2+}$ (blue). The reorganization energy and energy gap for $[Fe(bpy)_2]^{2+}$ have been determined to be comparable, placing it at the barrierless region of a Marcus curve (Figure 10).[15]

Reorganization energies for all three complexes are expected to be similar due to the metal-based electronic states involved in the transition. The $^5T_2$ state has a $(t_{2g})^4(e_g^*)^2$ orbital population while the $^1A_1$ ground state has a $(t_{2g})^6$ orbital configuration. The 0.2 Å elongation upon population of the $^5T_2$ state is consistent with the population of e_g^* anti-bonding orbitals. With similar reorganization energies (as is expected for the $^1A_1$ <-> $^5T_2$ transition), both larger energy gaps and smaller energy gaps will predict slower relaxation processes.

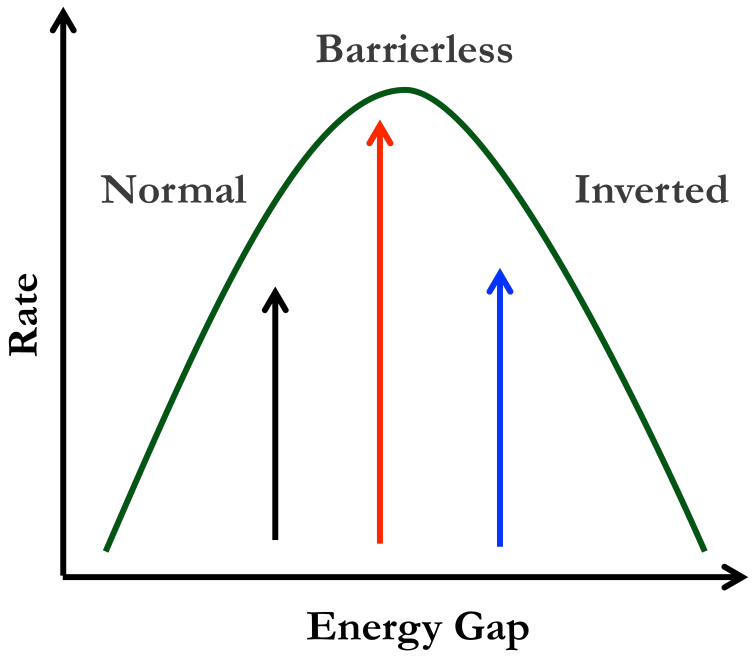

Figure 5-10: Marcus curve representing the $^5T_2 \rightarrow {}^1A_1$ transition for $[Fe(dkpp)_2]^{2+}$(blue), $[Fe(bpy)_3]^{2+}$(red), and $[Fe(terpy)_2]^{2+}$(black). With the understanding that $[Fe(bpy)_3]^{2+}$ is barrierless and the assumption that the electronic coupling is relatively constant for the three complexes, both $[Fe(dkpp)_2]^{2+}$ and $[Fe(terpy)_2]^{2+}$ should exhibit slower ground state recovery rates than $[Fe(bpy)_3]^{2+}$.

Invoking a Marcus theory explanation, we can use the respective energy gaps along with the assumption that the reorganization energies will not vary to a great extent to predict the trend in rates of ground state recovery for the series of interest. Ground state recovery time for $[Fe(bpy)_3]^{2+}$ is 0.96 ± 0.02 ns.[16] $[Fe(terpy)_2]^{2+}$ has an energy gap smaller than that of $[Fe(bpy)_3]^{2+}$, placing it in the normal region (λ is larger than ΔG). As shown in Figure 11, a relaxation time of 5.38 ± 0.10 ns has been measured for the ground state recovery of $[Fe(terpy)_2]^{2+}$.[17] The increased lifetime when compared to $[Fe(bpy)_3]^{2+}$ is expected and consistent with identical starting and ending electronic states. According to the electrochemical measurements and structural considerations already discussed, the energy gap for $[Fe(dkpp)_2]^{2+}$ has been predicted to be larger than that of $[Fe(bpy)_3]^{2+}$, yet the lifetime of $[Fe(dkpp)_2]^{2+}$ is 0.28 ± 0.04 ns. The decrease in lifetime when an increase is expected presents a divergence from the Marcus curve established for $[Fe(bpy)_3]^{2+}$ and $[Fe(terpy)_2]^{2+}$.

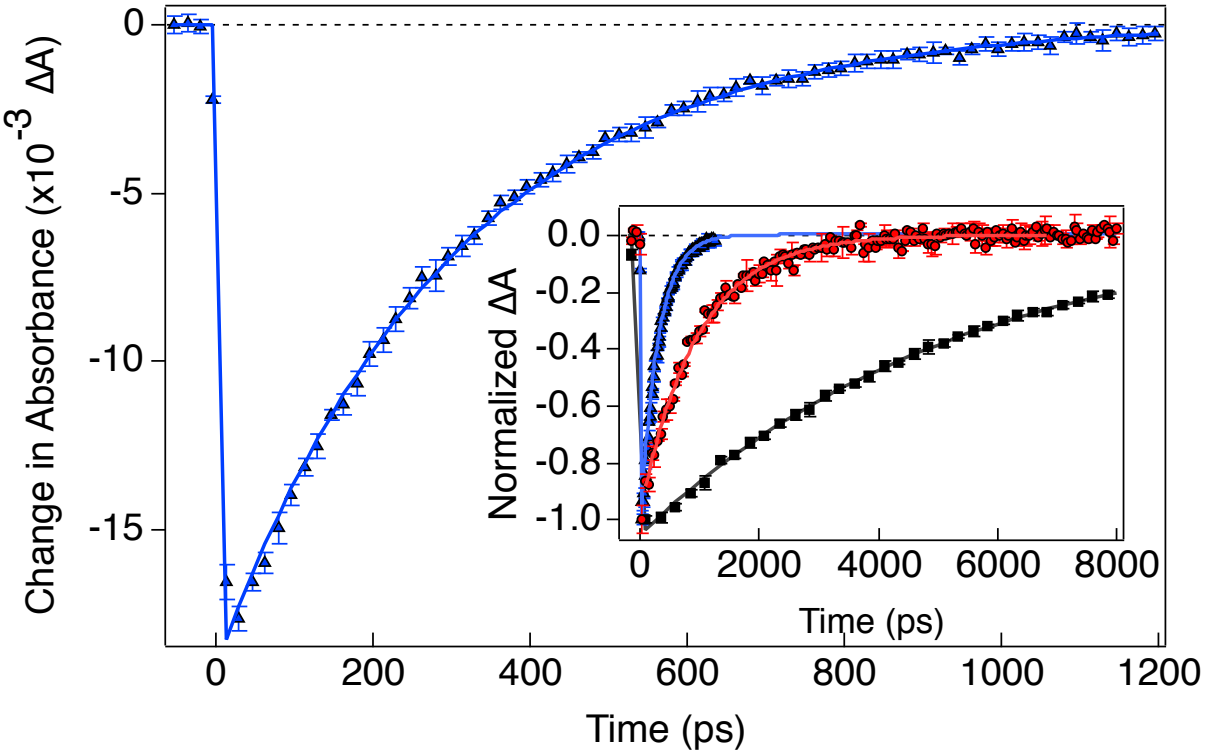

Figure 5-11: Ground state recovery single wavelength transient absorption traces of $[Fe(dkpp)_2]^{2+}$(blue), $[Fe(bpy)_3]^{2+}$(red), and $[Fe(terpy)_2]^{2+}$(black). Solid lines represent single exponential decay fits.

Two explanations could lead to this deviation: either the $^5T_2$ state is the lowest energy excited state and reorganization energy and/or coupling constant is significantly different for this complex than for $[Fe(bpy)_3]^{2+}$ and $[Fe(terpy)_2]^{2+}$ or the $^3T_1$ state has become the lowest energy excited state involved in the relaxation. If the lowest energy excited state is indeed the $^5T_2$, there is no reason to expect a significant change in reorganization energy. The same two metal-based electronic states are involved and the same 10% bond length change is associated with all three complexes. This is verified by geometry optimization calculations and is in the midst of being experimentally measured using femtosecond X-ray spectroscopy.[18,19] With a stronger field, it is reasonable to predict a faster rate for

relaxation if the coupling constant (H_{ab}) is increased, however. The $\Delta S=2$ process to go from a quintet to a singlet requires the influence of a triplet state. The $^3T_1$ state shown in figure 9 facilitates the coupling for this transition. The second-order coupling between the $^5T_2$ and $^1A_1$ states is dependent on the extent to which the two couple with the $^3T_1$, which is, in turn, dependent on the relative energy separations between the two pairs of states. As a stronger field is experienced, the amount of coupling between the $^1A_1$ and $^3T_1$ decreases as the energy separation increases. However, the coupling between the $^5T_2$ and $^3T_1$ increases two times more than the decrease in the $^1A_1/^3T_1$ coupling due to the slopes of the $^5T_2$ and $^3T_1$ lines with respect to the $^1A_1$ ground state. For this reason, it is reasonable to expect an increase in the overall coupling, and by extension, the rate at stronger ligand fields.

If, on the other hand, it is the case that the crossing point has been reached and the $^3T_1$ state is the lowest energy excited state, a decrease in reorganization energy would be expected. The bond length change between $^1A_1$ and $^5T_2$ is 0.2 Å and is expected to be about half of that for the $^3T_1$ due to the difference in orbital population: $(t_{2g})^4(e_g^*)^2$ for the $^5T_2$ is replaced with an orbital population of $(t_{2g})^5(e_g^*)^1$ for the $^3T_1$. Additionally, a $^3T_1$ lowest energy excited state changes the coupling to a first-order process rather than second-order as it is for the quintet to singlet transition. Although both possible scenarios can explain the ground state recovery dynamics observed, a couple of experiments can answer the

question of which excited state is populated: time-resolved X-ray spectroscopy and emission spectroscopy.

Time-resolved X-ray provides structural details of the complex as a function of time. The structure of the $^5T_2$ has a bond length increase of 0.2 Å on a 2.0 Å Fe-N bond. With a decrease in anti-bonding character and increase in bonding character when moving from the $^5T_2$ state to the $^3T_1$ state, the bond length change is expected to be smaller if the $^3T_1$ is the lowest energy excited state.

Emission is the other experiment that can provide strength to the argument that the lowest energy excited state is $^3T_1$. No iron(II) complex is known to emit. This is related to the observation that all low-spin iron(II) complexes have a $^5T_2$ lowest energy excited state. A $\Delta S=2$ spin state change going from the quintet to the singlet eliminates the possibility for a strong enough oscillator strength to radiatively couple the $^5T_2$ excited state to the $^1A_1$ ground state. The $^3T_1 \rightarrow {}^1A_1$ transition is a $\Delta S=1$ process, which can have strong enough radiative coupling to be observed. As previously mentioned, $[Co(CN)_6]^{3+}$complex has a $^3T_1$ lowest energy excited state, and it emits.[13]

Figures 12-14 show emission and excitation profiles for $[Fe(dkpp)_2]^{2+}$. Figure 12 is the corrected and uncorrected (inset) emission profile of $[Fe(dkpp)_2]^{2+}$ with 610 nm excitation. “Correction” of the data is performed to account for the wavelength dependent output of the emission lamp as well as the wavelength dependent detection ability of the detector. Emission was not detectable above 90 K, so measurements were taken at 80 K in

a 9:2 butyronitrile:propionitrile glass. The feature centered at 800 nm is assigned to the ligand field emission from the $^3T_1 \rightarrow {}^1A_1$ transition. The 650 nm feature is thought to originate from a charge transfer emission.

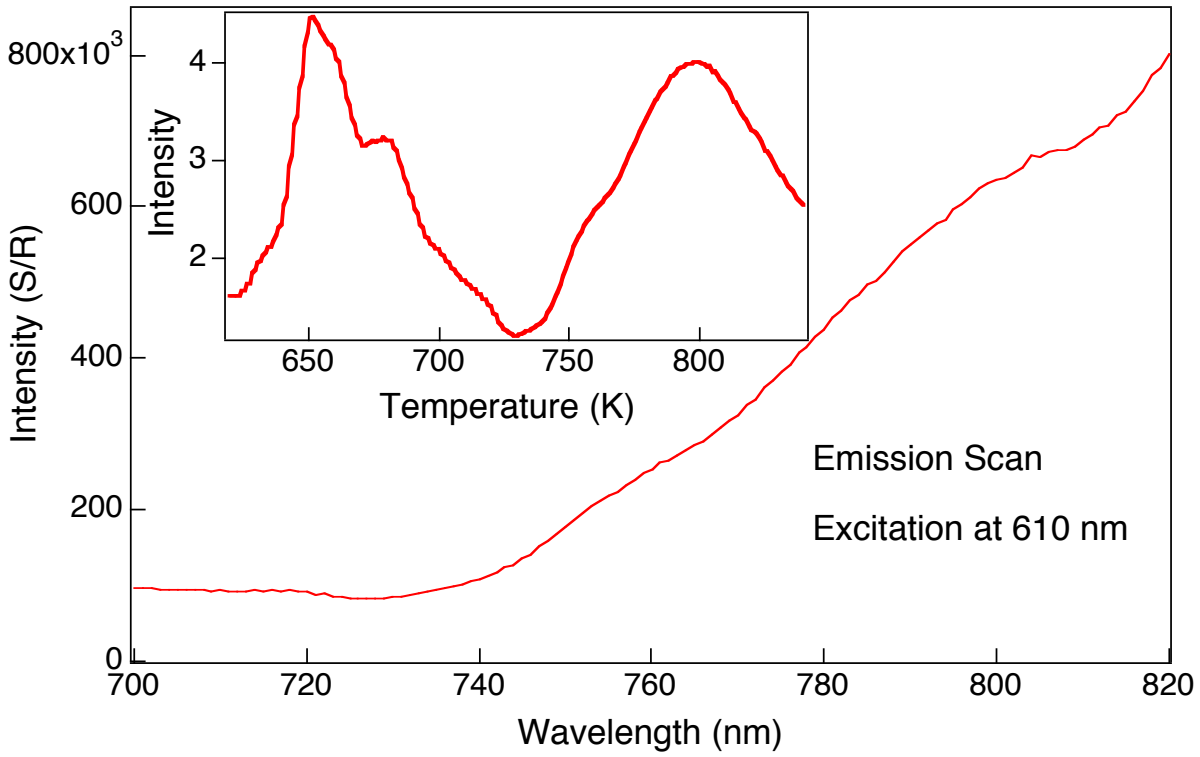

Figure 5-12: Corrected and uncorrected (inset) emission scans upon 610 nm excitation of solution-phase $[Fe(dkpp)_2]^{2+}$ at 80 K. Emission levels are too low for room temperature detection or quantum yield determination.

A substantiating experiment is an excitation scan, which provides information on the absorption features that lead to the emission event. Figure 13 is the excitation scan of the $[Fe(dkpp)_2]^{2+}$ detected at an emission wavelength of 800 nm at 80 K (red) plotted with the ground state electronic absorption spectrum (blue). The overlay of the excitation and absorption features indicates that the same states responsible for ground state absorption result in emissive species. This is a strong argument against the emission coming from an impurity.

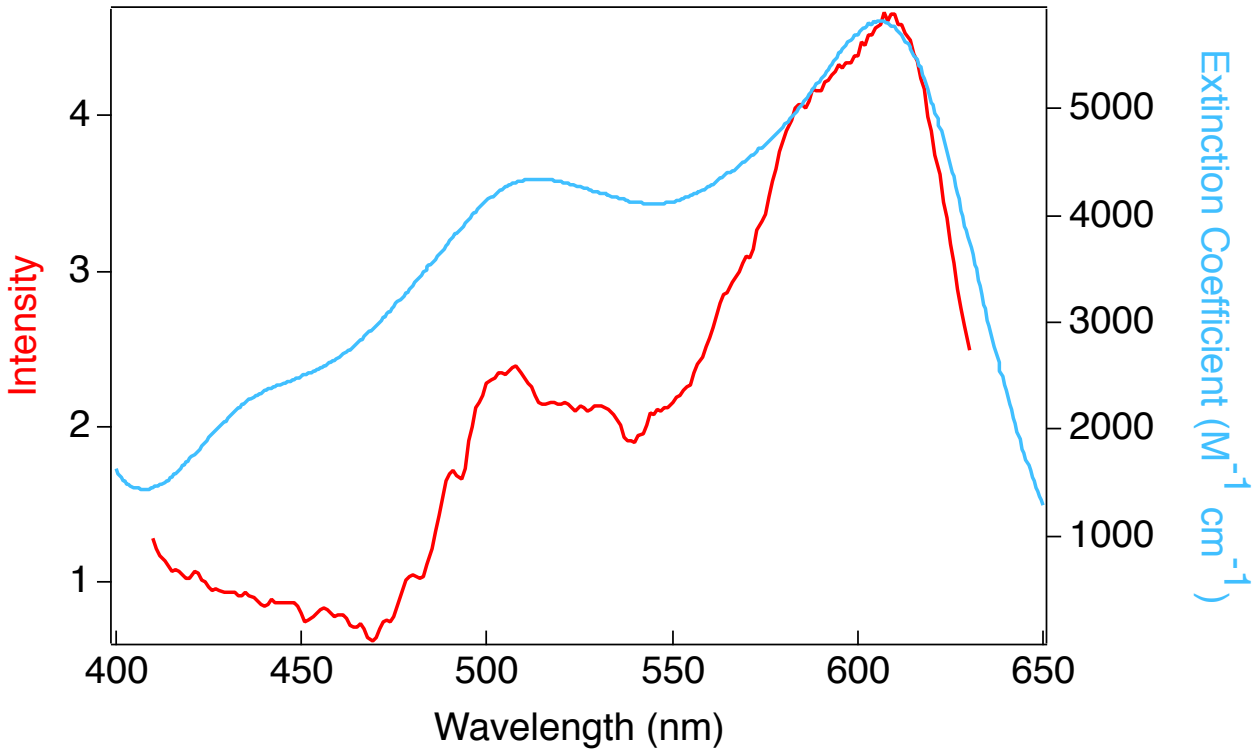

Figure 5-13: Solution-phase excitation scan (red) of $[Fe(dkpp)_2]^{2+}$ at 800 nm emission and 80 K. The absorbance spectrum is overlaid (blue) to compare.

Due to both the low intensity emission as well as the detector cutoff wavelength of 800 nm, these data are inconclusive. Attempts were made to recollect this data with a red sensitive detector, but without success. As a secondary check, crystalline samples were sent to Christian Reber at the Université de Montréal. Emission and excitation traces from that experiment are shown in Figure 14, along with the ground state absorption. Once again, a weak signal was measured and the excitation scan matches up with the absorbance spectrum. The blue shift of the ligand field emission is reasonable due to the solid state sample and colder temperature at which the measurement was collected. The detection of the ligand field emission and disappearance of the charge transfer state emission is consistent with the $^3T_1$ as the lowest energy excited state. Similar behavior in solution as

well as crystal form is another argument against the emission coming from an impurity. Although these results are exciting, they are in the process of being verified and recollected.

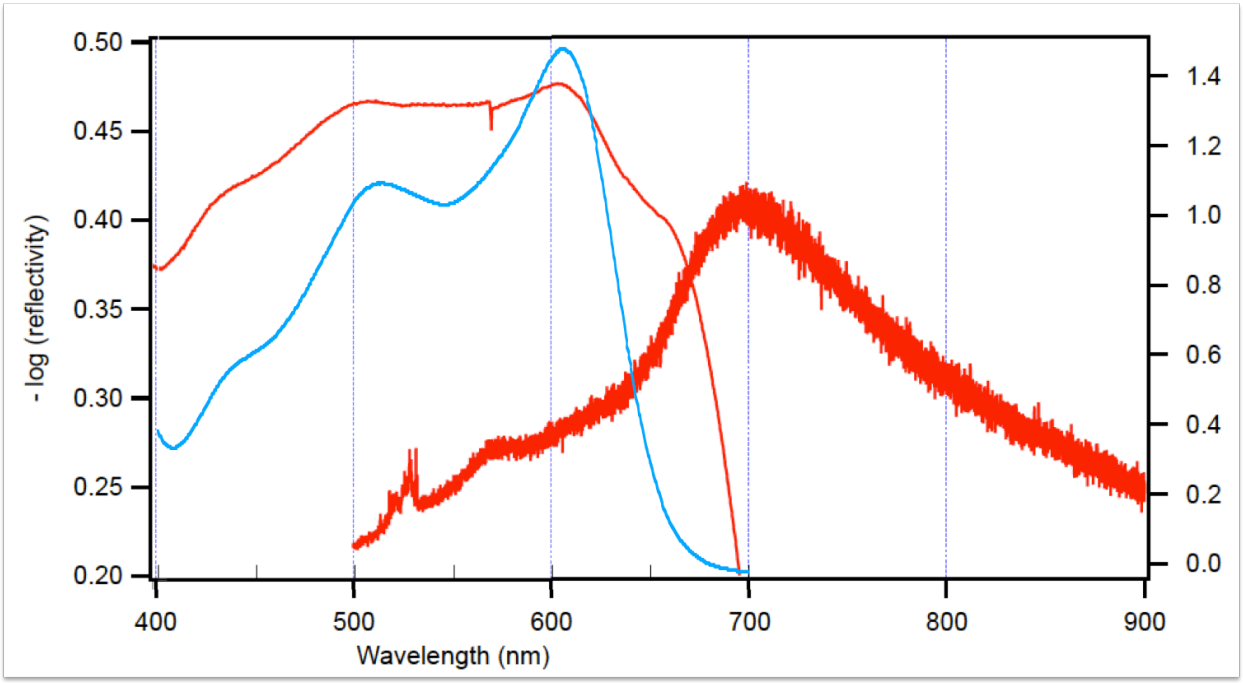

Figure 5-14: Solid-state emission (red, right) and excitation (red, left) scans of $[Fe(dkpp)_2]^{2+}$ measured at 4K. The absorption spectrum is plotted for comparison.

Implications for Solar Energy Conversion:

As discussed in earlier chapters, it is the metal-to-ligand charge transfer (MLCT) excited states that are responsible for the most efficient injection into dye-sensitized solar cells (DSSCs). Although from a basic science perspective, finding the first iron(II) molecule with a $^3T_1$ lowest energy excited state is exciting, it does not make any progress toward replacing Ru^{2+} sensitizers with Fe^{2+} complexes. The charge transfer state lifetime of the $[Fe(dkpp)_2]^{2+}$ was the original goal of making this complex. Figure 15 shows the kinetic trace for $[Fe(dkpp)_2]^{2+}$ in MeCN.

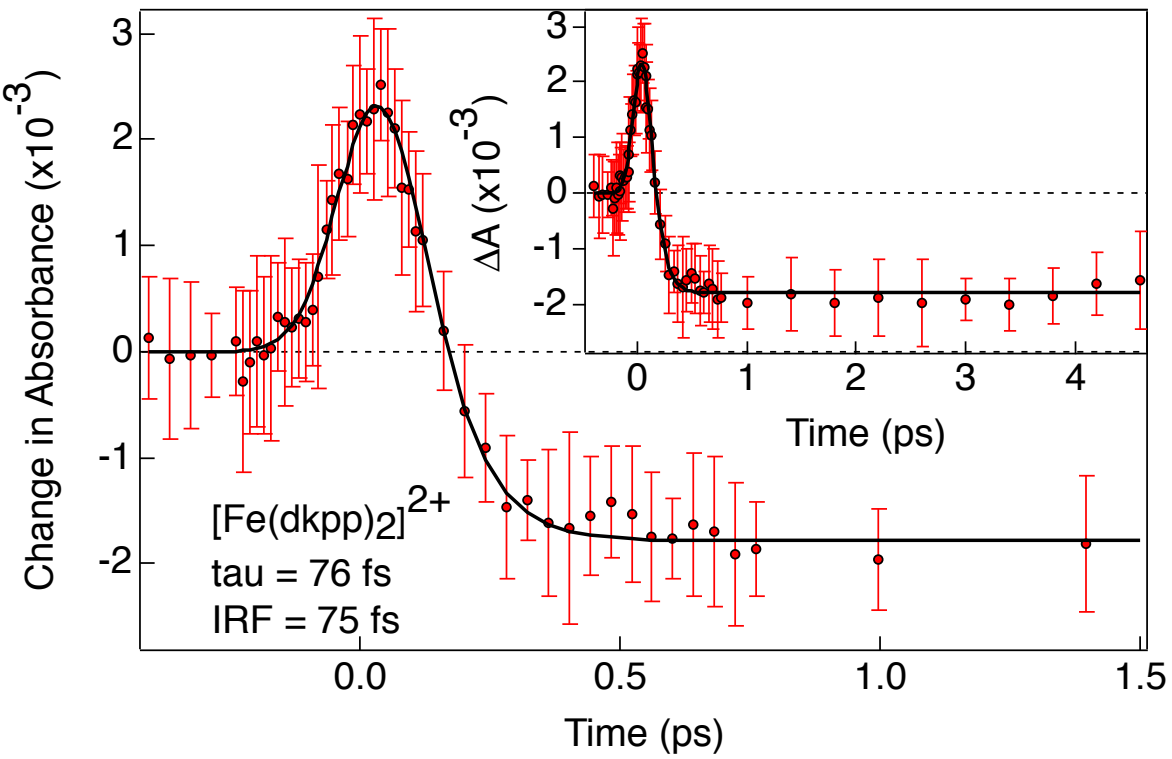

Figure 5-15: Charge transfer to ligand field conversion of $[Fe(dkpp)_2]^{2+}$ in MeCN. The solid black line is the deconvolved fit with a lifetime of 76 ± 15 fs and IRF of 75 fs.

As seen in the terpy series discussed in chapter 3, the signature positive-to-negative transition is an indication that the charge transfer state has been formed and then depleted in favor of the ligand field state.[20] A lifetime of 76 fs was measured for this transition, no longer than the terpy complexes studied previously.

All is not lost, however. Looking back at the molecular orbital diagrams and descriptions of orbital movement, it becomes clear that the ligand field/charge transfer state gap has decreased for this complex compared to $[Fe(terpy)_2]^{2+}$ and $[Fe(bpy)_3]^{2+}$. It is probable that the energetic match of the long-lived ligand field excited state is better and electron injection into either TiO_2 or a slightly positively shifted substrate is possible. Figure 16 shows the energetic matchup of $[Fe(dkpp)_2]^{2+}$ with TiO_2 and Sb_2O_3. Whereas with other

iron(II) complexes the ligand field states were both electronically and energetically incapable of electron injection, the energetic match has improved greatly for $[Fe(dkpp)_2]^{2+}$. Injection may be possible from $[Fe(dkpp)_2]^{2+}$, especially if a substrate with a positively shifted conduction band (such as Sb_2O_3) is used. Although no one is about to start mass producing solar cells with antimony, proof of principle that electron injection is possible from iron(II)-based chromophores would provide much anticipated encouragement to this project.

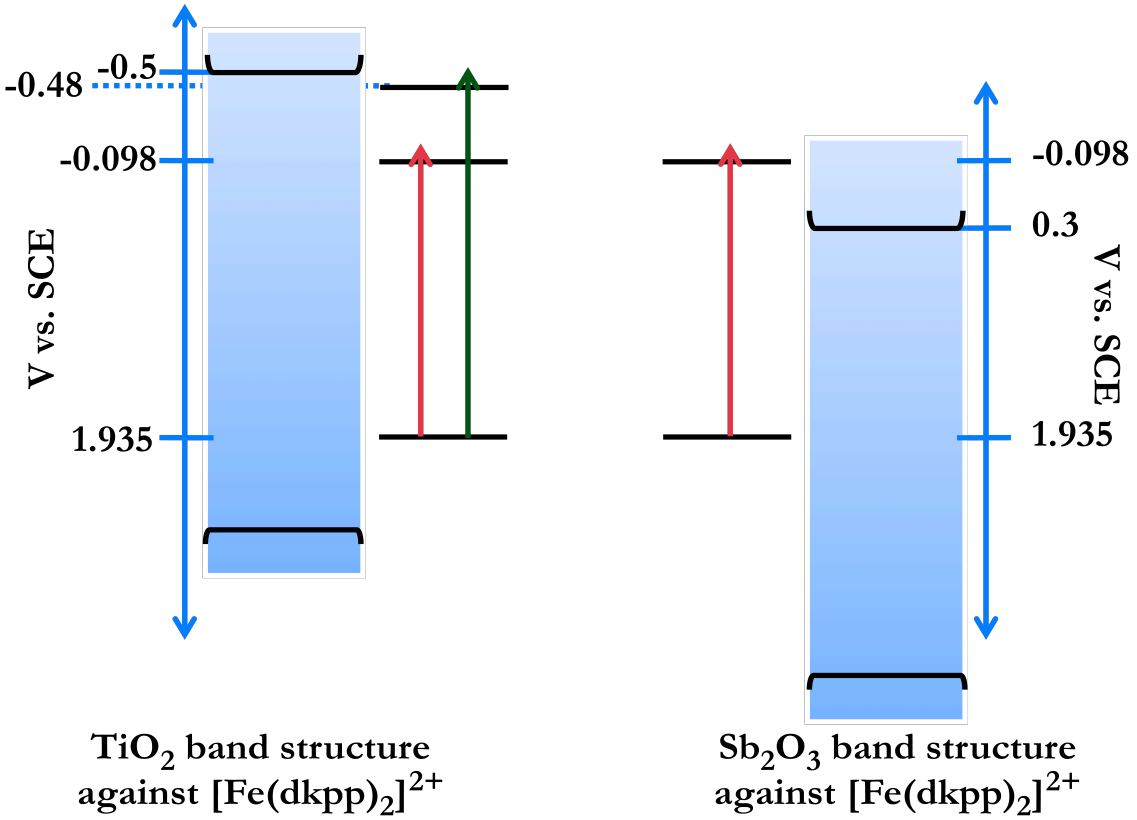

Figure 5-16: Band structure of TiO_2 and Sb_2O_3 compared to the energy level diagram of $[Fe(dkpp)_2]^{2+}$. The comparison is made to illustrate the possible impact this class of complexes may have on solar cell applications.

With a slightly stronger ligand field, inversion of the MLCT and ligand field states may also be possible. Were this to occur, the long-lived state of the iron-based sensitizer would become charge transfer in nature; fulfilling one more expected requirement of "good" sensitizers. Design of new ligand sets with anticipated stronger ligand fields is underway.

From the comparisons discussed in this chapter, the first iron(II) complex with a strong enough ligand field to produce a $^3T_1$ lowest energy excited state has been proposed. It is interesting that this modified polypyridyl ligand has generated a ligand field stronger than that of CN^-. With further understanding of the electronic and geometric factors that have produced such a strong ligand field, a new field of iron(II) chemistry can be opened. Analogous to $[Co(CN)_6]^{3-}$, a new set of chemical and photophysical functions can be expected from this new class of compounds.

REFERENCES

References: Chapter 5

(1) Schramm, F.; Meded, V.; Fliegl, H.; Fink, K.; Fuhr, O.; Qu, Z. R.; Klopper, W.; Finn, S.; Keyes, T. E.; Ruben, M. *Inorganic Chemistry* **2009**, *48*, 5677.

(2) Jamula, L. L. B., A. M.; Guo, D.; McCusker, J. K. *Journal of the American Chemical Society* **2011**, *Submitted for Publication*.

(3) Gawelda, W.; Cannizzo, A.; Pham, V. T.; van Mourik, F.; Bressler, C.; Chergui, M. *Journal of the American Chemical Society* **2007**, *129*, 8199.

(4) Smeigh, A. L., Michigan State University, 2007.

(5) Decurtins, S.; Felix, F.; Ferguson, J.; Gudel, H. U.; Ludi, A. *Journal of the American Chemical Society* **1980**, *102*, 4102.

(6) Tanabe, Y.; Sugano, S. *Journal of the Physical Society of Japan* **1954**, *9*, 766.

(7) Shimura, Y.; Tsuchida, R. *Bulletin of the Chemical Society of Japan* **1955**, *28*, 572.

(8) Monat, J. E.; McCusker, J. K. *Journal of the American Chemical Society* **2000**, *122*, 4092.

(9) Smeigh, A. L.; Creelman, M.; Mathies, R. A.; McCusker, J. K. *Journal of the American Chemical Society* **2008**, *130*, 14105.

(10) Khalil, M.; Marcus, M. A.; Smeigh, A. L.; McCusker, J. K.; Chong, H. H. W.; Schoenlein, R. W. *Journal of Physical Chemistry A* **2006**, *110*, 38.

(11) Gawelda, W.; Pham, V. T.; Benfatto, M.; Zaushitsyn, Y.; Kaiser, M.; Grolimund, D.; Johnson, S. L.; Abela, R.; Hauser, A.; Bressler, C.; Chergui, M. *Physical Review Letters* **2007**, *98*.

(12) McCusker, J. K.; Walda, K. N.; Dunn, R. C.; Simon, J. D.; Magde, D.; Hendrickson, D. N. *Journal of the American Chemical Society* **1993**, *115*, 298.

(13) Miskowski, V. M.; Gray, H. B.; Wilson, R. B.; Solomon, E. I. *Inorganic Chemistry* **1979**, *18*, 1410.

(14) Comparisons are made between the dkpp ligand and terpy, but the same general differences would be seen if compared to bpy, as well.

(15) Sutin, N. *Accounts of Chemical Research* **1982**, *15*, 275.

(16) McCusker, J. K.; Walda, K. N.; Dunn, R. C.; Simon, J. D.; Magde, D.; Hendrickson, D. N. *Journal of the American Chemical Society* **1992**, *114*, 6919.

(17) Creutz, C.; Chou, M.; Netzel, T. L.; Okumura, M.; Sutin, N. *Journal of the American Chemical Society* **1980**, *102*, 1309.

(18) Geometry optimization calculations for both high spin and low spin complexes were performed by Lindsey Jamula.

(19) Nils Huse at the University of California, Berkeley has performed preliminary measurements on the [Fe(dkpp)2]2+ complex and we are awaiting the results. A more thouorough study is planned.

(20) Whether the long-lived excited state of the complex is quintet or triplet in nature, the ground state bleach will still dominate the spectrum. The change in charge transfer state versus ligand field state will still be the dominating difference in the spectra.

Chapter 6: Future Directions

A number of questions were addressed and answered in the course of this research, but as with many good research projects, many more questions came up and plenty were left unanswered. This chapter will spotlight the research I believe to be the most important or interesting to pursue, along with additional experimental techniques that could be incorporated into the spectroscopic arsenal of the lab.

Excitation Energy and Solvent Dependence:

Chapter 5 discusses a complex with nearly perfect octahedral symmetry, $[Fe(dkpp)_2]^{2+}$- where dkpp is 2,6-di(2-ketopyridyl)pyridine, that exhibits unique and encouraging photophysical behavior. The ligand field excited state of this complex decays with a fast rate following rapid charge transfer state deactivation. Along with the measurements discussed in Chapter 5, this relaxation rate was measured as a function of excitation energy. With each pump wavelength, a different absorption band is excited. Figure 1 is a reproduction of the ground state electronic absorption spectrum for $[Fe(dkpp)_2]^{2+}$ with corresponding symbols indicating the different excitation wavelengths for the experiment. The absorption spectrum shows four distinct peaks with extinction coefficients within the range for charge transfer state transitions. Without the d0 analog of the complex from which charge transfer and ligand localized transitions can be assigned, a combination of literature assignments and extinction coefficients are the best way to determine the nature of these transitions.

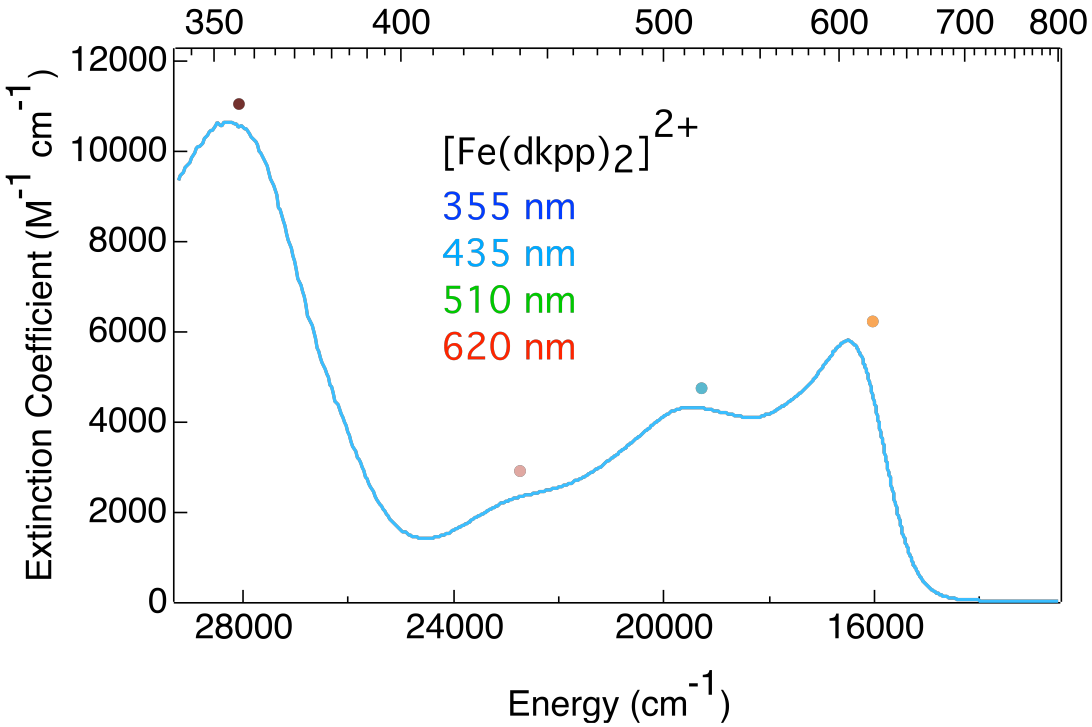

Figure 6-1: Ground state electronic absorption spectrum of $[Fe(dkpp)_2]^{2+}$ in MeCN. Colored markers indicate the excitation wavelengths for the ligand field relaxation kinetic traces shown in Figure 2.

The energies for the three red transitions (435 nm, blue diamond; 510 nm, green circle; 620 nm, red triangle) are in the wavelength region where the metal-to-ligand charge transfer transitions of many iron(II)-polypyridyl complexes appear. Along with the extinction coefficients and previous assignments, these transitions are assigned as MLCT bands. The blue most transition (355 nm, dark blue square) is a bit more ambiguous. The wavelength region is closer to that for ligand localized transitions, but the intensity of the transition is low for $\pi \rightarrow \pi^*$ transitions. Without the d^0 analog, the assignment was unclear.

Transient absorption spectroscopy was performed to determine if decay rates were pump energy dependent. Ground state recovery is shown in Figure 2. Time constants from the red-most and blue-most excitation energies measure within error of each other for

ground state recovery. This is not the case for charge transfer state deactivation, shown in Figure 3. Two observations can be made from the results of Figure 3: first, the behavior from the 355 nm excitation is not similar to that of all other pump wavelengths; second, a variation in long lived transient signal is excitation energy dependent for the three pumps in the MLCT region.

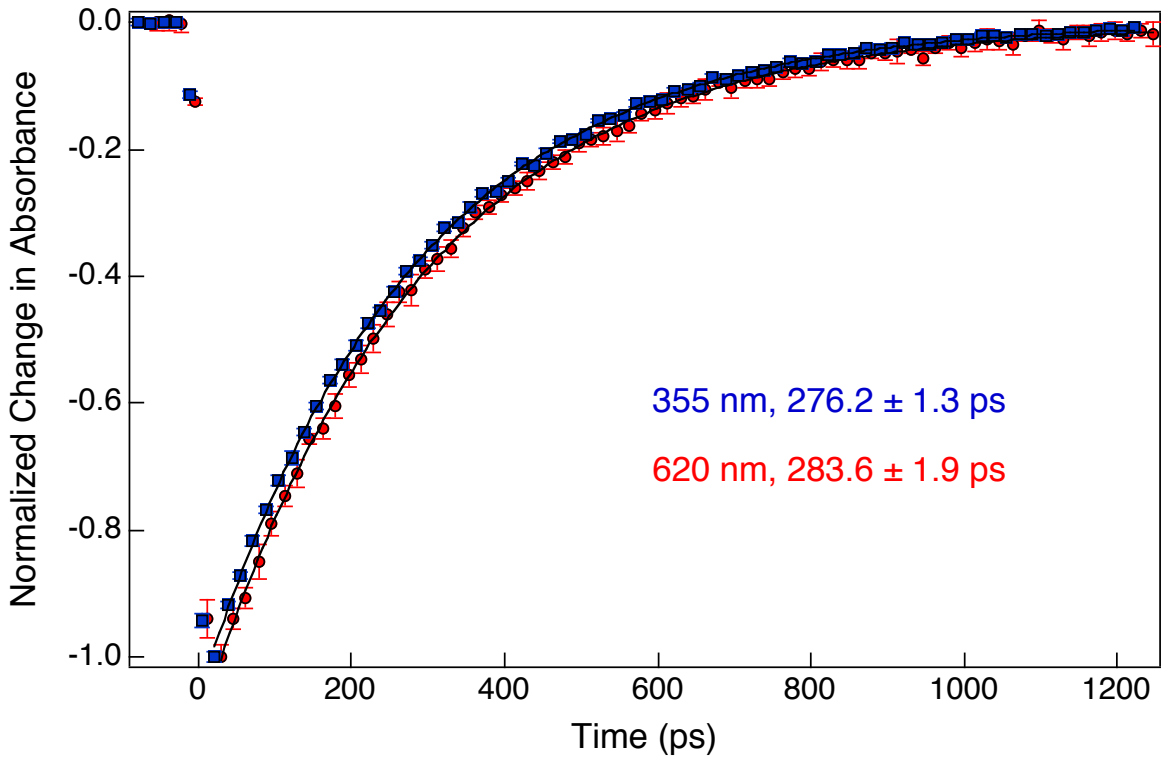

Figure 6-2: Long-lived excited state decay traces of $[Fe(dkpp)_2]^{2+}$ 5with different excitation energies. Both traces were probed in the excited state bleach at 600 nm for 355 nm excitation and 560 nm for 620 nm excitation.

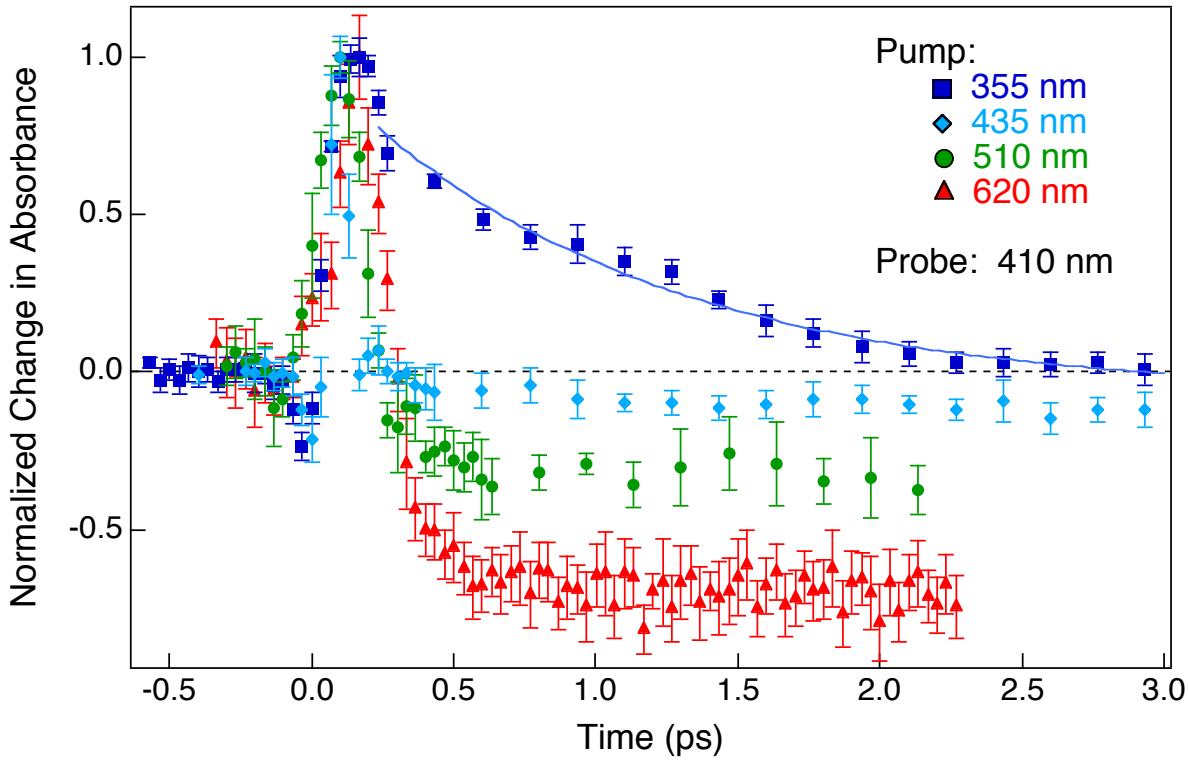

Figure 6-3: Decay traces for $[Fe(dkpp)_2]^{2+}$ within the first 3 ps of excitation with the indicated pump energies. The blue fit line shows a time constant of 1.09 ± 0.06 ps. All traces were probed at 410 nm.

The first observation can be explained by assigning the 355 nm band in the absorbance spectrum as ligand localized. The decrease in extinction coefficient compared to the $\pi \rightarrow \pi^*$ transitions of $[Fe(terpy)_2]^{2+}$ or $[Fe(bpy)_3]^{2+}$ can be due to intensity stealing from other transitions. Additionally, the significant red-shift of this transition can be explained by the increase in conjugation for the dkpp ligand as compared to terpy or bpy. Since the three redder transitions are of one type and the bluest transition is of another, it is not surprising that the time constants (or relaxation pathways) would be different.

The second observation is that the long-lived species after charge transfer excitation varies in intensity with different pump energies. Normalization was performed at t=0. It is more reasonable to think that 100% of the excited molecules populate the initially excited

electronic state than to assume 100% of the excited species end up in the same long-lived state. For this reason, normalization at the peak of the initially excited state around t=0 was deemed accurate for comparisons. It is yet undetermined whether this difference in long-lived excited state signal intensity is due to laser operation or due to a difference in formation yield of the excited state.

Systematically smaller pump powers were used as the excitation wavelength was moved toward the blue. With lower pump intensities, less excited state is expected to be created and a smaller signal indicates this difference in excitation. Counteracting this decrease in pump power is a concurrent decrease in the beam size out of the TOPAS as the wavelength moves blue. These inversely correlated effects can offset each other to keep the pump density constant. A second pump dependent study must be completed where the pump density is kept as constant as possible.

Another explanation could be that the yield for long-lived excited state formation is excitation energy dependent. If higher energy excitation somehow results in less long-lived population than low energy excitation, a smaller offset would be seen at longer times for the blue wavelength pumps. In order to determine this, a pump dependent excited state yield study would have to be performed. Netzel explains a procedure for determining the yield for ligand field excited states using $[Fe(phen)_3]^{2+}$.[1] Although these molecules are similar, the behavior of $[Fe(dkpp)_2]^{2+}$ is different enough from the other iron(II) polypyridyl complexes studied that it cannot be assumed that the relaxation behavior is similar. These pump dependent studies would provide more insight into how the

$[Fe(dkpp)_2]^{2+}$ system works and perhaps the changes that could be made to improve its behavior in the solar cell application.

Another interesting result came in the form of solvent dependent ground state recovery for the ligand field relaxation processes of the iron complexes. Although solvent dependences in many areas of chemistry are known, they are expected mostly for processes that strongly involve the outermost part of the complex. Since ligand field transitions are metal center based, the expectation was that they would not vary with solvent to a large extent.

Solvent dependent behavior was observed for many of the experiments performed on the complexes over the course of the research. Electrochemical potentials, ground state electronic absorption spectra, kinetic behavior, and thermodynamic properties[2] all exhibit solvent dependencies to some extent. Solvent even plays a role in solar cell efficiency.[3] These dependences, however, involved charge transfer states. Charge transfer states move electrons between the metal in the center and the ligand on periphery of the complex and solvent molecules are expected to respond. An extra kinetic component can sometimes be observed in decay traces after charge transfer excitation, indicating a energy dissipation pathway due to the solvent. The solvated complex has a particular charge distribution in its ground state and solvent molecules orient themselves to minimize the energy required to interact with this charge distribution. Movement of electrons from one part of the molecule to the other changes the charge on the ligand and requires a response from the solvent to redistribute its own charges. Charge transfer transitions are expected to incite a solvent

response and the response will vary with solvent type; polarity, size, strength of interaction and other solvent characteristics determine the size of the response.

When a transition does not involve ligands and is, instead, localized on the metal center of the complex, a much smaller solvent response is expected. The charge distribution centers on the middle of the complex where solvent has less interaction and does not change over the course of the transition. As shown in Figures 1 and 2, however, a significant change in ground state recovery rates is seen with various solvents. The trends along the solvent series do not seem to track polarity, dielectric constant, size, or protonation. It is possible that the size or shape of the solvent molecules can effect the amount of interaction possible with the metal center as the ligand field transition takes place. In order to determine the cause of these variations, calculations are underway to determine the size, shape, and orientation of the ligands around the complex in terms of the openings available to solvent molecules.

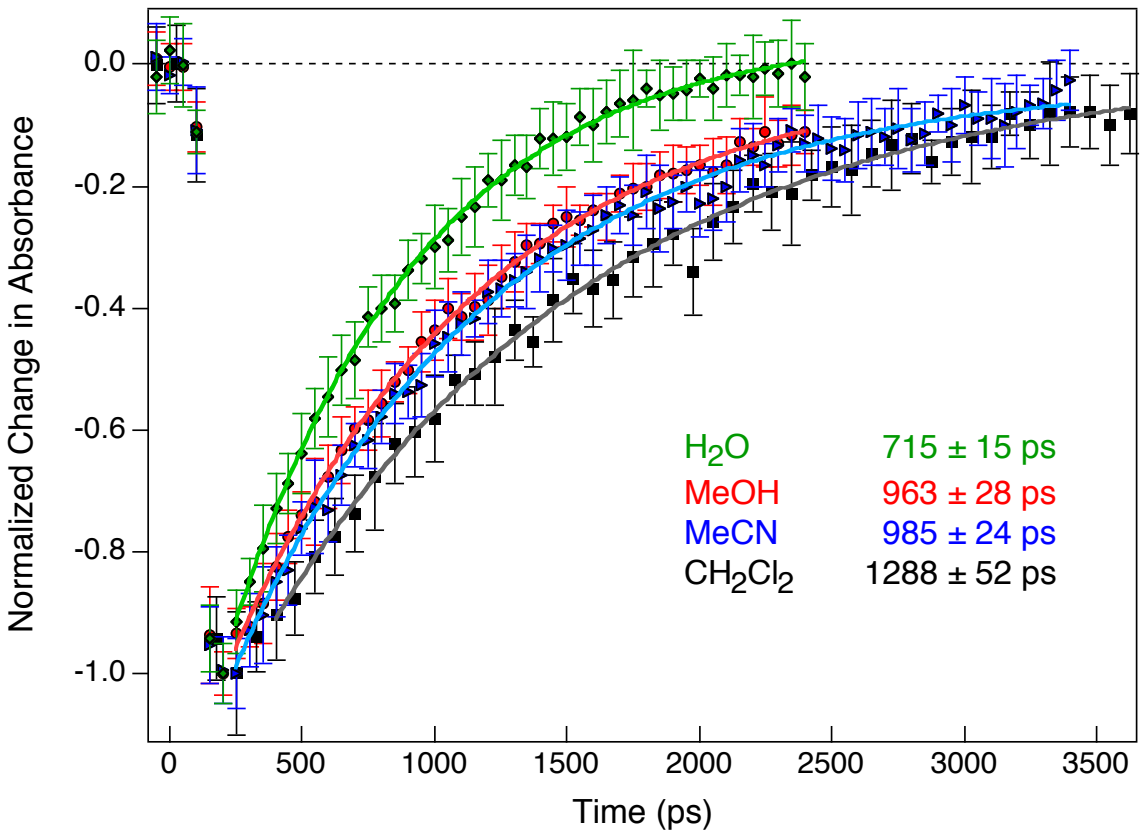

Figure 6-4: Single wavelength decay traces of $[Fe(bpy)_3]^{2+}$ in various solvents.

The variations in lifetime data for different solvents shown in Figure 4 represent a range of dielectric constants, polarity, and contain both protic and aprotic solvents. Lindsey Jamula is performing calculations to determine whether the amount of access to the metal afforded to the solvent from the ligand geometry can be correlated with the rate of relaxation. It is predicted that the more access the solvent has to the metal center, the larger the solvent effect will be seen on the ground state recovery. As seen in Figure 5, the trend is basically the same for $[Fe(terpy)_2]^{2+}$ as it is for $[Fe(bpy)_3]^{2+}$, but the effect is smaller.

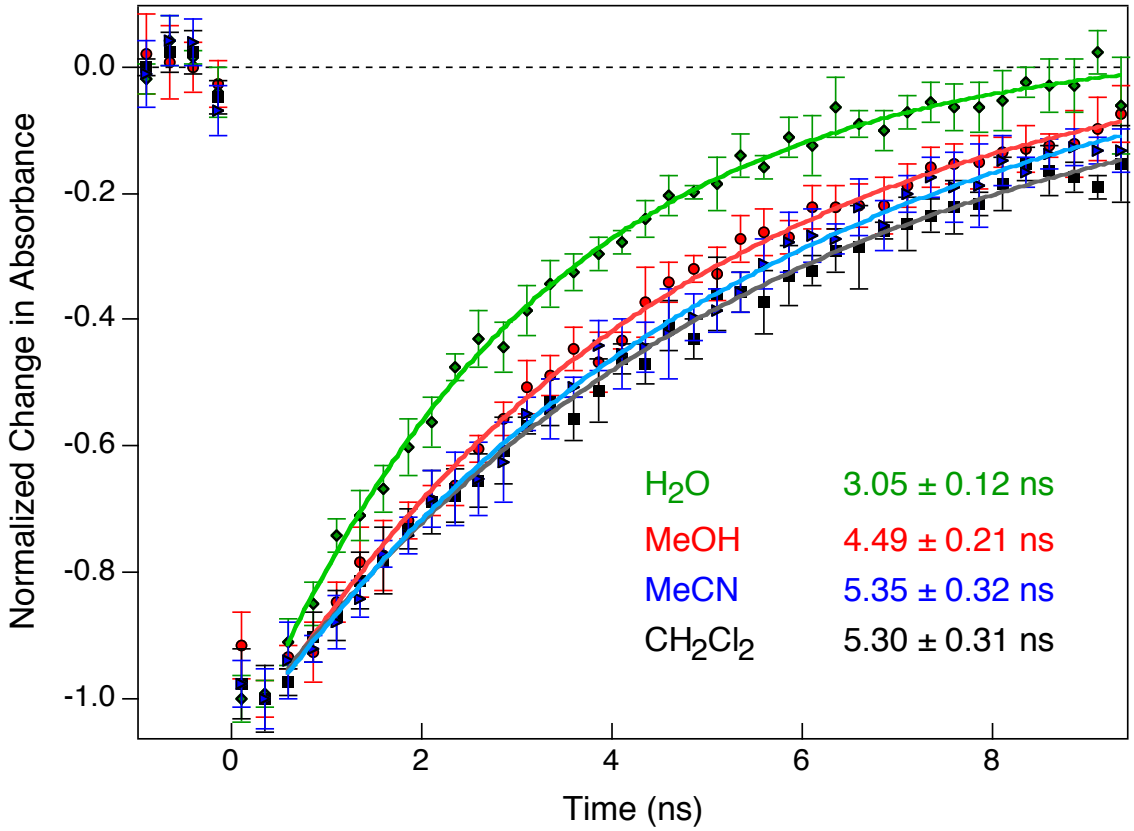

Figure 6-5: Single wavelength decay traces of $[Fe(terpy)_3]^{2+}$ in various solvents.

For now, the empirical observation that the ground state recovery process is solvent dependent is enough to beg the question of whether the charge transfer deactivation process is as well. Reports have been made on solar cell efficiency that is solvent dependent, but no other parameter in the solar cell was changed. Once again, when one component changes, the opportunity to optimize the entire cell opens up. Solvent could play an important role in this process. If it is found that one solvent stabilizes the charge transfer state of an iron (II)-based sensitizer more than another, that solvent will likely give the largest overall efficiency as well.

The data presented here are quite preliminary and must not only be recollected, but also expanded upon. A larger range of molecules with varying steric bulk will provide insight

into whether the effect is sterics-based and calculations can help discern whether it is electronics and energetics based. Either way, capitalizing on the solvent dependency of these processes can only benefit the research. The solvent used for these measurements have been, up to now, kept constant and only varied when solubility or temperature range dictates it. Having a better understanding of how the solvating medium affects the dynamics and efficiencies of the processes can lead to more intelligent design of the systems assembled for testing.

Electron Injection to Optimize Cells:

It was the original goal of this research project to measure the electron injection dynamics of an iron (II) based solar cell. With the observation of a photocurrent from such a cell,[4] electron injection is known to occur. The rate at which injection takes place is an important metric to be able to monitor as the sensitizers/cell parameters are changed. Electron injection dynamics for Fe(2,2'-bipyridine-4,4'-dicarboxilic acid)$_2$(CN)$_2$, the sensitizer that produced a photocurrent from the Ferrere and Gregg report, has been measured before.[5] The rate of injection was determined to be on the timescale of < 100 fs, however very little was mentioned about this finding and no follow-up exists. It is the goal of this research group to build on those initial reports and use the combination of synthetic design, steady state characterization, and electron injection detection to exhaust the possibilities for iron (II) based solar cells.

The first goal will be to reproduce previous results on the well studied N3 complex (Ru(2,2'-bipyridine-4,4'-dicarboxilic acid)$_2$(SCN)$_2$). Preliminary initial results show a reasonably similar rise time for the conduction band electron at 1700 nm, but experimental

procedures are still being fine-tuned. Once the signal for N3 is collected with confidence, the Fe^{2+} analog will be tested in the same cell conditions. This will be complimented by tests on the tris acid version of the sensitizer [Fe(2,2'-bipyridine-4,4'-dicarboxilic acid)$_3$]. The tris acid result will provide information on the relative efficiencies and rates for charge transfer state injection compared to metal to particle charge transfer (MPCT). A number of studies have found injection from $[Fe(CN)_6]^{4-}$ to TiO_2 films. [6-8] These findings, along with an absorption band-dependent photocurrent, suggest a larger efficiency for MPCT than injection from the MLCT state. It is crucial to determine the mechanism for charge injection in these complexes if optimization will occur.

From the results of these studies, optimization of other parameters in the cells can be started. The platinum counter electrode, I_3^-/I^- redox couple, and even TiO_2 semiconductor may not be the optimal materials for the iron (II)-based cell, although they work best for the ruthenium cells. A number of electrolyte compositions with varying redox couples will be crafted into the cells. Along with providing better electronic matches that may improve the open circuit voltages, the removal of I_2 from the electrolyte will decrease the detrimental light absorption that occurs from the dark brown solution.

The optimization, or even the detectable improvement, of an iron-based dye sensitized solar cell has the promise of great returns. Movement away from the rare and expensive ruthenium-based sensitizers is crucial for the mass production of these devices. It also provides new avenues through which improvements in the overall working of the cell can be made. There is no guarantee that the end of this research project will lead to a useful

iron-based solar cell, but the thorough investigation is necessary. Not only is there promise in the findings of previous work, but the lack of optimization in the cells, the fact that so many factors play a role in the individual solar cell's efficiency, and the promising energetics shown in novel iron (II) based complexes add to the excitement and possibilities this research holds.

With the new electron injection detection methods determined for the new system, research on optimization of cells can move forward full throttle. Variations in ligand set, anchoring group, semiconductor substrate, and electrolyte composition are the expected parameters to change and monitor as the cell is optimized. In order to ease the synthetic workload, it was decided that only the best candidates for sensitizers would be derivatized to add the anchoring group. As was shown in chapter 4, the first five complexes synthesized and studied not only failed to show a decrease in charge transfer deactivation rate, but the process got faster. Because more time in this dissertation was spent studying the solution-based fundamental photophysics of these complexes, very little was done on full cells. Currently, sensitizers are being modified to start the process of measuring electron injection as well as full cell parameters.

Additional Experimental Techniques:

Along with the synthetic and fundamental chemistry obstacles to the study of electron injection dynamics was the timescale available in the previous laser setup. As was discussed in chapter 2, a new 35 fs laser system was purchased to supplement the spectroscopic capabilities in the McCusker group. Many previous studies on the topic have measured at least one component of electron injection from ruthenium-based cells into TiO_2 in the <100 fs regime.[9-13] With the goals of optimizing any iron-based cell and

correlating the steady state behavior with electron injection dynamics, time resolution of better than 100 fs is an absolute necessity. Road runner is now operational with the chirp compensation, wavelength tunability, and infrared detection ability necessary for electron injection detection.

Improvement of this detection could also be accomplished by moving the detection capabilities further into the mid-IR. Conduction band electrons have stronger TA signals as the probe decreases in energy.[13] A second benefit comes from fewer broad, indistinguishable signals in the mid-IR to complicate the detection of the electron signal. This detection capability requires the purchase of a MCT array detector from IR Associates and the associated electronics from IR Systems Development along with performing difference frequency generation to reach the mid-IR wavelengths for probing. Plans have been made for adding this technique to the lab and are awaiting funding.

Ultrafast emission experiments are also in the long-term plans of the laser lab. A Time-Correlated Single Photon Counting (TCSPC) system from Ultrafast Systems will provide emission and transient absorption capabilities from ultrafast to microsecond timescales (with the generous supplement of Gary Blanchard's TCSPC system). Ultrafast emission capabilities will provide another detection method for relaxation dynamics of complexes in solution and in cells, making assignments of processes less ambiguous.

The final experimental addition to the ultrafast lab will be variable temperature TA. With the addition of the 13 ns delay line, additional chirp from the dewar setup on the 100 fs system will be negligible compared to the timescale of the interesting processes. The dewar used for the same experiment on the nanosecond timescale will provide reliable temperatures ranging down to 4 K. Difficulties of scatter and pump/probe overlap will

make this experiment anything but trivial, but the ability to collect low temperature transient absorption kinetics will fill in one more gap in the lab's abilities.

The opportunities afforded by the continuation of the synthesis, calculations, and spectroscopy in this area are very promising. With a group of talented scientists motivated to move this project forward, I am very excited to see what can be accomplished. I feel very fortunate to have been a part of this research effort and believe in the possibilities and the people continuing the work.

REFERENCES

References: Chapter 6

(1) Bergkamp, M. A.; Chang, C. K.; Netzel, T. L. *Journal of Physical Chemistry* **1983**, *87*, 4441.

(2) Hoselton, M. A.; Wilson, L. J.; Drago, R. S. *Journal of the American Chemical Society* **1975**, *97*, 1722.

(3) Pollard, J. A.; Zhang, D. S.; Downing, J. A.; Knorr, F. J.; McHale, J. L. *Journal of Physical Chemistry A* **2005**, *109*, 11443.

(4) Ferrere, S.; Gregg, B. A. *Journal of the American Chemical Society* **1998**, *120*, 843.

(5) Asbury, J. B.; Wang, Y. Q.; Hao, E. C.; Ghosh, H. N.; Lian, T. Q. *Research on Chemical Intermediates* **2001**, *27*, 393.

(6) Yang, M.; Thompson, D. W.; Meyer, G. J. *Inorganic Chemistry* **2002**, *41*, 1254.

(7) Yang, M.; Thompson, D. W.; Meyer, G. J. *Inorganic Chemistry* **2000**, *39*, 3738.

(8) Ohta, K.; Maekawa, H.; Tominaga, K. *Chemical Physics Letters* **2004**, *386*, 32.

(9) Gundlach, L.; Ernstorfer, R.; Willig, F. *Progress in Surface Science* **2007**, *82*, 355.

(10) Furube, A.; Murai, M.; Watanabe, S.; Hara, K.; Katoh, R.; Tachiya, M. 2006, p 273.

(11) Duncan, W. R.; Stier, W. M.; Prezhdo, O. V. *Journal of the American Chemical Society* **2005**, *127*, 7941.

(12) Kallioinen, J.; Benko, G.; Myllyperkio, P.; Khriachtchev, L.; Skarman, B.; Wallenberg, R.; Tuomikoski, M.; Korppi-Tommola, J.; Sundstrom, V.; Yartsev, A. P. *Journal of Physical Chemistry B* **2004**, *108*, 6365.

(13) Anderson, N. A.; Lian, T. *Coordination Chemistry Reviews* **2004**, *248*, 1231.

APPENDICES

APPENDEX A: Single-wavelength Femtosecond Transient Absorption Data Workup

In order to process the raw data collected from the TA experiment performed on Road Runner or Wile E, a LabView program entitled "UFWorkup.vi" is used. Figure 1 is the screen shot for the LabView program upon opening.

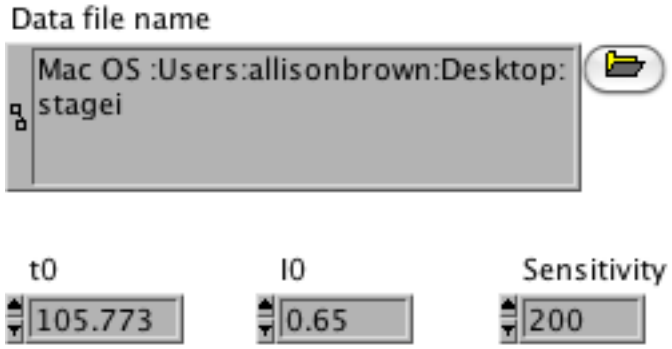

Figure A-1: Front panel for "UFworkup.vi" program for LabView.

- Enter the location of the file intended for workup in the "Data file name" box. Click on the folder icon to locate the file from the computer. Note: when a scan has completed, two files will be written. One will be the file name chosen at the start of the experiment and the other will have a "t" appended to it. The "t" stands for "transposed" and is the file that can easily be graphed when opened in a program such as excel, origin, or igor. However, data workup must be completed on the file without the appended "t".
- The t0 box should contain the stage position (in time) that corresponds to the $\Delta t=0$ for the sample collected. Remember that this is pump and probe wavelength dependent and should be established using a two-photon absorber such as the solvent or another standard molecule.

- The I0 box contains the voltage (in Volts) reading taken from the sample photodiode when the molecule is at negative time.
- The sensitivity setting for the scan to be worked up should be typed into the sensitivity box.
- Press the white arrow at the top of the program and a new, worked-up file will appear in the same folder the original file came from. This new, worked-up file will be named with the original file name and appended with a “wu”, indicating it is now “worked up”.

APPENDIX B: Saving Data Manipulated Files for Work Up or Deconvolution

When a baseline offset must be applied to a data set that must then be used in a subsequent Labview program, the corrected file must be saved in such a way to assure the LabView program can read it. To do this, open the file in an excel spreadsheet and do the desired data manipulation (baseline correction, normalization, etc.). When ready to save the file, make sure only the three columns of data are present (time, DA, error) without any titles (only the numbers). Go to "Save As" and indicate the "Format" for saving to be "Tab Deliminated Text (.txt)". Before saving, erase the ".txt" in the file name. Press "save". The file should now be in a format ready for further workup in LabView.

APPENDIX C: Full Spectra Workup in IgorPro (Courtesy of Amanda Smeigh)

In order to present full spectra transient absorption data without the temporal/spectral chirp artifact discussed in Chapter 2, a correction must be performed on the data. The following list of commands and explanations was created by Amanda Smeigh and is made for use in the IgorPro program. Two sets of procedures are presented. Solvent scans must be used as the base for the correction of the sample. Data must contain constant time intervals for accurate chirp correction.

**********START OF SOLVENT CORRECTION**********

//For MSU Data Files

I have included command lines here that you can copy and paste into IGOR all you will need to do is change the names to correspond to what you want to call the files. The // indicates comments that I have made, these are to help you not to be pasted into the command line!

loadSpectrum("","", "ACN")

//to load a file into a Matrix, which you use a Dialogue to choose and is then named ACN. *The "" is an open quote (") and a closed quote (") right next to each other. The last entry is what you want to name the matrix in this case I named it ACN since it is a solvent scan. It needs to be in quotes!*

SetScale/I x 315.015,611.909,"", ACN; SetScale/I y -0.134,1.5,"", ACN

//Change scaling of waves to do chirp correction THIS IS ESSENTIAL x is Wavelength (Start, Stop) y is the time range (Start, Stop). So your command line will be: *SetScale/I x*

StartValueXaxis, StopValueXaxis, “”,<nameofmarix>; SetScale/I y StartValueYaxis, StopValueYaxis,””,<nameofmaritx>

DTSpectrum(ACN, "aACN")

//This command copies and transposes the matrix ACN. This will give you a matrix to which you apply the chirp correction. It will create a matrix aACN and this is the one that you will use to get the chirp corrected spectrum of the solvent.

ShowInfo

//Brings up cursor box, drag a cursor to the point that you want to determine wavelength and t0. There is also a key stroke to get the information box to show up (Crtl + I)*You might have to click the small arrows on the right of the middle to view the x and y values*

edit

//opens and empty table you can type in the wavelength and t0 values from the image plot. *Be sure to SetScales properly before you do this!*

Display wave1 vs wave0

//Where wave1 is the wave with t0 values and wave0 are the corresponding wavelength values

CurveFit poly 4, wave1 /X=wave0 /D

//Fits wave1 to a 4-order polynomial with wave0 as the x values. The coefficients from the

fit are displayed in the History. *These coeff. are used in the Chirp(..) procedure*

****Chirp correction can ONLY be done on data that is a constant time spacing!!****

DupSpectrum(aACN, "caACN")

//Makes a copy of the aACN matrix to hold corrected spectra hence 'c' and displays the image. You can name it whatever you like. Making a duplicate is necessary because you have to use the aACN matrix as a variable in the chirp correction process.

caACN=aACN(x+Chirp(K0, K1, K2, K3, y))(y)

//Enter the coeffs from the fit for the corresponding Ks in the above command

//ie caACN=aACN(x+chirp(-5.9826, 0.027649, -3.799e-05, 1.75e-08, y))(y)

//where

K0 = -5.9826 ± 2.73

K1 = 0.027649 ± 0.017

K2 = -3.7992e-05 ± 3.48e-05

K3 = 1.7568e-08 ± 2.35e-08

//caACN should be corrected now, check the image to be sure that it is corrected properly!

These coefficients and equation should be used to correct the Sample spectrum.

****//From here you can import the truncated constant step distance data from your sample. Follow the ChirpCorr-Part2-Sample file for details//****

**********END OF SOLVENT CORRECTION**********

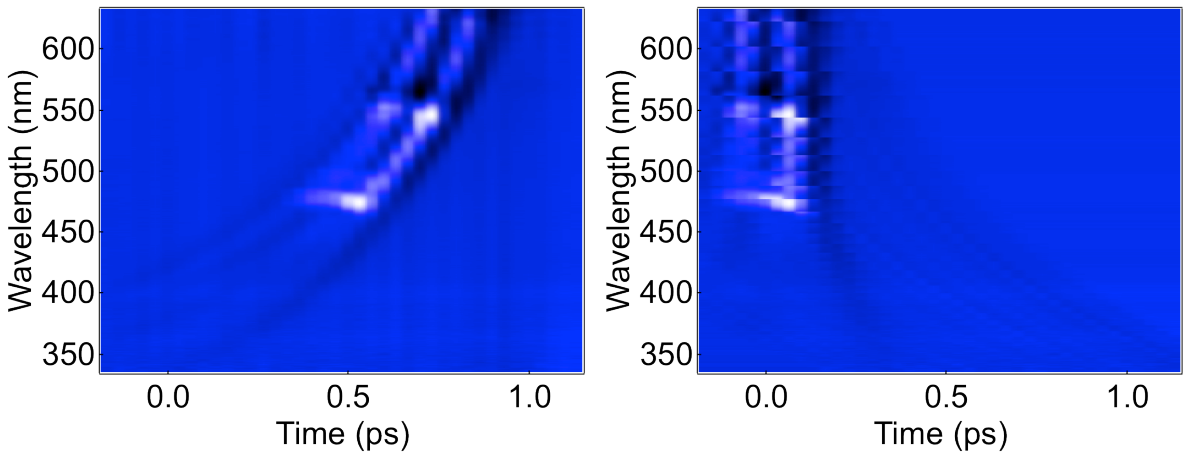

Figure C-1: Solvent signal for chirp correction before (left) and after (right) the chirp correction has been applied to the spectra.

**********START OF SAMPLE CORRECTION**********

Chirp correction can ONLY be done on data that has a constant time spacing!

//This means that you may have to truncate the input data. There are a few way to do this!

//Open the avg file in Excel and generate a separate .txt file with Wavelength, Time and DA of evenly spaced data

This file can then be imported with the LoadSpectrum command!

loadSpectrum("","", "FeBpy")

//Loads a file into a matrix, which you use a Dialoge to choose the file you want to load and is then named FeBpy

SetScale/I x 315.015,611.909,"", FeBpy; SetScale/I y -0.134,1.5,"", FeBpy

//Change scaling of waves to do chirp correction THIS IS ESSENTIAL

DTSpectrum(FeBpy, "aFeBpy")

//This command allows you to copy and transpose the matrix that you want to apply the chirp correction to, it will create a matrix aFeBpy with the x and y values transposed placeing time as you x axis and wavelength as your yaxis. You should check that the scaling is reasonable if you need to adjust the scaling. This done in 'Data' and 'Change wave scaling…'. *you will want to be SURE that you select the correct matrix to the right before you apply the new scaling*

****If you want to correct for a baseline issue, ie Scatter, I_o issues, you need to do the following procedure**

If you don't need to correct for scatter or baseline issues skip to the next (**) **

//Select DA data from the aFeBpy Matrix and copy it to the "Clipboard".

Click first Data cell hold shift down and then scroll to last cell in the last column and click, all the data should be highlighted. ***This is how you copy thing in general!*

Then copy this Data. (ctrl + C : PC) (apple + C : Mac)

LoadWave/J/D/A=aFeBpySW/E=1/K=0 "Clipboard"

//Now from the 'Data ' menu 'Load Waves' [the keystroke is Ctrl+L (PC) (and apple+L (Mac))]

//Make sure that "Make Table", "Load from Clipboard", "AutoName & Go", are checked and "Read Wave names" is NOT checked. Specify a name in the box below "AutoName & Go".

//If you use the command above and specify the “basename” you want for your waves where I have “aFeBpySW” it should work! *You will get a table with waves that correspond to a wavelength vs time.*

LoadWave/J/D/A=tFeBpy/K=0 "Clipboard"

//Select the time points from the First column of the full matrix and Load them into a wave, this can be done in a similar manner as above, by copying th time values (Ctrl+C). I have named the file “tFeBpy” but you can name it anything that is unique that you will recognize. *I usually don't put these into a table though.*

BaselineAdj("aFebpySW", 0, 3, 495)

//This allows you to correct for Scatter or negative times signals that make negative times DA values not equal to 0*. Residual emission from long lived species, or scatter can be corrected for with this command.*

//*Explanation of command* BaselineAdj("<basename of waves from above>", start point of neg.time(cell 0), stop point of neg.time (cell 3), number of waves). <number of waves> (the last number in the command) is the number of waves generated from pasting from Clipboard (usually less than 512) this usually 1+ the number appended to the last wave in the table ie 495 for the aFeBpySW series or the total number of bins you used on array. *There will be pause while this command is working and the command window/history will say “Silent”*

//To check this correction you can plot a kinetic trace before and after correction.

To do this enter:

Display aFeBpy[][309]; Appendtograph aFeBpySW309 vs tFeBpy0

//The time in aFeBpy[][309] is set when you Changed Scaling, so you need to use the time wave you created above for the aFeBpySW309 wave.

DupSpectrum(aFeBpy, "caFeBpy")

//This duplicates the aFeBpy matrix and provides a place to paste the baseline corrected data. Copy the data from the aFeBpySW Table and paste it into the caFeBpy matrix. *You can copy from the table you made from loading the SW waves in the same way you copied from the matrix…select the first cell in the first column and then scroll to the last cell in the last column, hold "shift" and click the cell.*

//Once you have the data selected and copied from the aFeBpySW table select the corresponding **DA data only** in the caFebpy matrix and paste in the aFeBpySW data you just copied

Now that you have done a baseline correction use caFeBpy for the Chirp Correction below ie Go to the command below ^^

****IF you didn't do a base line correction start here!**

//Using a copy of the original data, in the duplicated matrix "caFeBpy" you will generate below, you can do the chirp correction. This way you can always go back to the original

data.

DupSpectrum(aFeBpy,"caFeBpy")

//This duplicates your original data and scaling changes and makes a matrix you can use as the variable in the chirp correction process.

^^

DupSpectrum(caFeBpy,"FeBpycc")

//This command makes the marix that you will use to store the chirp corrected spectrum.

Be sure you have worked up your solvent data in 1) the same experiment OR 2) you have saved the coefs from the polynomial fit from the solvent. Using the Ks from the polynomial fit you will correct the matrix caFeBpy and store it in Febpycc

FeBpycc=caFeBpy(x+Chirp(K0, K1, K2, K3, y))(y)

//Enter the coeffs from the fit for the corresponding Ks in the above command, the ones you obtained from the solvent fit. ie FeBpycc=caFeBpy(x+chirp(-5.9826, 0.027649, -3.799e-05, 1.75e-08, y))(y)

//where

K0 = -5.9826 ± 2.73

K1 = 0.027649 ± 0.017

K2 = -3.7992e-05 ± 3.48e-05

K3 = 1.7568e-08 ± 2.35e-08

//FeBpycc should be corrected now!

DTSpectrum(FeBpycc, "csFeBpy")

//Duplicates the FeBpycc matrix and names it csFeBpy and then transposes csFeBpy so that wavelength is now a column

Now to plot spectra you need to make spectral waves!

First copy the wavelengths from the the csFeBpy table (or what ever you have named it!)

LoadWave/J/D/A=wFeBpy/K=0 "Clipboard"

//Loads the copied wavelengths from csFeBpy matrix (from above) and pastes them into an additional wave. This is done by pasting from "Clipboard" as you did above (a while ago). *You can substitute your chosenwave name in the above command, if you have copied the values from the matrix, and just paste the command into the command window and enter.*

//This will name the wave wFeBpy0 and it contains the wavelength information needed for displaying the spectra

Now you want to load the DA data in its spectral form, the data values in the csFeBpy matrix, copy the data only by selecting it with the shift key as you have done before.

LoadWave/J/D/A=csFeBpyFS/K=0 "Clipboard"

//This command loads the copied data from the “clipboard” that you copied from the csFeBpy matrix and loads it into a series of waves with the basename "csFeBpyFS"

The waves will be csFeBpyFS0 thru csFeBpyFSXX where XX is the number of colums in csFeBpy, it should be equal to the number of time points in the scan (this will change based on how many time steps you took. ALL DATA THAT IS TO BE CHIRP CORRECTED SHOULD BE COLLECTED IN A CONSTANT TIME SPACING: SAME DENSITY OF POINTS!

plotSpectra("csFeBpyFS", wFeBpy0, 140)

//Description of command: plotSpectra(<"base name of files to plot">, <wavelength wave>, <number of time points of number of waves with base name "csFeBpyFS">)

//Plotting the Spectra with plotSpectra will generate a plot of ALL of the spectra with the csFeBpyFS basename. Be sure that you have wFeBpy0 and that you know how many csFeBpyFS waves there are present. This will also colorize the traces.

From here you can display a chirp corrected spectrum at a specific point in time:

Display csFebpyFS0, csFebpyFS7, csFebpyFS13, csFebpyFS19, csFebpyFS25, csFebpyFS37, csFebpyFS67 vs wFeBpy0

//Being the 0th, 7th,13th,19th,25th, 37th, 67th wave with the base name csFeBpyFS vs wavelength (wFeBpy0) . To determine the corresponding time values look at the caFeBpy matrix. *The number of the wave in csFeBpyFS# table corresponds to the row number in caFeBpy the first column will give you the time value of that spectrum. Ie csFeBPyFS0 is the first time point most that corresponds to -5.1ps for instance and csFeBPyFS7 corresponds to the 7th time point which could be 0 ps for instance.*

//To display Chirp corrected kinetic traces a little more work is needed to accurately determine the wavelength

//There are two ways to do display kinetic traces:

1)

Display Febpycc[][70], Febpycc[][130], Febpycc[][190], Febpycc[][250], Febpycc[][370], Febpycc[][490]

//Which displays the 70th, 130th, 190th, 250th, 370th, 490th columns, which are 357.08 nm, 393.145 nm, 429.205 nm, 465.26 nm, 537.385 nm, 609.505 nm (check the row assignment in a matrix that has a wavelength column!)

2)

//Copy from FeBpycc the data cells and Load Waves from "Clipboard" (make a table) into a series of waves that has the basename ccFeBpySW or something. Then you can display them vs tFeBpy0 and the # at the end of the ccFeBpy waves will correspond to a wavelength in the row of FeBpy This is the way I would do it!

**********END OF SAMPLE CORRECTION**********

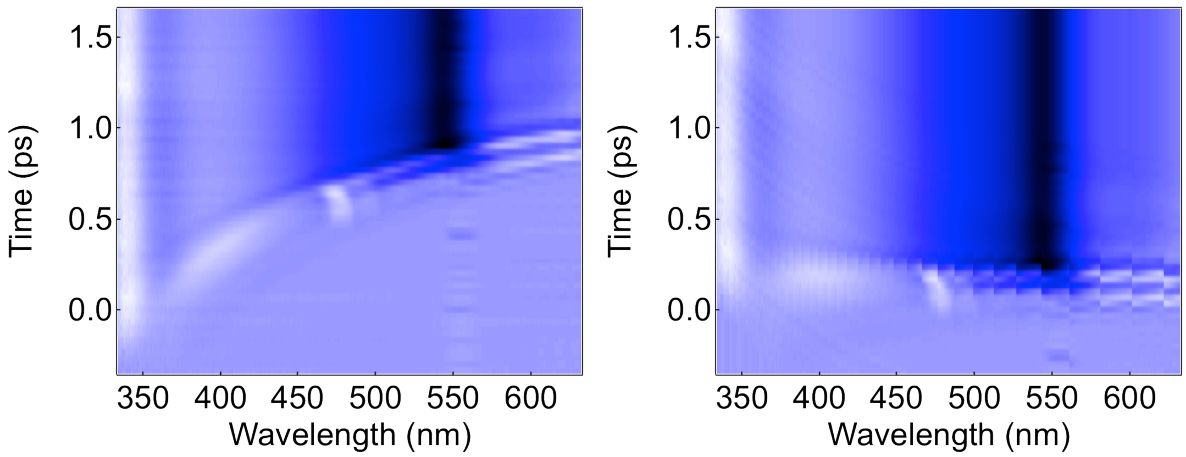

Figure C-2: Sample signal for chirp correction before (left) and after (right) the chirp correction has been applied to the spectra. Correction is based on solvent signal.

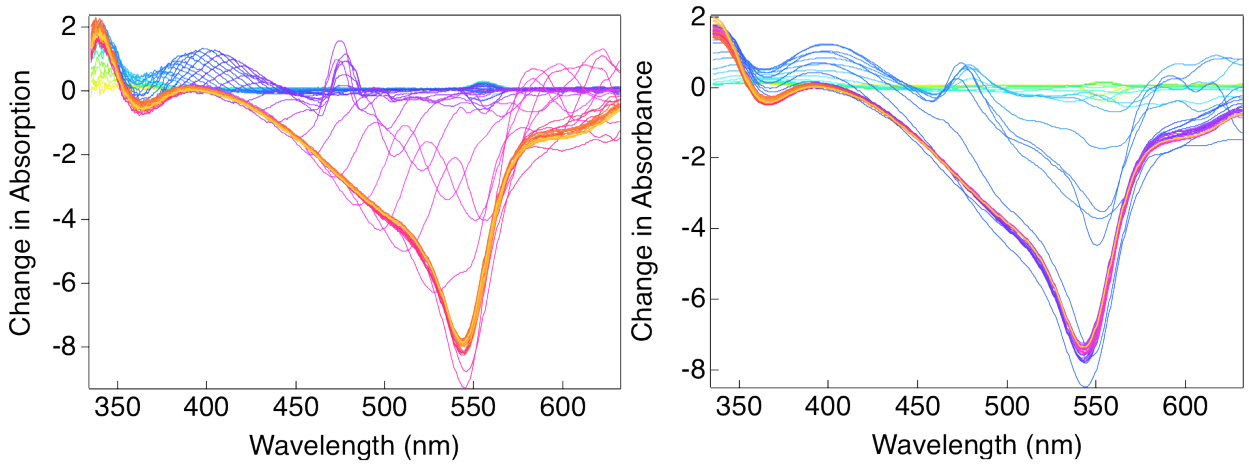

Figure C-3: Full spectra data graphed before (top) and after (bottom) chirp correction.

APPENDIX D: Iterative Reconvolution

The instrument response function (IRF) listed in this document corresponds to the timescale detected when and instantaneous signal is input into the spectrometer. When a longer-than instantaneous but shorter than IRF signal is input, the timescale for the kinetic process can often be determined graphically. The LabView program named "Decon 3 Exp VTI Master.vi" can be used to convolve a kinetic model with a curve corresponding to the pulse width and shape. By iterative reconvolution, the rise of the data can be fit along with the decay. This method allows for determination of time constants down to <25% of the measured IRF.

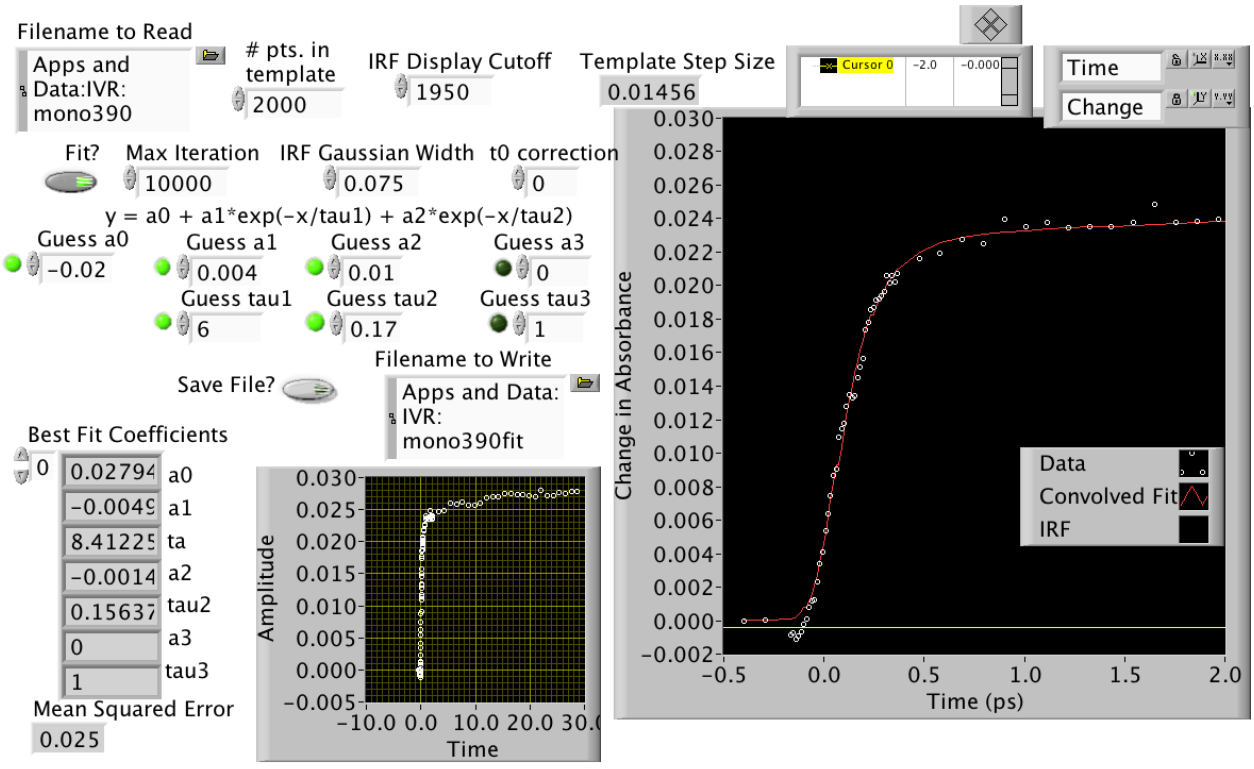

Figure D-1: Front panel for the "Decon3 Exp VTI Master.vi" LabView Program.

- Any timescale can be deconvolved. Be sure data is in the correct form: 3 columns without headings – time data, DA data, error.
- Use the folder button next to the "Filename to Read" box to find the file to be deconvolved.
- With the "Fit?" button turned off, press the white arrow to run the program. This will show the data in the smaller graph to the bottom left without performing any fit.
- The IRF for the spectrometer used (in the same units as the time values for the data) can be placed in the "IRF Gaussian Width" box.
- Values for "# of points in template", "Display Cutoff", "Template step size", and "Max Iteration" are preprogrammed and have little effect on the data. These determine resolution of the fit and can be kept the same as when the programmed was opened. It can often be educational to play with values to determine how they work, however, these have no direct change on the functions used in the fit.
- The number of aX values that are variable (green light on) and non-zero indicates the number of exponentials expected in the fit. If a single exponential is expected, turn off lights for "Guess a2" and "Guess a3" and change their values to zero. Otherwise turn the lights on. The value for a0 is the long time offset – the ΔA value at long time.
- Initial guesses assist in speed and accuracy for fitting completion. Approximate timescales can be put into the "Guess tauX" boxes. The closer these are to correct, the faster the fit will be found. Once again, the green lights must be turned on to allow the values to be variables or turned off to make them constant.

- The “t0 correction” will allow a horizontal shift of the fit with respect to the data. This corrects for slight errors in t0 calculation (which has no bearing on the correctness of the data, but can have a huge impact on the correctness of the fit).
- Once initial guesses are input, run the program by pressing the white arrow.
- The large graph on the right will show two sets of data: one is the original data from the input file, the other is the data associated with the calculated fit. Coefficients corresponding to the fit show up in the “Best fit Coefficients” table on the left.
- Often this process can be done one time and the correct fit is found. More times than not, however, the first “fit” is a starting point for optimization. Varying the starting guesses, the combination of variables allowed to float and kept constant, the t0 correction, and even IRF can change the fit. A little bit of manual variation of some of these variables allows for an understanding of the error associated with the tau values. This assists in the reporting of timescales with error. Fits can be measured as “good” by eye and by the “Mean Squared Error”. Since this is a technique used to assure fast time constants are correct, be sure to zoom in on the early time to assure good match in the rise of the signal. Then, once there is good correlation between the data and the fit at early time, zoom back out to make sure the long time fit matches as well.
- Once the fit that most closely matches the data is found, press the “Save File?” button so it is lit up. Place the destination of the saved file in the “Filename to Write” box and press the white arrow. The new file will have the three columns of the original file with two extras: the data for the fit and the list of coefficients associated with the fit.

APPENDIX E: Contour Plots for Fitting to the Marcus Equation

An Igor program was written and provided by John Weeks from Wavemetrics support. As an .ipf file, this file allows the error for each set of fitting parameters to be plotted. In this file, the variables hab and λ are varied within specified ranges and at specified spacings while the variables DH and DS are explicitly typed into the program. This is a copy of the text of the program:

**********START OF PROGRAM**********

```
#pragma rtGlobals=1                    // Use modern global access method.

Menu "Macros"
        "Make Marcus Chi Square Plot", /Q, mMarcusChisquareGrid()
end

Function mMarcusChisquareGrid()

        Variable starthab=0, endhab=100
        Variable startlambda=0, endlambda=16000
        Variable habpoints=100, lambdapoints=160
        String yDataWaveName, xDataWaveName
        String coefName = "W_coef"
        String outputName
        Variable doLog=1
```

```
	Prompt habpoints, "Number of hab points"
	Prompt lambdapoints, "Number of lambda points"
	Prompt starthab, "First hab value"
	Prompt endhab, "Last hab value"
	Prompt startlambda, "First lambda value"
	Prompt endlambda, "Last lambda value"
	Prompt yDataWaveName, "Y data wave", popup WaveList("*", ";", "")
	Prompt xDataWaveName, "X data wave", popup WaveList("*", ";", "")
	Prompt coefName, "Coefficient wave", popup WaveList("*", ";",
"DIMS:1,MINROWS:2,MAXROWS:2")
	Prompt outputName, "Name for output matrix"
	Prompt doLog, "compute log(chi-square)", popup "Yes;No;"
	DoPrompt "Make Chi-square grid for Marcus fit function", habpoints, lambdapoints,
starthab, endhab, startlambda, endlambda, yDataWaveName, xDataWaveName, coefname,
outputname
	if (V_flag == 0)
		Make/N=(habpoints, lambdapoints)/O $outputName/WAVE=outw
		SetScale/I x starthab, endhab, outw
		SetScale/I y startlambda, endlambda, outw
		MarcusChiSquareGrid(outw, $yDataWaveName, $xDataWaveName,
doLog==1)
		CheckDisplayed/A outw
		if (V_flag == 0)
```

```
                    Display;AppendImage outw;AppendMatrixContour outw
                endif
        endif
end

Function Marcus(w,T) : FitFunc
        Wave w
        Variable T

        //CurveFitDialog/ These comments were created by the Curve Fitting dialog.
Altering them will
        //CurveFitDialog/ make the function less convenient to work with in the Curve
Fitting dialog.
        //CurveFitDialog/ Equation:
        //CurveFitDialog/ f(T) = ((2*3.1416)/(5.3085*10^-
12))*(hab)^2*(4*3.1416*lamda*.69504*T)^(-1/2)*exp(-((-
4000+5*T)+lamda)^2/(4*lamda*.69504*T))
        //CurveFitDialog/ End of Equation
        //CurveFitDialog/ Independent Variables 1
        //CurveFitDialog/ T
        //CurveFitDialog/ Coefficients 2
        //CurveFitDialog/ w[0] = hab
        //CurveFitDialog/ w[1] = lamda
```

```
	return ((2*3.1416)/(5.3085*10^-12))*(w[0])^2*(4*3.1416*w[1]*.69504*T)^(-
1/2)*exp(-((-4000+5*T)+w[1])^2/(4*w[1]*.69504*T))
End

Function MarcusChiSquare(cw, DataY, DataX)
	Wave cw, DataY
	Wave/Z DataX

	if (!WaveExists(DataX))
		Duplicate/FREE DataY, xwave
		Wave xw = xwave
	else
		Wave xw = $(GetWavesDataFolder(DataX, 2))
	endif

	Duplicate/FREE DataY, resids
	resids = DataY - Marcus(cw, DataX)
	resids = resids^2
	return sum(resids)
end

Function MarcusChiSquareGrid(cwmatrix, DataY, DataX, doLog)
```

```
	Wave cwmatrix, DataY
	Wave/Z DataX
	Variable doLog

	Make/D/FREE/N=2 cw
	Variable i,j
	for (i = 0; i < DimSize(cwmatrix, 0); i += 1)
		for (j = 0; j < DimSize(cwmatrix, 1); j += 1)
			cw[0] = DimOffset(cwmatrix, 0) + i*DimDelta(cwmatrix, 0)
			cw[1] = DimOffset(cwmatrix, 1) + j*DimDelta(cwmatrix, 1)
			if (doLog)
				cwmatrix[i][j] = log(MarcusChiSquare(cw, DataY, DataX))
			else
				cwmatrix[i][j] = MarcusChiSquare(cw, DataY, DataX)
			endif
		endfor
	endfor
end
```

**********END OF PROGRAM**********

- Values that need to be input in the program are written in green (ΔS) and purple (ΔH).
- Once the program is varied to the intended extent:
    - Access the “Macros” tab and click on “Compile”

- Click on the “Macros” tab once more and click on the “Make Marcus Chi Square Plot” tab
- This will produce a contour plot

- Many more plots can be created with this data
  - Under the “Windows” tab, highlight the “New” option and click on the plot of interest.
    - “Contour plot”
      - Variables such as the number of contour lines, the values between which the contour lines appear, the color of the contour lines are available
    - “Image plot”
      - Same variables are available, but the plot shows smooth transitions between contour lines
    - “3D Surface plot”
      - Allows a 3-dimensional view of the data collected from running the program